THERMAL-STRUCTURAL OPTIMIZATION AND RELIABILITY OF LEADFRAME SOLDER JOINT GEOMETRY IN ELECTRONIC PACKAGING

Kofi Nelson-Owusu

B.Sc. in Civil Eng., Portland State University, 1992.

M.S. in Civil Eng., Portland State University, 1994.

A thesis presented to the faculty of the

Oregon Graduate Institute of Science and Technology

In partial fulfillment of the

Requirements for the degree

Doctor of Philosophy

In

Materials Science and Engineering.

January, 2000

The dissertation:
Thermal-Structural Optimization and Reliability of
Leadframe Solder Joint Geometry in
Electronic Packaging

By

Kofi Nelson-Owusu

Has been examined and approved

by the following Examination Committee:

Lemmy L. Meekisho, Thesis Advisor
Associate Professor
Department of Material Science and Engineering
Oregon Graduate Institute of Science and Technology

Jack McCarthy
Assistant Professor
Department of Material Science and Engineering
Oregon Graduate Institute of Science and Technology

David G. Atteridge
Professor
Department of Material Science and Engineering
Oregon Graduate Institute of Science and Technology

Jack H. Devletian
Professor
Department of Material Science and Engineering
Oregon Graduate Institute of Science and Technology

In Everything Give Thanks For This Is The Will Of God in Christ Jesus ...1 These. 5:18

ACKNOWLEDGMENTS

TABLE OF CONTENTS

LIST OF TABLES

LIST OF FIGURES

ABSTRACT

**Thermal-Structural Optimization and Reliability of Leadframe Solder Joint
Geometry in Electronic Packaging**
Kofi Nelson-Owusu, B.Sc., M.S.

Ph.D., Oregon Graduate Institute of Science and Technology
January 2000

Thesis Advisor: Dr. Lemmy L. Meekisho

In surface mount technology, the near-eutectic 63Sn-37Pb solder alloy is frequently used to connect electronic chip modules to printed circuit boards, due to its low melting temperature, so as to protect other sensitive electronic devices from high temperature exposure during the reflow soldering process. The resulting solder joint, beside providing connections for electrical signal lines, is relied upon to provide structural integrity for resisting thermomechanical forces resulting from thermal, cooling fluid, and random vibration found in most electronic packaging service environments.

This study presents a multidisciplinary approach of modeling solder joints by incorporating all the variables that affect solder joint integrity. From the joint formation of the molten solder state to the final joint solid state when subjected to thermomechanical loads to predict the optimum solder joint fillet shape using structural optimization techniques. A new bond force model was developed and used to predict the interfacial bond stress state in a gullwing leadframe solder joint. In addition, an elastic-plastic material constitutive parameters model referred to as *"the unified creep model"* was developed from experimental data on eutectic Sn-Pb alloy and used for the nonlinear finite element analysis. In developing the model, continuum damage mechanics principles and neural networks methods were applied, together with experimentally derived eutectic Sn-Pb solder alloy data. This approach was used to minimize possible uncertainties that are normally associated with experimental data collection.

The study revealed that, at the optimum solder joint shape (assuming that the solidified fillet shape of the solder remains unchanged from the molten state) only the surface tension and the wetting angles of the molten solder fillet relate directly to the

imposed thermomechanical loads. The effect of gravity on the solder joint fillet formation was negligible and hence ignored in solder joint reliability studies. Nonlinear elastic-plastic finite element analysis based on the predicted optimum solder joint was performed to validate the proposed bond force, and the material constitutive models use to formulate the optimization problem. The resultant state of stresses was found to be within the eutectic Sn-Pb alloy strength limits, used in the optimization analysis.

CHAPTER ONE

INTRODUCTION

1.1 **Electronic Packaging Architecture Overview**: Tremendous strides have been made in microelectronics technology over the past decade.[1] The challenges of dense component packaging, heat sensitivity, and miniaturization of the solder leads have created numerous problems in the area of finished product performance. With continued demand for higher performance, the electronics industry is packing more and more circuitry onto a silicon chip, without equivalent emphasis on the structure that carries the chips. Consequently, the systematic treatment of the engineering, the science and the art of packaging application and inter-disciplinary treatment of microelectronics thermal-structural are rarely cited in literature. The high degree of integration, high speed, high power level, and high production cost of advanced electronic packaging systems have imposed more stringent reliability requirements beside the obvious ones such as the electrical and electronic issues.

Another reason that may explain the lack of treatment of themal-structural interaction in detail, might be due to the multidisciplinary nature of electronic packaging analysis.[2] The successful researcher or practitioner in this area must employ sophisticated knowledge in electrical engineering, mechanical engineering, chemical engineering, materials science and computer science. This research work relates to how the Ceramic Quad FlatPack (CQFP) chip with gullwing leadframes is soldered efficiently and reliably at the solder joints. The thermomechanical, geometric, and the materials issues related to solder joints are explored in detail in this study. The mechanical engineering issues considered in this work include thermal analysis, shock, vibration and durability in electronic packaging systems.

The packaging of high-performance electronic systems such as, computers, sophisticated medical and laboratory instrumentation, military hardware, as well as manufacturing equipment, require engineering design and development at several distinct packaging levels, [1] see figure 1.1.

The principal levels of packaging architecture, consist of the structure that houses the chip module, known as the first level packaging (chip level), the chip-to-chip interconnect which is called the second level packaging (board level). Finally the board-to-board interconnect structure referred to as the third level packaging (system level). These packaging levels can be seen in figures 1.1 and 1.2. At each of these levels, the package designer must provide an electrical signal distribution means for delivering a properly conditioned power and a means of removing heat generated at the target component and or device temperature. At the board level, the solder joint provides mechanical support and environmental protection for both the functional and interconnects circuitry.
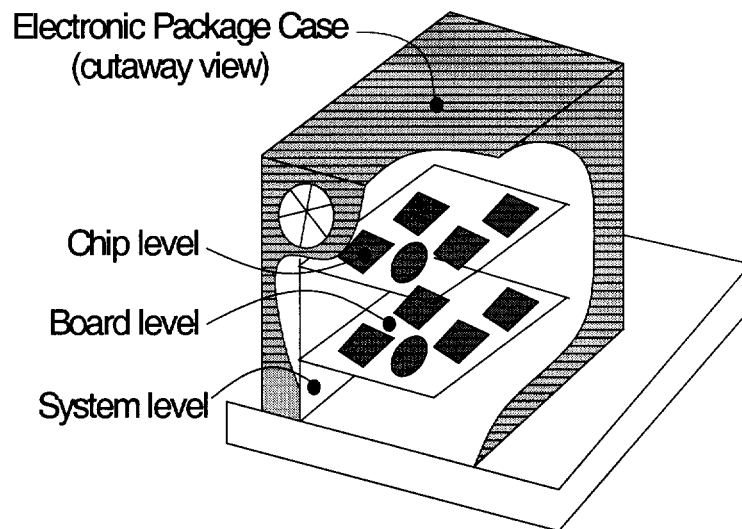
Fig. 1.1   Electronic Packaging Architecture
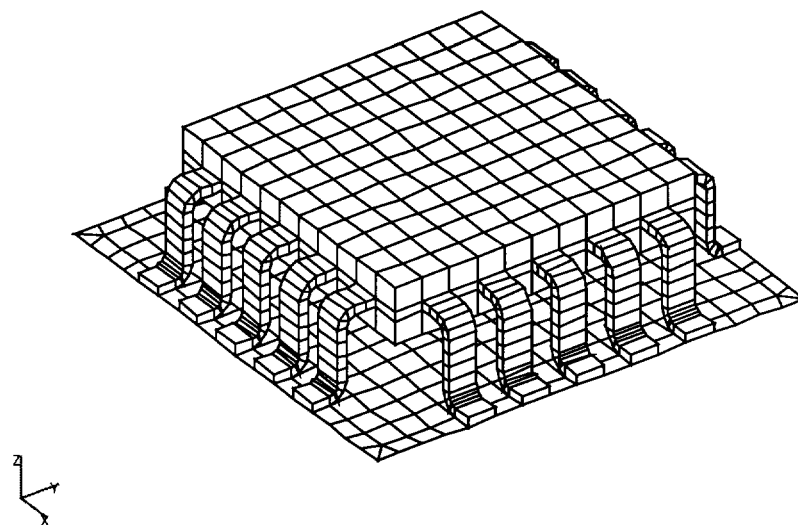
Fig 1.2 3D Schematic View of Surface Mount CQFP with Gull Lead Frame

1.2   Economic Consideration: Precise statistical data on the total cost of mechanically induced electronic package components failures could not be found in published literature, however, one can make fairly representative estimates based the state of the current electronics market. In this electronic age, electronic equipment can be found in virtually every aspect of our modern life, from toys and appliances to high-power computers. The equivalent capital value may be substantial enough to merit studies of failure and reliability of components. Vibration and shock are usually considered the next most damaging factor besides temperature influence, which accounts for about 20 – 30% of all Air Force Avionics Failure alone [3]. From these percentages of the rate of failure, if one assumes them to represent the general electronic packaging market, they will translate into millions of dollars. The 70-80% failure rates assigned to temperature influences include [3]:

- Temperature Dependent Mechanical Failure
- Temperature Induced Corrosion Failure
- Temperature Dependent Electrical Failure
- Temperature Effects on Electromigration
- Temperature Dependence on Operational Device Frequency

Judging from the effects of these influences, the total temperature dependent-mechanical failure alone, which is the subject of this research, will by far exceed the 30% failure rate. The consequence of this, vis-à-vis the dollar value is evidently quite far reaching, hence it crystallized the motivation for this work.

1.3 **Thermomechanical Loads**: Electronic packaging systems comprise of dissimilar materials (metals, ceramics, and polymers) that expand and contract at different rates due to temperature changes. These temperature changes are due to the various manufacturing and service conditions such as power cycling, seasonal changes from summer to winter, solar heating, and heat from appliances, altitude changes in aircraft, and heat developed by chemical processes. These conditions, when imposed on electronic packaging induce thermal expansion and stresses on the solder joint. Electronic packaging systems are also subjected to many different forms of vibration over wide frequency ranges and acceleration levels[2, 4]. Theses loads may include dynamic loading effects such as impact, shocks, vibration of the floor supporting the unit, induced fluid loads due to cooling fan / blowers, acoustic noise generated by cooling fans, repeated impact from typing keys on laptops computers, and accidental equipment abuse.[3, 5, 6]

Past research works on solder joint integrity issues have mainly addressed the effects of thermal loads on the solder joint by neglecting the mechanical component. Hence, the emphasis of this study was to consider the combined effects of thermal-structural interaction as they relate to the electronic package solder joint integrity. Surface mounted electronic packages rely upon the structural integrity of the solder for support in thermal, vibration, and shock environments[3]. Though, many different types of surface mounting methods are available, gull lead frame was used for this work. The thermal expansion and contraction due to the mismatch of materials in multimaterial structures (Silicon chip, wires, leadframe, and plastic), and non-uniform temperature distributions, may result in thermal stresses that are large enough to cause leadframe solder joint distortion or failure.

1.4 **Optimization Methods in Electronic Packaging**: The current motivation of electronic packaging design towards faster microprocessor units, higher component density, tighter integration and lower cost, have brought the importance of electronic packaging solder joint reliability and performance issues to light. Electronic devices are increasingly being designed to occupy less and less packaging real estate while at the same time expected to operate at high performance and reliability. In order to accomplish these, space and reliability requirements, computer modeling and simulation tools are applied extensively.[4] Thermomechanical analysis was applied to address design and operation efficiency of solder joint. Quantitative estimates for the design factors (variables) that affect the electronic packaging response to thermal and mechanical loads, which often show complex nonlinear behavior, can be made through structural optimization methods. [7, 8]

1.5 **Dissertation Objectives and Layout**: The principal objectives of this work are:

1. First, to break down the global finite element model of the top level chip module-to-board interface solder joint reliability problem into simpler modules. Secondly, to apply the readily available tools (hardware & software) using novel analytical techniques to solve the models of the global model. This approach has the advantage of reducing significant errors that would otherwise be unavoidable if a series of necessary simplifications were to be applied directly on the global model.

2. To identify and develop mathematical statements for the optimum solder joint geometric shape of electronic package solder joint under the influence of molten solder processing parameters and thermomechanical loads. Molten solder parameters include pressure, gravity, surface tension, contact angle and solder volume.

3. To integrate the optimum solder joint shape found in item 2 above to solve the top-level solder joint (local verification finite element model) in order to ensure the solder joint integrity, performance, and reliability of the electronic packaging.

4. Finally, to study the relationship between molten solder processing parameters and thermomechanical loads and their impact on solder joint shape formation using structural optimization techniques.

The reliability issues of solder joint in electronic packaging are generally, physical in nature and must be thoroughly understood. Therefore, multidisciplinary (see figure 1.3) materials are presented in chapters 2 to 5 to provide the fundamental understanding which are essential to the study of solder joint integrity phenomena in electronic packaging. The layout for this dissertation is as follows: Chapter 2, comes immediately after the introduction chapter and it deals with the mechanics of eutectic Sn-Pb solders and their physical, thermal, and mechanical properties as well as solder joint shape formation. Chapter 3 covers the treatment of mechanical loads through the formulation of structural dynamics equations for both deterministic and non-deterministic PCB and chip response. Chapter 4 covers the thermal loads through heat transfer equations formulation including fluid dynamics forces induced by the cooling fan and blower that may be acting on the packaging components. Chapter 5 addresses classical and stochastic optimization methods including their underlying theories. Simulated annealing which is a stochastic optimization method is presented in detail since it is known for its efficiency in determining the near-globally-minimum cost solution for large problems [9].

With the aid of the groundwork of chapters 2 to 5, the main components of this dissertation are presented. Here, we formulate both the global and local verification finite element models of the solder joint geometry problem. The global model results were used to solve for the optimum solder joint geometric-shape subjected to applicable constraints. The local model was based on isotropic, elastic-plastic eutectic Sn-Pb solder material properties. Finally, chapter 7 provides discussions and conclusions of the research work including dissertation contribution to the field of solder joint reliability in electronic

packaging. Logical extensions of the completed work in this dissertation are identified under future work.

MECHANICS OF
Sn-Pb MATERIALS

STRUCTURAL
DYNAMICS

HEAT
TRANSFER
ANALYSIS

FLUID
DYNAMICS

STRUCTURAL
OPTIMIZATION
METHODS

CHIP

CU-LEADS

PCB
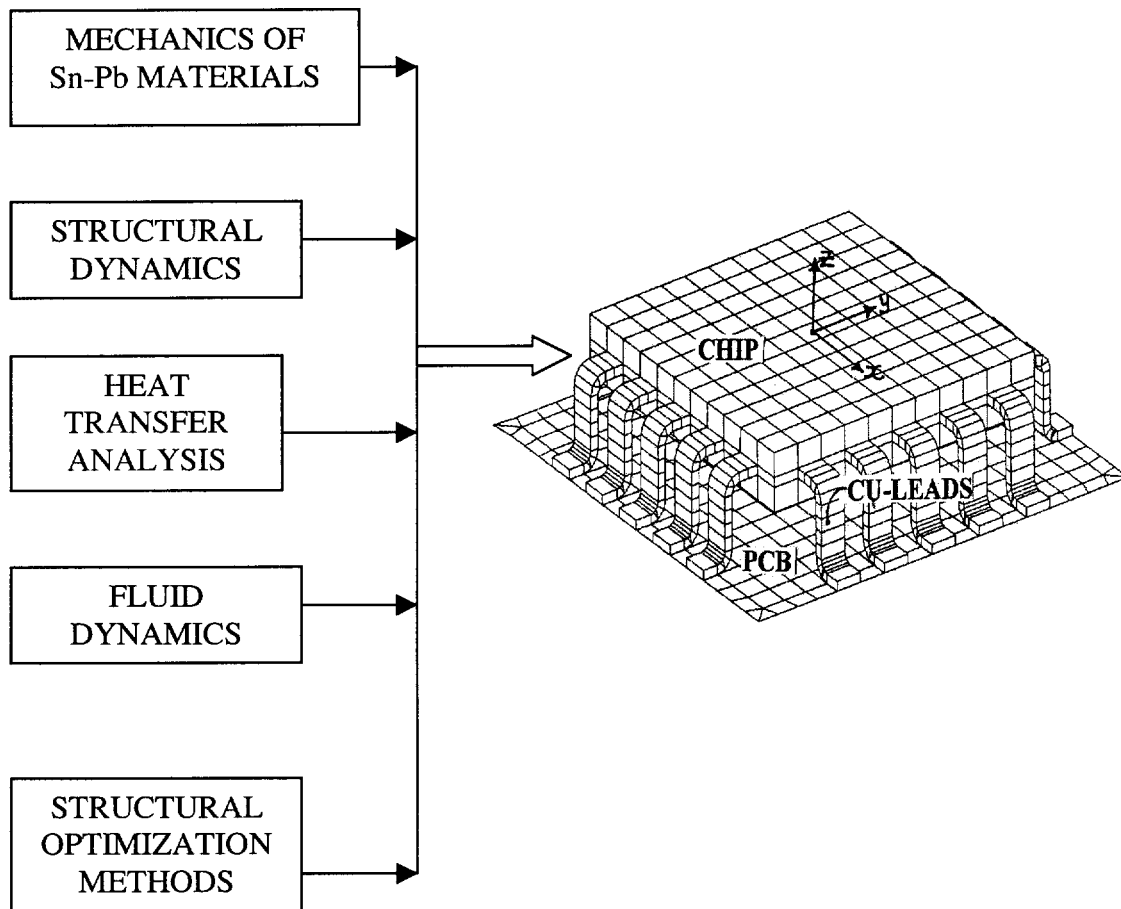
Figure 1.3   Research Components

CHAPTER TWO

MECHANICS OF Sn-Pb SOLDER MATERIALS

2.1 **Introduction**: The reliability of solder joints often depends directly on both thermal and mechanical properties of the solder alloy. The coefficient of thermal expansion (CTE) and thermal conductivity are the crucial thermal properties that affect solder joint integrity in electronic packaging. CTE sensitivity to temperature causes it to increase as the solder material temperature rises, while the reverse is the case with thermal conductivity. [10] There may be many other parameters that can affect the reliability of the joint but the key thermomechanical properties considered by many researchers to be crucial to solder joint integrity are tensile and shear strength, ductility, elastic modulus, toughness and creep. The processing history of solder alloys also determines the material's microstructure, which in turn will determine the thermomechanical properties.

The thermomechanical properties of metals depend on their microstructure ability to resist changes,[11] particularly 67Sn-37Pb solders used in electronic packaging, since the ratio of their operating temperature to the melting temperature is high and hence deserved to be studied. Thermomechanical loads and the extensive metallurgical interaction between the solder and the substrate metal can cause changes in the solder microstructure. Failed solder joints in electronic packaging data published in various journals revealed significant degradation in microstructure.[4] Solder joint integrity has been found to be highly dependent on the solder joint configuration, which, in turn, is determined by bond pad size, the alloy material, and the lead frame. Eutectic solder having a melting temperature of about 184 $^{\circ}$C is low enough to prevent thermal damage to sensitive electronic components in electronic packages and is used to attach components to the printed circuit board. Due to the low melting temperature of the alloy, hot deformation is common, which affects the microstructure and therefore the material properties of the alloy. Hot deformation phenonena in solder alloys is reported in solder joint fatigue literature.[12]

Sn-Pb eutectic structure exhibits dramatically different morphologies with different processing histories and microstructures or thermomechanical properties, and therefore this section of the dissertation will be limited to the solid mechanics aspect of eutectic Sn-Pb solder constitutive behavior under cyclic thermomechanical loads. A simplified method based on equilibrium conditions for predicting solder-to-leadframe interfacial bond stress model is proposed. The method considers the solder joint as structural element subjected to external thermomechanical forces.

2.1.1 Linear Stress and Strain Temperature Relations: When a real body is deformed as the result of externally applied thermomechanical forces, the internal forces in the body arises due to the change of the body's volume and geometric shape. If a small area element of the body ΔA with a normal vector **n** is taken in a plane passing through this body, with a resulting force of ΔF acting on it, then the stress vector is defined at this point as:

$$\sigma = \lim_{\Delta A \to 0} \frac{\Delta F}{\Delta A} = \frac{dF}{dA}$$

(2.1)

The stress vector σ does not need to be perpendicular to the reference plane and therefore can be resolved into the normal stress component σ_N, perpendicular to the plane of reference, and the shearing stress component τ_S, tangential to the plane of reference. Therefore a stress at a point can be specified by the three mutually perpendicular planes passing through a point. [13]

If we consider eutectic Sn-Pb solder alloy as an isotropic material with small uniform temperature change ΔT, and all infinitesimal line elements within the volume undergo equal expansions, without changing their initial directions. The resulting strain due to

temperature change ΔT in Cartesian coordinates (x, y, z) is given by the following relationships:[14]

$$\varepsilon'_{xx} = \varepsilon'_{yy} = \varepsilon'_{zz} = \alpha\Delta T \ldots\ldots\ldots\ldots\ldots(a)$$

and

$$\varepsilon'_{xy} = \varepsilon'_{xz} = \varepsilon'_{zy} = 0 \ldots\ldots\ldots\ldots\ldots(b)$$

$$(2.2)$$

Where:

α = Thermal coefficient of thermal expansion of the solder alloy.

ε'_{xx}, ε'_{yy}, ε'_{zz} = Normal strain components at a point caused by the application of external thermomechanical loads for each respective axis.

The corresponding stresses based on Hooke's Law are given by: [14]

$$\sigma_{xx} = \lambda e + 2G\varepsilon_{xx} - c\Delta T \qquad (2.3.1)$$

$$\sigma_{yy} = \lambda e + 2G\varepsilon_{yy} - c\Delta T \qquad (2.3.2)$$

$$\sigma_{zz} = \lambda e + 2G\varepsilon_{zz} - c\Delta T \qquad (2.3.3)$$

$$\tau_{xy} = 2G\varepsilon_{xy} \qquad (2.3.4)$$

$$\tau_{yz} = 2G\varepsilon_{yz} \qquad (2.3.5)$$

Where: $$c = (3\lambda + 2G)\alpha = \frac{E\alpha}{(1 - 2\upsilon)} \qquad (2.3.6)$$

$$G = \frac{E}{2(1+\upsilon)} \qquad (2.4) \qquad\qquad \upsilon = \frac{\lambda}{(\lambda + G)} \qquad (2.5)$$

E = Modulus of Elasticity.

λ = Lame's Elastic Coefficient

G = Shear Modulus of

υ = Poisson's Ratio

σ_{xx}, σ_{yy}, σ_{zz} = Stress components relative to orthogonal coordinate (x,y,z)

τ_{xy}, τ_{xz}, τ_{yz} = Shear stress components.

For isotropic elastic materials and using strain energy density formulation, it had been shown that for small-displacements, the volumetric strain due to externally applied thermomechanical force is given by: [14]

$$\varepsilon_{xx} = \frac{1}{E}\left[\sigma_{xx} - \upsilon\left(\sigma_{yy} + \sigma_{zz}\right)\right] + \alpha\Delta T \ldots\ldots\ldots(a)$$

$$\varepsilon_{yy} = \frac{1}{E}\left[\sigma_{yy} - \upsilon\left(\sigma_{xx} + \sigma_{zz}\right)\right] + \alpha\Delta T \ldots\ldots\ldots(b)$$

$$\varepsilon_{zz} = \frac{1}{E}\left[\sigma_{zz} - \upsilon\left(\sigma_{xx} + \sigma_{yy}\right)\right] + \alpha\Delta T \ldots\ldots\ldots(c)$$

$$(2.6)$$

$$\varepsilon_{xy} = \left(\frac{1+\upsilon}{E} \right) \tau_{xy} \dots\dots\dots\dots\dots\dots(a)$$

$$\varepsilon_{xz} = \left(\frac{1+\upsilon}{E} \right) \tau_{xz} \dots\dots\dots\dots\dots\dots(b)$$

$$\varepsilon_{yz} = \left(\frac{1+\upsilon}{E} \right) \tau_{yz} \dots\dots\dots\dots\dots\dots(c)$$

$$(2.7)$$

Finally, using linear elastic identities, the strain energy for the elemental volume under consideration in terms of strains is given by:

$$U_o = C_1 + C_2 - C_3 \dots\dots\dots\dots\dots\dots\dots\dots\dots\dots\dots\dots\dots\dots(a)$$

Where

$$C_1 = \frac{1}{2}\lambda \left(\varepsilon_{xx} + \varepsilon_{yy} + \varepsilon_{zz} \right)^2 \dots\dots\dots\dots\dots\dots(b)$$

$$C_2 = G\left(\varepsilon_{xx}^{\;2} + \varepsilon_{yy}^{\;2} + \varepsilon_{zz}^{\;2} + 2\varepsilon_{xy}^{\;2} + 2\varepsilon_{xz}^{\;2} + 2\varepsilon_{yz}^{\;2} \right) \dots\dots\dots(c)$$

$$C_3 = c\left(\varepsilon_{xx} + \varepsilon_{yy} + \varepsilon_{zz} \right)\Delta T + \frac{3}{2}c\alpha(\Delta T)^2 \dots\dots\dots(d)$$

$$(2.8)$$

2.1.2 Time Dependent Deformation – Creep: The near-eutectic solder alloy (63Sn-37Pb) is the solder material used mainly for interconnection of components in electronic packaging. The eutectic composition (61.9Sn-38.1Pb) requires the lowest temperature for total solidification of the alloy. The eutectic composition melting temperature is 183 °C and, for this study, it was assumed that the near-eutectic composition has the same melting temperature. The ratio of solder temperature-to-melting temperature is called the homologous temperature when expressed in absolute temperature scale (i.e $T_{homo.} = T_m(K)$ /2). During the past few decades, research work on solder joint reliability has been centered on temperature and its effects on the solder materials, as well as the development of accurate constitutive relationships to characterize the material through experimentation.[15,16] The characterization of solders presents a challenge since the material behavior is dependent on temperature and strain rate. For thin solder layers commonly found in electronic packages, the problem becomes very significant because of the complication of simulating the thermomechanical loading history that may be acting on the layers under controlled laboratory conditions.[16] In light of this fact, as with past research activities on thin layer solder constitutive relationships, the work of Gilat [16] was adopted for this study. The fundamental equations of uniaxial creep models under varying uniaxial stress are presented followed by solder joint material failure definitions based on continuum damage mechanics and stochastic damage models.

From creep theory, the general uniaxial creep equation is given by:[13]

$$f(\varepsilon, \sigma, t, T) = 0 \qquad (2.9)$$

Where:

$\varepsilon(t)$ = Strain history   T = Temperature

$\sigma(t)$ = Stress response in time   t = Time

Equation 2.9 may also be expressed in terms of creep strain as:

$$\varepsilon^c = F(\sigma, t, T) \qquad (2.10)$$

Where:

ε^{c} = The creep strain.

For the case of constant stress σ_1, producing a constant strain ε_1, the following expressions can be obtained from creep relaxation tests under constant stress conditions:

$$\sigma(t) = \sigma_1 H(t)................(a)$$

$$\varepsilon(t) = \sigma_1 J(t)................(b)$$

$$\sigma(t) = \varepsilon_1 E(t)................(c)$$

$$\varepsilon(t) = \varepsilon_1 H(t)................(d)$$

(2.11)

Where:

H (t) = Heaviside unit function:

$$H(t) = 0 \rightarrow if ...t \le 0......................(a)$$

$$H(t) = 1 \rightarrow if ...t \succ 0......................(b)$$

(2.12)

E (t) = Relaxation modulus obtained from test

J (t) = Creep compliance function

And all other terms have previously been defined.

The characteristic features of time dependent behavior at constant stress of a typical creep curve consist of three principal zones, namely; primary zone, secondary zone and the

tertiary zone. At the primary zone, the creep strain rate decreases in direct contrast to the tertiary phase where the strain rate increases as a result of the change of the dimension of the member cross-section and material deterioration which ultimately lead to creep rapture. At the secondary zone or regime, the response of the material to load stays fairly constant and therefore referred to as steady-state creep, see figure 2.0. The slope of the steady-state regime is equal to the creep rate. Experimental studies of creep mechanisms found in literature suggest that creep phenomena of Sn-Pb solders are mainly influenced by temperature in two ways,[13, 14, 16] which are:

- The dependence of solder material constitutive constants on temperature, and
- The structural changes of the solder alloy producing strain hardening or softening conditions.

Deformation of material below its homologous temperature above $0.5T_m$ is referred to as hot deformation, which is also true for solder alloys. Therefore the eutectic solder joint response to thermomechanical loads will be assumed to be of the hot deformation type for this studies due to the low melting temperature of the alloy. At room temperature, homologous temperature of the alloy approaches $0.5T_m$. In summary, the four temperature range cases obtained from uniaxial creep tests may be used to relate the creep to strain rate as a result of the activation of microstructural products within the member. These cases are briefly outlined below:

Case-1: At relatively low temperature ~ (T < 0.4Tm) - The predominant creep mechanism is the slip type. This characteristic is largely present in the primary creep regime.

Case-2: At intermediate temperature ~ (0.4 < T < 0.5Tm) – The strain hardening effect in the material is diminished by the dislocation creep mechanism caused by thermal activity of the crystal lattice structure of the material.

Case-3: At higher temperature ~ (0.5Tm < T < 0.6Tm) - The dislocation creep mechanism overcomes the strain hardening effect due to increase of thermal activity, resulting in the secondary phase. This is mainly true for the steady state creep regime.

Case-4: At very high temperature ~ (0.6Tm < T < 0.8Tm) - Diffusional creep mechanism results in a drastic increase of the strain rate preceding the creep rapture. This phenomenon occurs in the tertiary creep regime.

Where:

$\quad\quad\quad$ Tm = Soldier material melting temperature

$\quad\quad\quad$ T = Temperature of the material.

The importance of case 3 in solder joint reliability studies have been recognized and therefore for this study it is singled out for further treatment. Under these conditions, the solder strength may be greatly reduced to a level that it may not be adequate to resist the hot deformation caused by creep mechanisms acting on the joint. Many kinds of creep consitivitive relationships have been proposed in literature[15] with their own inherent degrees of uncertainty, especially with regard to 63Sn-37Pb solders. Mathematical models, in particular, Sn-Pb eutectic creep models, are usually imperfect descriptors of the complex physical phenomena, hence, predictions made from these models are plagued with three major source of uncertainties given below:[17]

1. Error in over-simplification of the testing apparatus setup and limiting test from capturing all the possible key variables.
2. Test data acquisition errors resulting from inaccurate measurement of variables under laboratory or field conditions and thereby adding to the error of uncertainty.
3. Statistical errors – the accuracy of the estimated parameters depends on the size of the available data set. A smaller data set, as in the case being considered, often introduces an additional uncertainty in estimating the material parameters.

To maintain some level of confidence in using these models for this study, a probabilistic approach to material damage behavior called continuum damage mechanics is presented. [18]
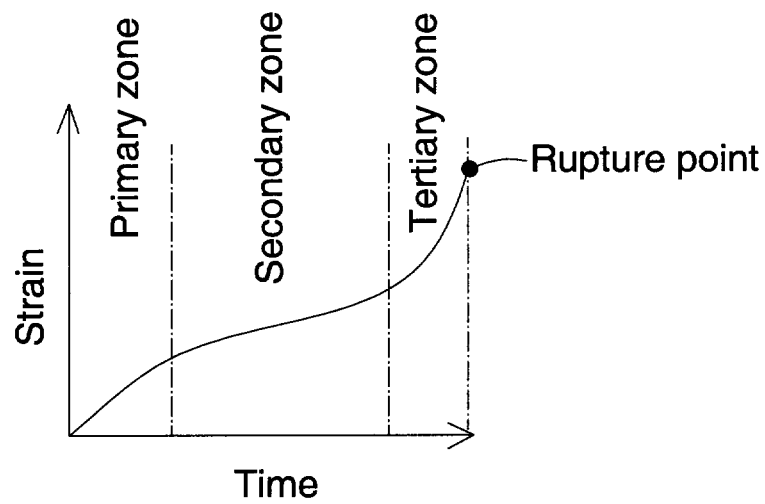
Figure 2.0   Basic Creep Curve

2.1.3 Continuum Damage Mechanics Approach: Solder joint structural damage accumulation is an intrinsically random phenomenon due to variations in the solder material microstructure, solder joint loading history, and the operating environment of the electronic package.[15, 19, 20] Continuum damage mechanics, (CDM), is well suited to deal with the random damage growth localization since it seeks to express the aggregate effect of microscopic defects[21] present within the solder joint materials in terms of macroscopically defined quantities. These microstructural defects that may be present in the solder joint include voids, discontinuities, and inhomogenetics. CDM seeks to relate these defects within a given material volume to properties that can be measured at the macroscopic level such as, tensile strength, shear strength, hardness, and Poison's ratio.

CDM defines damage as the density of defects/discontinuities on a cross section in a given orientation, amplified by their stress-raising effect.[20] For isotropic damage condition, and using the concept of effective stress, along with the principle of strain equivalence, the following equation may be used to relate the constitutive law for solder material damage loaded uniaxially to effective stress: [20, 22]

$$\bar{\sigma} = \frac{\sigma}{1 - D}$$
(2.13)

By application of the principle of strain equivalence, the damage may variably be related to the fractional loss in material stiffness, given as:

$$D = 1 - \frac{\bar{E}}{E}$$
(2.14)

Where:

σ = Normal Stress

$\bar{\sigma}$ = Effective Stress

E = Elastic modulus of undamaged materials

$\bar{E}$ = Elastic modulus of the damaged material

D = Scalar Damage Variable

Equations 2.13 and 2.14 provide a means for measuring the extent of damage in a structural component experimentally using one of the many conventional and non-destructive methods, including direct tension tests, ultrasonic pulse velocity, measurement of electrical resistivity have been used to generate constitutive data in reference [16].

For the purpose of this work, failure in the solder material is assumed to occur when the damage variable equals the critical damage D_c. It does not necessarily correspond to rupture but rather to the formation of macroscopic defects. The parameter D_c varies between 0.15 to 0.85 for engineering alloys,[20] hence it is treated as a random variable and is used in this study for the purpose of providing the basis for the application of stochastic CDM equation formulation for the solder joint material.

Stochastic Creep Damage Growth Prediction: Various constitutive relations for Sn-Pb eutectic solder joint alloy that account for both time-independent plasticity and steady-state creep have been developed and reported in the literature [15]. It is assumed that the total strain rate consists of elastic strain and plastic strain rates. In terms of pure shear, the total strain can be expressed as follows:

$$\varepsilon_{total} = \varepsilon_e + \varepsilon_p \dots\dots\dots\dots\dots\dots\dots\dots\dots\dots\dots\dots\dots(a)$$

Where:

$$\varepsilon_e = \frac{\overline{\tau}}{G}\cdots(\text{steady - state elastic component})\dots\dots(b)$$

(2.15)

$$\varepsilon_p = A\Phi\overline{\tau}t^{\Phi-1}\dots\dots\dots(c)$$

$\tau =$ Elastic shear stress

$G =$ Elastic shear modulus

$A =$ Material constant

$\Phi =$ 1.0 for Steady-State conditions

$\overline{\tau} =$ Effective shear stress

$t =$ Time

Equation 2.15c = (Bailey – Norton Creep strain rate relation under uniaxial loading condition)

Under constant stress creep (steady state regime), the increment in total strain is the same as that in creep strain and therefore using the work of Bhattacharya [20], when data noise is neglected, the following damage expression can be used to predict the critical damage parameter.

$$D_c = 1 - \left[(1 - D_o)^{m+1} - \frac{4}{3}\left(\frac{A\sigma_o^{m+1}}{\sigma_f} \right) \right]^{\frac{1}{m+1}} \qquad (2.16)$$

Where:

σ_o = The far-field stress acting normal to surface approximately equal to residual stress.

A = Material constant to be determined from test data

σ_f = True failure stress

m = Exponential material constant assumed to be unaffected by damage, determined by test data assumed to be 1.2

D_o = The initial damage assumed to equal to initial strain

Φ = 1 for steady-state condition [20]

D_c = Critical value of D

Using the data from reference [16], the computed values based on equations 2.15 and 2.16, and the materials from chapter 5, section 5.2.3 are shown in table 2.1

Table 2.1: Creep and Shear Properties of 63-37 Tin-Lead Solder (Ref. Temp. = 25°C)

PARAMETER	A	m	ϕ	τ	σ_f	E	K	D_o	DC
Nominal	0.025	1.2	1	10 (MPa)	49 (MPa)	48.2 (MPa)	234 (MPa)	0	0.625
S. D.				-	0.228	-	0.228	-	0.228
Distribution	LN	N		Det.	N	Det.	N		N

Note: LN = lognormal, N= normal, Det. = deterministic, S.D. = standard deviation

2.1.4 Mechanics of Interfacial Bond Force: Lead frame bond connections are susceptible to bond shear and bond stress (peeling stress) failure due to high thermomechanical loads resulting from the combined effects of thermal stress and vibration forces. Starting from the pioneering work of the Timoshenko using beam theory [23], Chen and Nelson [24], and several other investigators dealing with interfacial bond stress research work have reported their findings in literature.[10, 25] Suhir,[26-28] Pao, and Eiseue,[29] were able to predict the thermal stresses in layered structures by assuming that the material remains linear elastic. Although these proposed methods have the advantage of predicting interfacial bond stresses between layers, they all failed to consider the complete joint configuration and thereby imposing symmetry conditions. It should be noted that, a typical surface mounted leaded device solder joint shown in figure 2.1 does not have symmetry along the length of the joint. This study considers the whole joint configuration without the application of the symmetry condition in formulating the expression for the maximum bond stress. The proposed bond force (stress) method is based on the prying deformation of an equivalent bolted solder joint.

The simplifying assumptions pertinent to the development of the proposed model include:

1. Perfect adhesive bonding exists at all joint interfaces before the application of thermomechanical loads. [30]

2. The local area of the boundary where the bond pad is attached to the printed circuit board (PCB) is infinitely rigid, hence out-of-plane bending effect in the solder due to both bond pad and PCB is negligible.

3. The external forces acting on the solder joint system are due to thermomechanical forces acting on the leads and the thermal force within the solder joint as a results of temperature changes.

4. Initial bond stress due to solder solidification process is low due to the low heat input of the soldering process, hence can be ignored.

5. The distribution of bond stress between the leads and the solder element interface can be described by a parabolic function for gullwing leadframe,

increasing from the heel of the joint and approaches zero at the toe of the joint. The area under the curve equals the equivalent bond stress.

6. The solder joint system is subjected to uniform temperature change.

It assumed that metallurgical bond does not take place since the surfaces being joined are not melted in reflow soldering process. It is important to note that, from assumption 5, the bond stress at the toe is not necessarily zero, rather it approaches zero.

Lets consider the curved element part of the gullwing leadframe solder joint shown in figure 2.1, with axial force **P**, shear force **V** and moment M_0 acting on it due to thermomechanical effects.
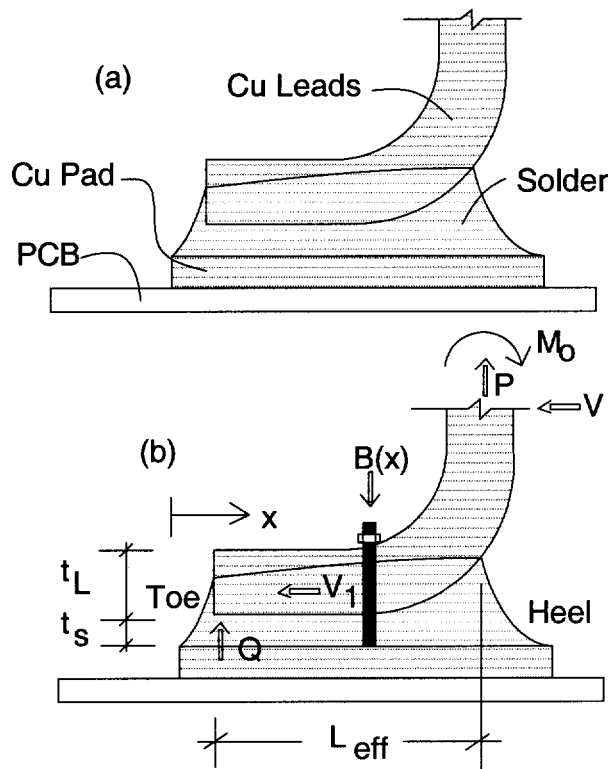
Figure 2.1   (a) Schematics of Leaded Solder Joint and (b) Equivalent Bolted Solder Joint Connection with Applied Forces

Using Castiglano's curved beam energy theorem states that the rate of change of strain energy for a body with respect to any statically independent force **P** gives the deflection component of the point of application of this force in the direction of the force. Similar statement is made for moments and rotation, that is, the rate of change of strain energy with respect to a statically independent point couple **M₀**, gives the amount of rotation at the point of application of the couple, about an axis collinear with the complete moment.[31] These two statements of the theorem imply that, mathematically, we can relate the external applied forces acting on a structural element subassembly to its internal forces.[14] For the case of gullwing solder joint, if we assumed that the curved portion of the leads plane section remain plane before and after the application of the loads, and that the effect of both radial and shear stresses are sufficiently small such that the state of stress is essentially one-dimensional, the following statement can be made.

$$\delta P = \frac{\partial U}{\partial P} .....(a) \qquad \phi = \frac{\partial U}{\partial M_O} ......(b) \qquad (2.17)$$

Where the δP, ϕ, and **U** represent the deflection component of the curved element in the direction of load **P**, the angle of rotation in the direction of the **M₀**, and the total strain energy in the curved element at $\theta = 0$, respectively. From figure 2.2, the applied loads **V** (θ), **N** (θ), and **M** (θ) at a section forming angle θ with the face **OC** are

$$V(\theta) = P\sin\theta ....(a)$$

$$N(\theta) = P\cos\theta ....(b)$$

$$M(\theta) = M_o - PR(1 - \cos\theta) ....(c)$$

$$(2.18)$$
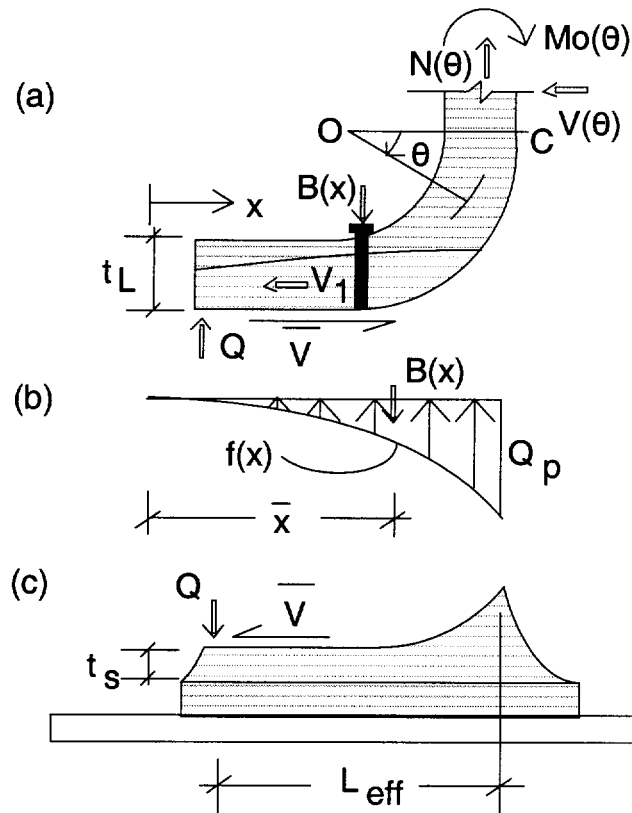
Figure 2.2   Analytical Interface Bond Stress Model: (a) Forces acting on the Lead; (b) Bond Stress Profile along x-direction at leads-solder interface; (c) Solder-Copper Pad- PCB Interface Forces

Applying the Castigliano's energy theorem to the curved element under consideration, the total strain energy is given by: [14]

$$U = \int\left(\frac{kV^2R}{2AG}\right)d\theta + \int\left(\frac{N^2R}{2AE}\right)d\theta + \int\left(\frac{A_m VM_x^2}{2AE(RA_m - A)}\right)d\theta - \int\left(\frac{M_x^2 N}{AE}\right)d\theta$$

(2.19)

Substituting equations 2.18 and 2.19 into 2.17, we obtain

$$0 = \int_0^{\frac{\pi}{2}}\left(\frac{(M_o - PR(1 - \cos\theta))A_m}{AE(RA_m - A)}\right) - \int_0^{\frac{\pi}{2}}\frac{P\cos\theta}{AE}d\theta$$

(2.20)

Solving for M_o we obtain

$$M_o = PR\left(1 - \frac{2A}{\pi RA_m}\right)$$

(2.21)

Where for rectangular leads cross-section with width **d**, and depth **t**,

$$A_m = \int\frac{dA}{r} = d\ln\frac{R}{t}$$

(2.22)

With M_o known, the loads at every section of the curved element of the leads and solder joint can be determined.

Equivalent Bond Stress: Consider the deformation of solder joint for gullwing leadframe shown in figure 2.2, where thermomechanical forces deformed and lifted the Lead leg upward. The edge of the lead at the toe of the joint bore against the solder element-giving rise to the force **Q**, known as the Prying force. The prying force is due to the re-distribution of the applied load and the relative flexibility of the leads to the stiff solder element, bond pad and the PCB.

Applying force equilibrium conditions at the joint as $\theta \to 0$ to figures 2.2, yield

$$Q\bar{x} + M(\theta) - N(\theta)b - V(\theta)R - V_1\frac{t_L}{2} = 0 \dots\dots\dots(a)$$

$$Q - B(x) + N(\theta) = 0 \dots\dots\dots\dots(b)$$

$$V_1 + V(\theta) = 0 \dots\dots\dots\dots(c)$$

$$(2.23)$$

Equations 2.23a-c are independent equilibrium equations that must be satisfied. Making substitution for terms in equation 2.23, and solving for Q and V_1, results in

$$Q = \frac{1}{x}\left(\frac{2PA}{\pi A_m} + V_1\frac{t_L}{2}\right) \dots\dots\dots(a)$$

$$Q = B(x) - P \dots\dots\dots(b)$$

$$V_1 = V(\theta) \dots\dots\dots(c)$$

$$(2.24)$$

Solving for B(x) by equating equations 2.24a to b, gives the expression for the resultant bond stress

$$B(x) = P\left(1 + \frac{2A}{\overline{x}A_m \pi}\right) + \frac{V_1}{\overline{x}}\left(\frac{t_L}{2}\right)$$

(2.25)

As the temperature of the joint changes, copper leads and the solder joint experience shear stresses as a result of differential thermal expansion between the two materials. The solder joint in-plane thermal deformation $d\delta$ along the x-direction for both materials are given by

$$d\delta_S = (\alpha_S \Delta T)dx \dots\dots\dots\dots\dots(a)$$

$$d\delta_L = (\alpha_L \Delta T)dx \dots\dots\dots\dots(b)$$

(2.26)

Applying compatibility condition of the interface, the shear stress and strain expressions are given by

$$\gamma = \frac{\delta_L - \delta_S}{t_S} = \frac{\tau}{G_S} \dots\dots\dots\dots(a)$$

$$\tau(x) = \frac{(\alpha_L - \alpha_S)}{t_S}\Delta TGx \dots\dots\dots(b)$$

(2.27)

Therefore the shear force V_1 acting on the effective interface area A_{eff} is given by

$$V_1(x) = \left[Gx\left(\frac{\alpha_L - \alpha_S}{t_S}\right)\Delta T \right] A_{eff}$$

(2.28)

Distributed bond stress: Applying assumption 5, equation 2.25 may be related to the actual distributed bond stress present at the interface of the leads and solder joint as shown in figure 2.2b and is given as:

$$\overline{B}(x) = \int_{x=0}^{x=L_{eff}} \left(f(x)A_{eff} \right)dx = \frac{Q_P d}{L_{eff}^2}\left(\frac{x^4}{4} + C\right) = \frac{Q_P x^4 d}{4L_{eff}^2}$$

(2.29)

Where A_{eff} = xd, the lead-solder contact area (figures 2.2 and 2.3) and the constant of integration is considered zero through the application of the joint boundary condition, i.e. as $x \to 0$, $\overline{B}(x) \to 0$. Equilibrium condition requires that, the bond force equations 2.25 and 2.29 are equal, (i.e. $B(x) = \overline{B}(x)$), therefore the maximum bond stress Q_p, occurring at the heel of the joint, may be obtained by equating the two equations, resulting in

$$Q_P = P\left[\left(1 + \frac{2A}{A_m \overline{x}\pi}\right) + \frac{V_1}{x}\left(\frac{t_L}{2}\right)\right]4L_{eff}^2$$

(2.30)

Making substitution for $x = L_{eff}$, V_1, and $\overline{x}$, in equation 2.30, the expression for the maximum bond stress is obtained as:

$$Q_P(x = L_{eff}) = 4PL_{eff}^2(C_1 + C_2)\varphi$$

(2.31)

The constant φ is introduced into the equation 2.31 to modify the restriction imposed by assumption 1, by accounting for the variability of the solder joint components interface bonding conditions. Its value ranges from 1.0 for perfect bond to 0.1 for poor bonding, and may be determined experimentally.

Where

$$C_1 = \left[1 + \frac{8A}{3A_m \pi L_{eff}} \right]$$

$$C_2 = \frac{2}{3} G \Delta T (\alpha_L - \alpha_S) \frac{t_L}{t_S}$$

P, V = Externally applied thermomechanical axial and shear forces.

$V_1(x)$ = Internal force within the solder element due to temperature change.

B (x) = Resultant bond force obtained from integration of the area under parabolic bond stress distribution function f (x)

Q = Concentrated bearing forces acting at the toe of the solder joint due to the flexibility of the leads.

t_L, t_S = Thickness of lead frame and solder element respectively.

σ_p = Yield stress of the solder material.

$\bar{x} = \frac{3}{4}$ (L_{eff}), the centroid of the parabolic bond stress distribution

b = $L_{eff} - x$

R = Radius of leadframe leg curvature at the solder joint.

A = Leadframe cross-sectional area.

2.2   Solder Joint Geometry Formulation: The demand for higher integrated circuit functionality and clock speed in electronic packaging, particularly in surface mounted technology (SMT) requires new approaches that address wider solder joint integrity problems. This means, the gap that exists between the influence of solder joint shape formation during reflow and joint integrity for both testing and service conditions should be very narrow [32]. A review of the literature on the subject of solder joint reliability issues suggests that there has been significant research activity on solder joint integrity from the perspective of structural analysis and fatigue life prediction, under a variety of thermal and mechanical loading conditions,[32, 33] all done on an assumed joint geometry. Hence, a combined approach that considers joint formation during the manufacturing phase and joint integrity during testing and service conditions are presented in this work.

Joint formation starts with the solder in a paste form, heated until it liquefies and then cools to a solid state. The behavior of the solder during this process is complex due to the coupling effects of the thermomechanical behavior of the chip and PCB interface condition, the fluid flow, heat transfer, and the phase change mechanics of the solder material. The resulting shape from the joint formation process can then be treated as a structural component (analysis model) bonded to the chip and the PCB, which is acted upon by thermomechanical loads. It is important to determine the correct volume of solder to use for a given joint. Since too much solder will lead to the problem of bridging between adjacent terminals, while the opposite may cause problems with joint strength. In this section, a mathematical formulation of the geometric shape for gull leads solder joint is presented. The formulation is based on joint pad size, solder volume, the wetting angle, surface tension and the gravitational force [33-36].

2.2.1 ASSUMPTIONS AND MATHEMATICAL FORMULATION: The objective of this part of the research work is to find an engineering approximation to the solder profiles of some practical rectangular (gullwing leadframe legs) pad geometry. Consequently, the following assumptions are made to simplify the formulation: [33-37]

1) The solder joint attains static equilibrium when solidification occurs.

2) The solder pad on the substrate is rectangular and is perfectly aligned at the time of solidification.

3) Solder properties, including density and surface tension are uniform within the joint.

4) The solder pad is completely covered by solder, which does not spread beyond the pad.

5) The solder pad metallization is assumed to be perfectly wettable, while the surrounding surface remains dry.

Formulation of solder joint geometric surface contours is based on Laplace's equation. Considering a differential element of membrane under equilibrium conditions, the relationship between pressure jump and curvature of the solder may be expressed as follows:

$$P_o = P_a + \gamma \left(\frac{1}{R_1} + \frac{1}{R_2} \right) + \rho g z$$

(2.31)

where

P_a = Atmospheric, (ambient) pressure as a function of z

P_o = Internal pressure as a function of z

γ = Surface tension a solder-atmospheric interface.

R_1, R_2 = Average the principal radii of curvature of the solder as a function of z

ρ = Mass density of liquid solder.

g = Gravitational constant.

h = Height at which solder terminated.

z = Solder height dummy variable.

For static equilibrium, the last term of equation 2.31 suggest that, the internal pressure variation will be hydrostatic. Defining an arbitrary Cartesian coordinates (x, y) plane through the differential element shown in figures. 2.3, and neglecting the 3-dimensional effects, the governing equation originally in a 3-dimensional system is reduced to 2-dimentional by the elimination of one of the two principal radii. Therefore the simplified governing equation is given by:

$$P = P_o - P_a + \gamma \frac{1}{R_1} + \rho g z$$

(2.32)

Where the slope of the curvature **1/R** is considered positive, if the center of it lies to the outer side of the solder surface (concave outward).
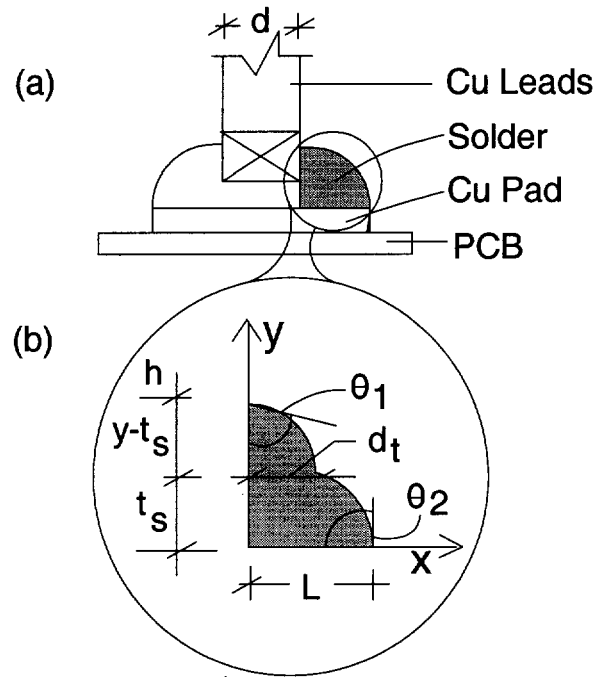
Figure 2.3   Cross Section of Gullwing Leadframe Solder Joint Geometry (a) Arbitrary Solder Shape (b) an enlarged solder fillet described by the governing equation

In reference to figure 2.3, the corresponding curvature equivalent in rectangular coordinate system is given by [35, 37].

$$\frac{1}{R} = \frac{y''(x)}{\left[1 + [y'(x)]^2\right]^{\frac{3}{2}}}$$

(2.33)

Where the primes represent differentials and all other terms previously defined. It is assumed that, the liquidus solder internal pressure directly underneath the leads is balanced

by the downward force of the total self-weight of the unit. This assumption is reasonable since the solder directly under the leads provides mechanical support to the self-weight of the device (chip and leads) before and after the reflow soldering process. Therefore, the remaining internal pressure and surface tension forces will formed an arbitrary membrane shape shown in figure 2.3b. If equation 2.33 is substituted into equation 2.32 and the a dummy variable z is changed to y and making further simplification, the joint profile governing equation is given by:

$$\frac{\rho g y}{\gamma} - \frac{P_o - P_a}{\gamma} = \frac{y''(x)}{\left[1 + [y'(x)]^2\right]^{\frac{3}{2}}}$$

(2.34)

Equation 2.34 becomes the governing equation, which may be used to describe the solder joint formation shown in figure 2.3b, subjected to the following boundary conditions.

$$y(x = 0) = h............................(a)$$

$$y'(x = 0) = -\cot\theta_1....................(b)$$

$$y(x = d_t) = 0.........................(c)$$

$$y'(x = d_b) = -\tan\theta_2....................(d)$$

(2.35)

$$A_{sec}(x = 0) = \int_0^{d_b} y(x)dx..................(e)$$

Where **h**, **d$_t$** are the permissible height and length of the solder joint respectively. The wetting angles θ_1, θ_2 and the solder cross-sectional **A,** are as defined in figure 2.3. If we let the volume of the solder paste directly underneath the leads before joint formation, (i.e.

reflow process) be represented by V_o, then the following relationship can be expressed between the cross-sectional area of figure 2.3b and Volume as:

$$V = V_o + A_{\mathrm{sec}}\left(L_{path}\right) \tag{2.36}$$

Where the last term of equation 2.36 is assumed to be the perimeter of the bond pad.

2.2.2 SOLUTION METHOD: Equation 2.34 is a second order ordinary differential equation requiring two boundary conditions. The three additional boundary conditions (equation 4a-e) are necessary for the presence of the three unknown terms in the model, namely; ρ_o, **h**, and $\mathbf{d_b}$. Normally, the solder properties (ρ, **g**, γ) of joint fillet area **A**, and wetting angles θ_1, and θ_2 are specified before the formation of the joint. The solution to the governing equation (equation 2.34), for the solder joint can be found in reference [35] and therefore will not be repeated here. The mathematical expression derived in this chapter will be used in chapter six to augment the analytical bond force model.

-CHAPTER THREE

MECHANICAL LOAD EQUATIONS FORMULATION

3.1 **Introduction**: Natural phenomena and human activities impose forces of a time-dependent variability on electronic packaging components [2, 4, 38, 39]. These time-dependent forces are the results of the oscillatory motions or vibrations, which the packaging system may be subjected to during its service life. In order for mechanical vibrations in (second level) electronic packaging system to occur, two energy-storage elements must be present in the system.[40] The mass, to store kinetic energy, and a spring, to store potential energy. The chips and the heat sinks are the masses and the lead frames are the springs for a given electronic packaging system at the chip level, as shown in figure 3.1.

Oscillatory systems can also be deterministic or probabilistic (random) in terms of its response to external loads. If the elastic member is linear, then the system's response to excitation will be sinusoidal or harmonic motion. On the contrary, if the system response to excitation does not follow any apparent pattern, the resulting motion or vibration record is called random vibration, and is probabilistic in nature. Electronic packaging assemblies, besides being subjected to the aerodynamic buffeting (drag and lift forces) caused by the cooling air, are also subjected to random forces. [3, 5, 6, 41-43] These random forces are induced by package shipment or transportation, accidental impact or shocks, vibration of the building floor supporting the unit and, for some, vibratory-in-service environments, like military and emergency vehicles. The random forces are normally described by statistical parameters such as the "mean value" and the "power spectral density." Some typical failure modes in electronic packaging associated with vibration and shock include broken lead wires, cracked solder joints, flexure of the circuit boards, broken circuit board traces, shorting of the lead, and loosening or complete loss of electrical contact. [3, 5, 6, 41-43] The goal of this section is to develop methods, and mathematical formulations for analyzing the stress, strain and displacements acting on electronic package solder joints when subjected to an arbitrary dynamic or time varying load.
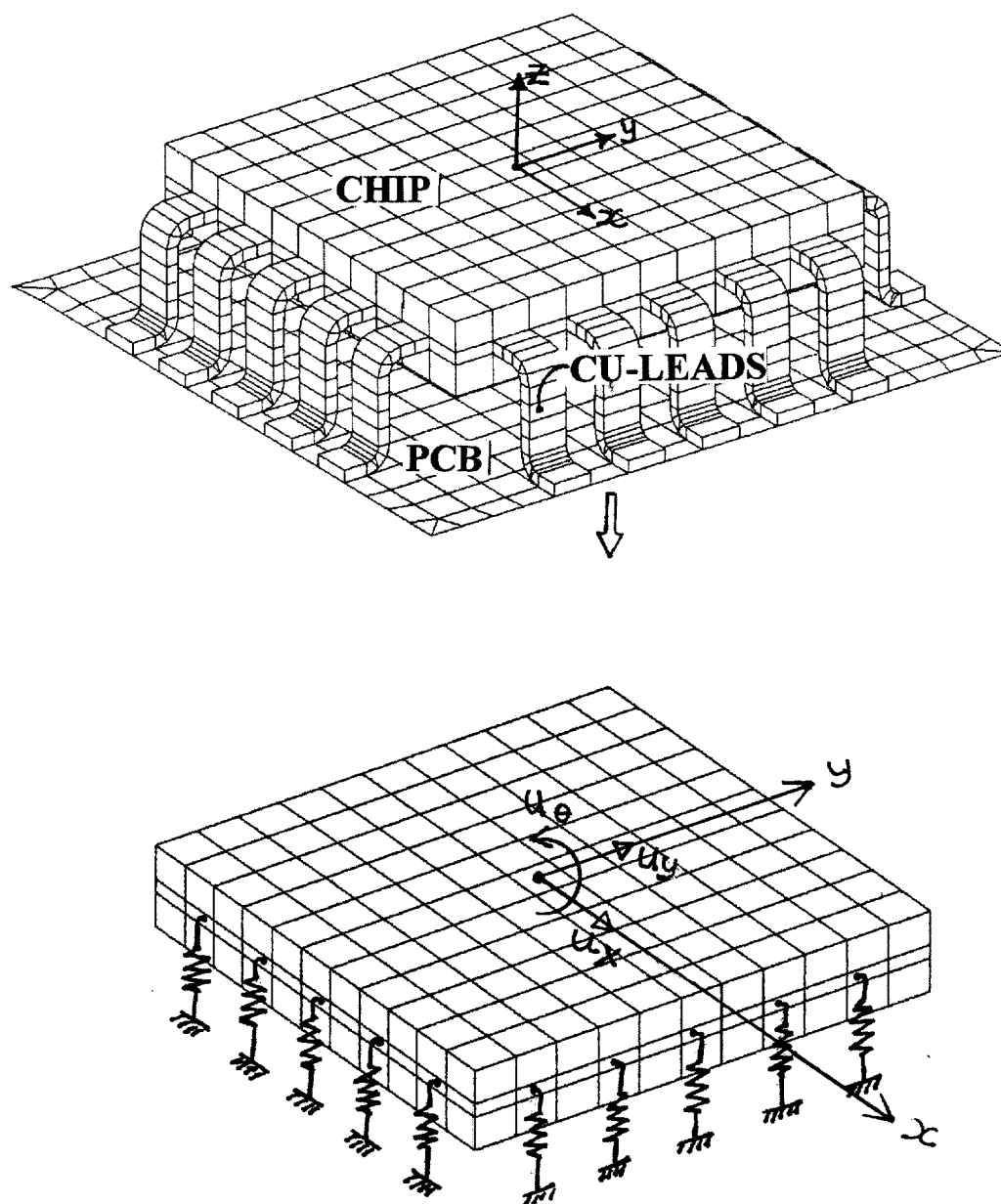
Figure 3.1   Integrated Circuit Package (above) and Analytical Model of
Package (below)

3.2   EQUATION OF MOTION FOR PCB: Many electronic packaging structural components are made of composite materials, such as plates or shell used at both board level and the chip levels. Though several theories have been developed to model both the transverse deflections and flexural behavior of composite laminates, the classical lamination theory (CLT), similar to classical bending theory for plates will be used in this work.[44-47] The **x, y, z** coordinate system is assumed to have its origin on the middle surface of the plate, so that the middle surface lies in the **x y** plane. The **x-, y-, z-** displacements at a point are denoted by **u, v,** and **w**, respectively.

The CLT is based on the following assumptions:

1. The plate consists of orthotropic laminae bonded together, with the principal material axes of the orthotropic laminae oriented along arbitrary directions with respect to the **x** and **y** axes.

2. The laminate is thin.

3. The displacement **u, v,** and **w** are small compared with the plate thickness.

4. The strain distribution is linear along the thickness direction.

5. Out-of-plane shear strains are zero.

6. Each ply obeys Hooke's law.

7. The plate thickness is constant.

An infinitesimal element shown in figure 3.2 will be used to develop the differential equations governing plate deflections will be used where N_x, N_y, and N_{xy} are the in-plate resultant forces in **x** and **y** directions and **xy** plane respectively. M_x, and M_y are the bending moments, Q_x and Q_y are the transverse shear stress resultant in **x** and **y** directions respectively, and **q(x, y)** is the transverse distributed load.

$$Q_x = \int_{-t/2}^{t/2} \tau_{xy} dz \dotfill (a)$$

(3.1)

$$Q_y = \int_{-t/2}^{t/2} \tau_{yx} dz \dotfill (b)$$
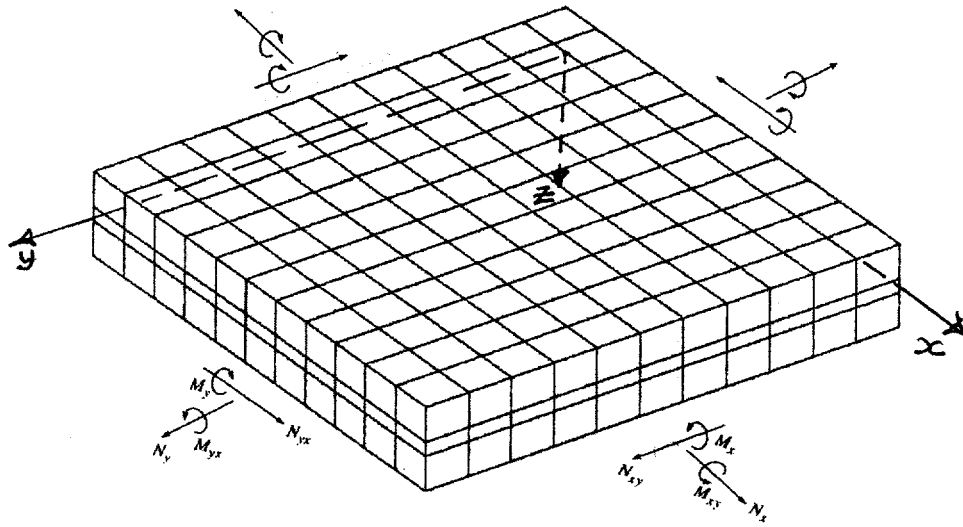
Figure 3.2   Coordinate System and Stress Resultant for PCB Plate.

According to Newton's second law, under static equilibrium conditions, the summation of forces along the x and y directions may be denoted as follows

$$N_x dy + \frac{\partial N_x}{\partial x} dx dy + N_{xy} dx + \frac{\partial N_{xy}}{\partial y} dx dy - N_x dx - N_{xy} dx = 0$$

$$(3.2)$$

$$N_y dx + \frac{\partial N_x}{\partial y} dx dy + N_{xy} dy + \frac{\partial N_{xy}}{\partial x} dx dy - N_y dx - N_{xy} dy = 0$$

$$(3.3)$$

These equations may be simplified as:

$$\frac{\partial N_x}{\partial x} + \frac{\partial N_{xy}}{\partial y} = 0 ....(a) \qquad\qquad \frac{\partial N_y}{\partial y} + \frac{\partial N_{xy}}{\partial x} = 0 ....(b)$$

$$(3.4)$$

Similar expressions can be derived for forces in z-direction, and the moments in both x and y directions. Making further simplification, the final expressions may be written as

$$\frac{\partial Q_x}{\partial x} + \frac{\partial Q_y}{\partial y} + q(x,y) = 0 \dotfill (a)$$

$$\frac{\partial M_x}{\partial x} + \frac{\partial M_{xy}}{\partial y} = Q_x \dotfill (b)$$

$$\frac{\partial M_y}{\partial y} + \frac{\partial M_{xy}}{\partial x} = Q_y \dotfill (c)$$

(3.5)

Substitution of equations 3.5b and 3.5c into 3.5a yields:

$$\frac{\partial^2 M_x}{\partial x^2} + 2\frac{\partial^2 M_{xy}}{\partial x \partial y} + \frac{\partial^2 M_y}{\partial y^2} + q(x,y) = 0$$

(3.6)

Equation 3.6 is in terms of stresses and moments. The corresponding equation in terms of displacements can also be derived based on force-deformation and strain-displacement relationships. The solutions to these equations can be found in several published literature [46, 47] and therefore will not be covered here. Additional equations required to describe the behavior of PCB to both out-of-plane buckling and transverse vibration are presented in the next two subsections for completeness.

3.2.1 PCB Buckling Analysis: In deriving equations 3.6 and 3.6, the coupling between the in-plane forces N_x, N_y, and N_{xy} and the out-of-plane deflections, **w** was ignored. This assumption was based on small displacement theory. This section will not use this assumption, rather, the coupling effects in deriving the expressions which may be used to predict laminate plate buckling response to in-plane loads will be incorporated. Consider differential elemental in figure. 3.3, and taking into account the vertical components of the in-plane forces, the summation of forces in the z direction becomes

$$\frac{\partial Q_x}{\partial x} + \frac{\partial Q_y}{\partial y} + q(x,y) + N_x \frac{\partial^2 w}{\partial x^2} + 2N_{xy} \frac{\partial^2 w}{\partial x \partial y} + N_y \frac{\partial^2 w}{\partial y^2} = 0$$

(3.7)
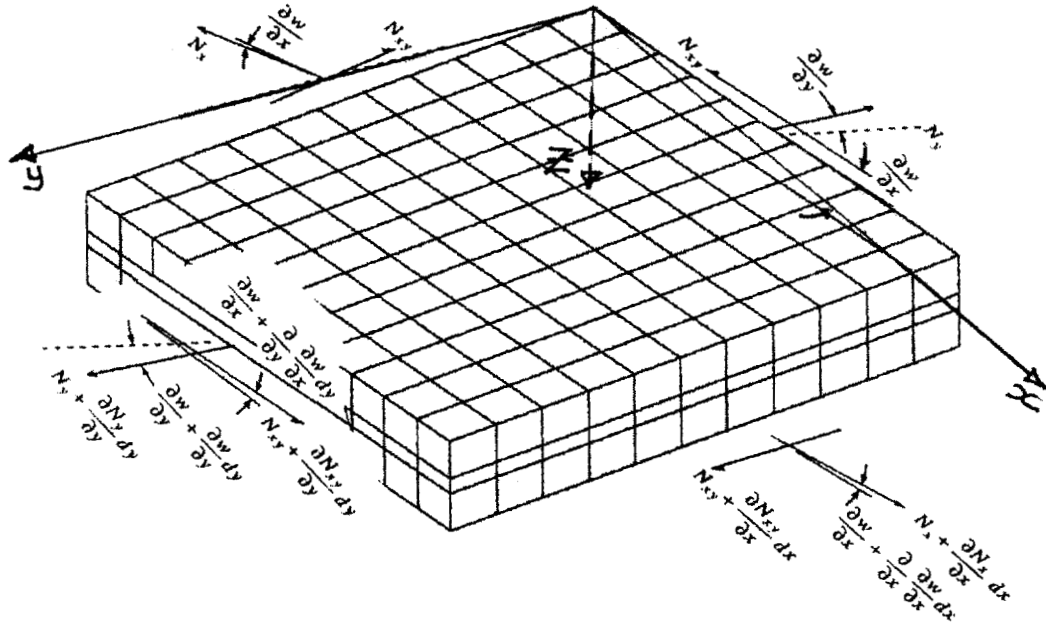
Figure 3.3   Stress Resultant and External Loads acting on PCB.

Combining equations (3.5b), (3.5c) and (3.7), will give equation (24)

$$\frac{\partial^2 M_x}{\partial x^2} + 2\frac{\partial^2 M_{xy}}{\partial x \partial y} + \frac{\partial^2 M_y}{\partial y^2} + 2N_x \frac{\partial^2 w}{\partial x^2} + 2N_{xy} \frac{\partial^2 w}{\partial x \partial y} + N_y \frac{\partial^2 w}{\partial y^2} + q(x, y) = 0$$

(3.8)

Equation (3.8) is similar to equation (3.6) above with additional terms involving the in-plane forces, which can cause the plate to buckle. For special cases, these equations may be reduced to reflect the boundary conditions associated with PCB support systems in a typical electronic packaging.

3.2.2 PCB Transverse Vibration: The general equations of motion for transverse vibration of a laminated plate can also be used to predict the response of PCB to dynamic loads, by modifying the static equilibrium equations for static deflection analysis and adding the inertia term according to Newton's second law. The summation of forces in x-direction (figure 3.4) is given by:

$$N_x dy + \frac{\partial N_x}{\partial x} dx dy + N_{xy} dx + \frac{\partial N_{xy}}{\partial y} dx dy - N_x dx - N_{xy} dx = \rho_o dx dy \frac{\partial^2 u_o}{\partial t^2}$$

(39)

Where:

ρ_o = mass per unit area of the laminate, i.e. $\rho_o = \rho h$

ρ = mass density of laminate is the per unit volume

h = thickness of laminate (note h is used instead of t).

$u_o = u_o(x, y, t)$, $v_o(x, y, t)$, and $w(x, y, t)$ is the middle surface displacement in x, y z directions respectively.

t = time

Similar equilibrium equations may be written for y-direction and the corresponding moments. Further simplification will result in the following differential equations of motion for laminated plates in terms of stress and moment resultants

$$\frac{\partial N_x}{\partial x} + \frac{\partial N_{xy}}{\partial y} = \rho_o \frac{\partial^2 w}{\partial t^2} \dots\dots\dots\dots(a)$$

$$\frac{\partial N_y}{\partial y} + \frac{\partial N_{xy}}{\partial x} = \rho_o \frac{\partial^2 w}{\partial t^2} \dots\dots\dots\dots(b)$$

$$(3.10)$$

$$\frac{\partial^2 M_x}{\partial x^2} + 2\frac{\partial^2 M_{xy}}{\partial x \partial y} + \frac{\partial^2 M_y}{\partial y^2} + q(x,y) = \rho_o \frac{\partial^2 w}{\partial t^2} \qquad (3.11)$$

Equations 3.10 and 3.11 form the foundation for formulating the finite element composite problem. The PCB, as a composite plate, is divided into four node (rectangular) or three node (triangular) isoparametric elements with each node having three rotational and three translational degrees-of-freedom (DOF). The principal displacements **u**, **v**, and **w** corresponding with **x**, **y**, **z** in 3D-coordinate system are related to the shape functions N_i , for the four node rectangular element as follows

$$u = N_1 u_1 + N_2 u_2 + N_3 u_3 + N_4 u_4 \dots\dots\dots\dots\dots(a)$$

$$v = N_1 v_1 + N_2 v_2 + N_3 v_3 + N_4 v_4 \dots\dots\dots\dots\dots(b)$$

$$(3.12)$$

$$w = N_1 w_1 + N_2 w_2 + N_3 w_3 + N_4 w_4 \dots\dots\dots\dots(c)$$

The corresponding nodal shape functions for the element are

$$N_1(\xi,\eta) = \frac{1}{4}(1-\xi)(1-\eta)\ldots\ldots\ldots\ldots(a)$$

$$N_2(\xi,\eta) = \frac{1}{4}(1+\xi)(1-\eta)\ldots\ldots\ldots\ldots(b)$$

(3.13)

$$N_3(\xi,\eta) = \frac{1}{4}(1+\xi)(1+\eta)\ldots\ldots\ldots\ldots(c)$$

$$N_4(\xi,\eta) = \frac{1}{4}(1-\xi)(1+\eta)\ldots\ldots\ldots\ldots(d)$$

Where ξ and η are used to define the natural coordinates system. For a thin element taken from the PCB and subjected to in-plane and transverse loads, the stresses and strains that produce the work for in-plane stress-strain state may be given by

$$\varepsilon_x = \frac{\partial u}{\partial x}\ldots\ldots\ldots\ldots(a)$$

$$\varepsilon_y = \frac{\partial v}{\partial y}\ldots\ldots\ldots\ldots(b)$$

$$\gamma_{xy} = \frac{\partial u}{\partial y} + \frac{\partial v}{\partial x}\ldots\ldots\ldots(c)$$

(3.14)

Similarly the strain-displacement (curvature) relations for the case of plate bending are

$$K_x = \frac{\partial^2 w}{\partial x^2} \dots\dots\dots\dots (a)$$

$$K_y = \frac{\partial^2 w}{\partial y^2} \dots\dots\dots\dots (b)$$ (3.15)

$$K_{xy} = \frac{\partial^2 w}{\partial x \partial y} \dots\dots\dots\dots (c)$$

Substituting equation 3.12 into equations 3.14 and 3.15 results in expressions for strain and curvature with respect to the element nodal displacement. From this point, the formulation of element stiffness matrix can be completed for each element so as to assemble the global stiffness matrices for the problem. Figure 3.4 shows epoxy-graphite PCB of dimensions 101.3mm x 203.2mm x 1.52mm thick, with several components mounted on it. Only one edge of the board is firmly supported by the chassis of the package box. When this system is exposed to an arbitrary shock load, the response history at point **A** in figure 3.4 will be used as the input base excitation force to analyze the model, see figure 3.1.
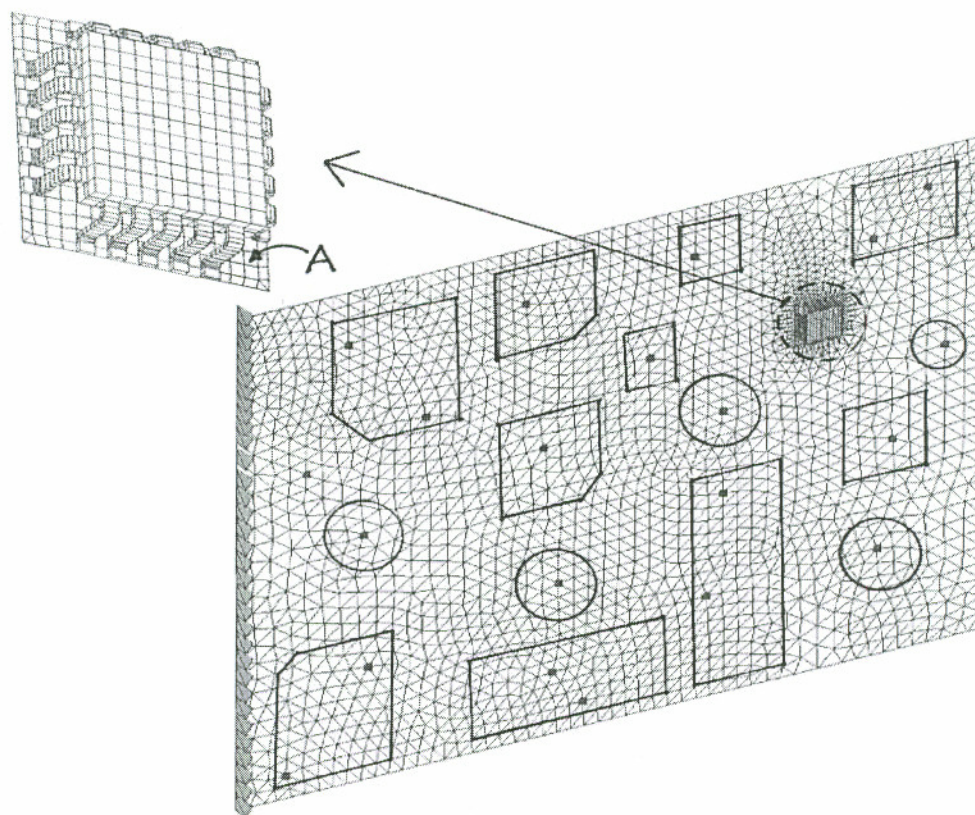
Figure 3.4   Epoxy-Graphite PCB showing Point A where base Excitation History was
Extracted.

3.2.3 PCB Vibration Transmissibility: Printed-circuit boards may be supported by the electronic box in many different ways, depending upon such factors as the environment, weight, maintainability, accessibility, and cost. The manner in which the PCB is supported is very important since it determines how the PCB responds to vibration and shock. With firm grip support, the PCB may reduce deflections that result from edge rotation and translation, and the PCB's natural frequency when subjected to either forced vibration or support excitation. [43, 48, 49] This implies that the forces that the individual component on the PCB may experience are dependent upon the PCB support conditions. The transmissibility equation derived in this section will be used subsequently to study how forces are transmitted from the package chassis to PCB, and then to the chip component. Consider the mass-spring-damper system shown in figure. 3.1, subjected to a harmonic force. Following the work of Chopra,[50] the force (f_T) transmitted to the base solder joint(s) is given by:

$$f_T = f_S + f_D = k.u(t) + c\dot{u}(t)$$

(3.16)

Where

$$u(t) = u_o \sin(\omega t - \phi) = \frac{P_0}{k} R_d \sin(\omega t - \phi))$$

(3.17a)

$$\dot{u}(t) = \frac{P_o}{\sqrt{k_m}} R_v \cos(\omega t - \phi)$$

(3.17b)

$$R_d = \tan^{-1}\left(\frac{2r\xi}{1 - r^2}\right)$$

(3.17c)

k, k_m = System spring constant.

$R_v = rR_d$

P_o = Amplitude of the applied force.

c = Damping parameter used to relate the types of motions to critical damping.

ω_n = Natural frequency of the system.

$\zeta = c/2m\omega_n$ Damping ratio or fraction of critical damping

ϕ = The phase angle which defines the time by which the response lags behind the force.

u_o = Displacement amplitude.

$r = \omega/\omega_n$

By substituting for the terms in equation 3.17 and making further simplification gives

$$f_T(t) = \left(\frac{p_o}{k}\right) R_d \left[k \sin(\omega t - \phi) + c\omega \cos(\omega t - \phi)\right]$$

(3.18)

Until now, we have assumed that the dynamic response is essentially the same as static deformation and therefore the system is controlled by stiffness only. Since the objective for this sub-section is to generate an expression for transmissibility of the system (**TR**), the maximum value of $f_T(t)$ in equation 3.17 over time **t** is taken to be $(f_T)_o$. Therefore, equation 3.17 can be written in a manner that produces the ratio of the maximum transmitted dynamic force P_o as

$$TR = \frac{(f_T)_o}{P_o} = \sqrt{\left(\frac{1 + (2r\xi)^2}{(1-r^2)^2 + (2r^2\xi)^2}\right)}$$

(3.19)

a)

k = spring constant

c = viscous damping constant
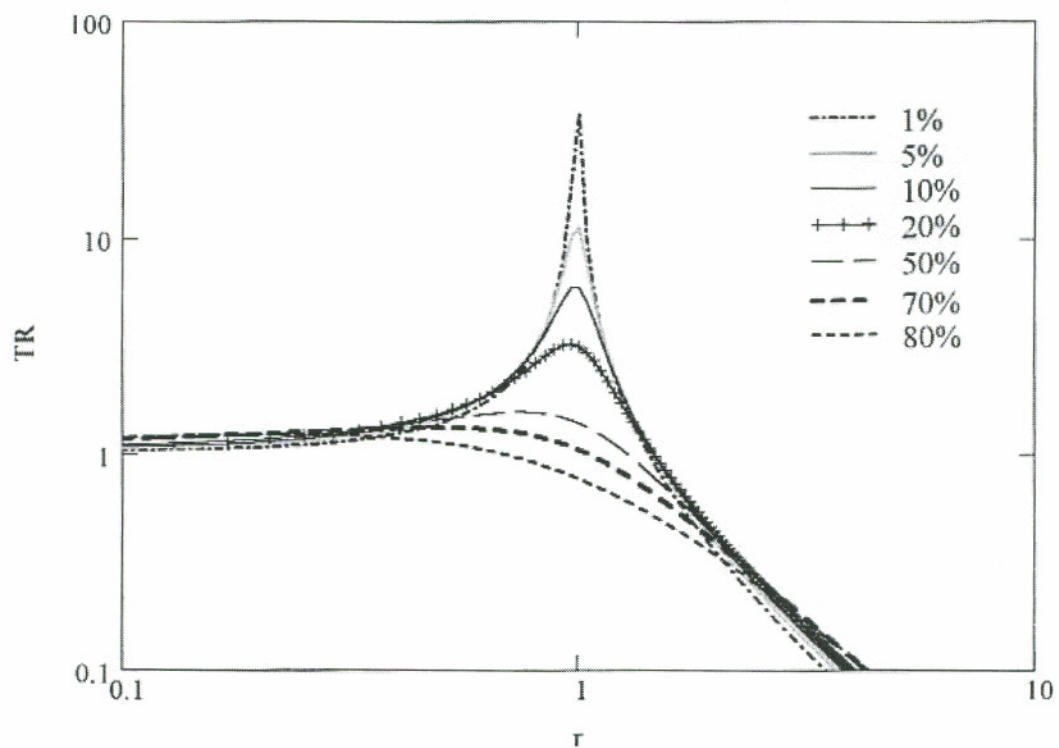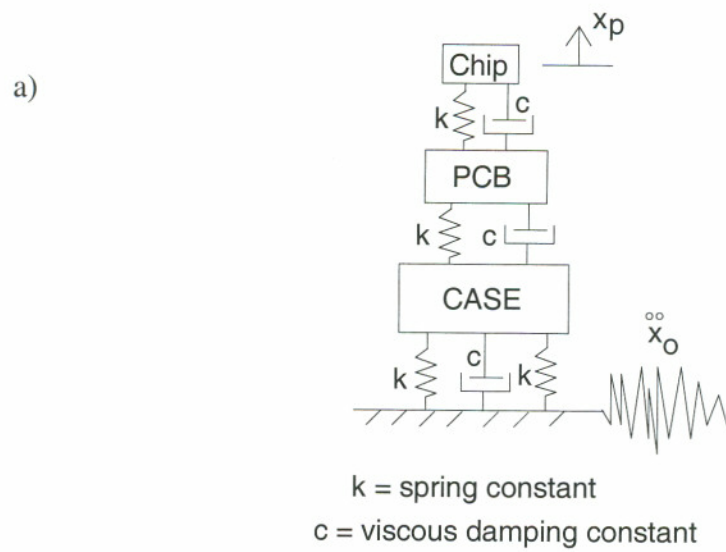
Figure 3.5   Transmissibility ($TR = X_p / X_o$) for Harmonic Excitation.

Following the above approach, an identical expression for transmissibility for the case when the applied force to the system is due to base excitation can be derived. In this case, Equation 3.18 can also estimate the ratio of base excitation (acceleration) transmitted to the mass and amplitude of base acceleration. In conclusion, it can be said that the transmissibility for base excitation problem is the same as for the system with applied force, and that equation 3.19 can be used to estimate its value. The transmissibility as a function of system frequency ratio is plotted in figure 3.5 using logarithmic scales. This was done to highlight the values of the region of interest, thus the higher frequency ratio values, particularly at **r =1.0**. for damping ratio between 0.01 to 0.05

3.3 Cooling Fluid (Air) Induced Vibration: The vibration due to the cooling fans and blowers create drag forces (forces in fluid direction), lift forces (forces perpendicular to fluid flow), and vortex shedding effects. Wong,[39] and works by many other researchers work support this claim. Turbulent boundary layers resulting from forced air cooling create a field of random pressure fluctuations on the walls of electronic packaging components. These pressure fields will induce vibration response of the package components. The level of vibration is typically in the linear range and hence its response can be found from the convolution integral of the pressure spectral density and that of the dynamic responses of the component [51]. Under extreme conditions, excessive amplitude due to vibration could result in pounding, which is a phenomenon that describes the situation when one electronic component strikes an adjacent component. This action induces higher forces in the component solder joints, which may undermine the joint integrity. To describe cooling air induced vibrations, the work of Krenk [52] will be adopted and modified where appropriate, to the unique problem depicted in figure. 3.1

Consider electronic component of length **L**, and width **D** with mass **m₀**, supported by linear springs **k** damping ratio ξ₀ in a fluid with mass density ρ, and undisturbed flow velocity **u** as shown in figure. 3.6.
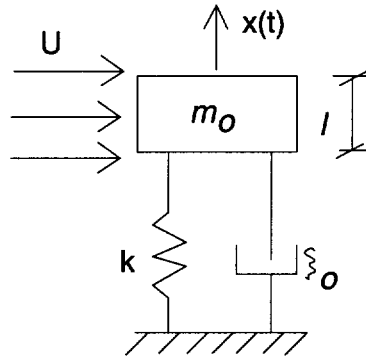
Figure. 3.6 Cooling Air Induced Vibrations of Electronic Component in Cross-flow.

Assuming that the component can move only in the x-direction, the displacement x (t) and the corresponding equation of motion can be expressed in the form of:

$$m_o\left(\ddot{x} + 2\xi_o\omega_o\dot{x} + \omega_o^2\right) = \frac{\rho}{2}U^2C_LDL$$

(3.20)

Where

C_L = non-dimensional lift coefficient corresponding to fluid flow around the mass, assuming that Reynolds number is small.

ω_o = Circular eign-frequency.

If we assume that the force exerted by the fluid on the mass in the direction of motion to be proportional to the relative velocity of the fluid mass, then an expression for lift coefficient as a function of time is given by

$$C_L = \frac{\dot{w}(t)}{U}\gamma$$

<div align="right">(3.21)</div>

Where

  γ = Non-dimensional coupling parameter assumed constant for this work.

  w(t) = The transverse velocity of the fluid mass

Making substitution for the lift coefficient term in equation 3.21 the resulting equation of motion is

$$m_o\left(\ddot{x} + 2\xi_o\omega_o\dot{x} + \omega_o^2\right) = \frac{\rho}{2}U^2 C_L DL\frac{\dot{w}(t)}{U}\gamma$$

<div align="right">(3.22)</div>

If the forcing term of the fluid oscillator is assumed to contain the velocity of the mass x(t) as a factor, then by requirement, the rate of energy transferred to the mass by means of the right-hand side of equation 3.22 must be identical to the rate of energy extracted from the fluid oscillator. Therefore, the equation of motion of the fluid oscillator with quadratic damping is given by:

$$m_f\left\{\ddot{w} - 2\xi_f\omega_s\left(1 - \frac{w^2 + \frac{\dot{w}^2}{\omega_s^2}}{w_o}\right)\dot{w} + \omega_s^2 w\right\} = -\frac{\rho}{2}U^2 DL\frac{\dot{x}(t)}{U}\gamma$$

<div align="right">(3.23)</div>

Where

m_f = Equivalent mass of the fluid oscillator, proportional to the fluid mass density ρ and volume of the structure.

w_o = A parameter that controls the amplitude of self-induced vibrations of the fluid in the case of stationary mass.

ξ_f = Equivalent fluid damping ratio. It represents the sensitivity of the energy source to changes in fluid oscillation amplitude.

Now, we can limit the discussion to the case of stationary mass, typical of what is found in electronic packaging environment, the solution to equation 3.23 is given by

$$w(t) = w_o \sin(\omega_s t + \phi)$$

(3.24)

And the corresponding lift coefficient exhibiting harmonic vibrations with amplitude C_{LO} is given by

$$C_{LO} = 2\pi S \frac{w_o}{D} \gamma$$

(3.25)

Where

ϕ = Arbitrary phase angle

S = Strouhal Number, usually in order of approximately 0.2 [53]

ω_o = Prescribed equivalent fluid amplitude.

Finally, in line with the work of Krenk,[52] the normalized fluid oscillator amplitude **B** is given by

$$B = \left\{ \left[\frac{4\omega_s^2}{\omega_s^2 + 3\omega^2} \right] \left[1 - \left(\frac{\xi_o \omega_o}{\xi_f \omega_s} \right) \left(\frac{\omega_s^2 - \omega^2}{\omega_s^2 - \omega^2} \right) \right] \right\}^{\frac{1}{2}}$$

(3.26)

And the normalized structural amplitude **A**, may be expressed in terms of fluid oscillator amplitude **B** and the lift coefficient C_L respectively as

$$A = \frac{\mu_f C_o \left(\dfrac{\omega_s}{\omega_o}\right)\left(\dfrac{\omega}{\omega_o}\right) B}{\left\{\left[1-\left(\dfrac{\omega}{\omega_o}\right)^2\right]^2 + 4\xi_o^2\left(\dfrac{\omega}{\omega_o}\right)^2\right\}^{\frac{1}{2}}} \qquad (3.27)$$

$$A = \frac{1}{2}\mu_f\left(\frac{U}{D\omega_o}\right)^2 C_L\left\{\left[1-\left(\frac{\omega}{\omega_o}\right)^2\right]^2 + 4\xi_o^2\left(\frac{\omega}{\omega_o}\right)^2\right\}^{-\frac{1}{2}} \qquad (3.28)$$

Thus for a given electronic component system (see figures. 3.1 and 3.5), subjected to cooling air loads, the structural amplitude can be determined from equation 3.28. The relative fluid mass μ_f, the square of the reduced velocity $U/D\omega_o$, the lift coefficient C_L, and the amplification factor of the linear structural oscillator are the required parameters in order to find the system response.

3.4   Response to Impulse Loading: As stated earlier, electronic components are frequently exposed to many different forms of vibration over wide frequency ranges and acceleration levels. Impulse loads such as repeated impact of typing keys on laptops and shocks are special classes of dynamic loading electronic packages may be subjected to during the lifetime of the device. Such load normally consist of a single principal impulse of arbitrary form and generally is of relatively short duration.[42, 43, 54-57] Damping has much less importance in controlling the maximum response of a structure to particular impulse load, than for periodic or harmonic loads because the maximum response to a particular

impulse load will be reached in a very short time before the damping forces can absorb much energy from the structure.

Let us consider one-degree-freedom systems such as the one shown in figure. 3.6, subjected to arbitrary forcing functions shown in figure 3.7.
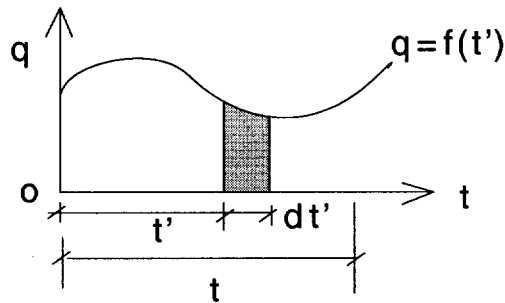
Figure 3.7　　General impulsive loading function.

The equation of motion is given by:

$$m\ddot{u} + c\dot{u} + ku = Q = F(t')$$　　(3.29)

Dividing equation 3.29 by the mass **m** and rearranging terms results in the following:

$$\ddot{u} + 2n\dot{u} + \omega^2 u = q$$

(3.30)

Where

$$q = \frac{Q}{m} = \frac{F(t')}{m} = f(t')$$

The expression for **q** was derived by considering the shaded area under the curve in figure 3.7. At time **t**, during the interval **dt'**, the shaded area is equal to **q.dt**. This impulse force acting on a body produces an instantaneous change in velocity, which can be determined from Newton's law of motion as:

$$d\dot{u} = qdt'$$

(3.31)

Equation 3.31 is valid irrespective of other conditions such as spring force, displacement, and velocity that may be acting upon the system at time instant **t**. If we consider this incremental velocity as the initial velocity at time **t**, and the initial displacement to be zero, then we can conclude that the incremental displacement of the system at any later time **t** may be given by:

$$du = e^{-n(t-t')} \frac{qdt'}{\omega_d} \sin \omega_d (t - t')$$

(3.32)

This implies that, the loading function may be regarded as a series of short impulses at successive incremental times **dt'**, with each producing its own differential response at time **t** of the form given by equation 3.32. Therefore we may conclude that the total displacement at time **t** due to the continuous action of the force **q** is given by the summation of the differential displacement equation, from time **t'= 0** to time **t'= t**, that is

$$u = \frac{e^{-nt}}{\omega_d} \int_0^t e^{-nt} q \sin \omega_d (t - t') dt' \qquad (3.33)$$

The integral in equation 3.33 is known as a Duhamel integral. This equation represents the complete displacement produced by the disturbing force **q** acting during the time interval **0** to **t**. It includes both steady state and transient terms of the motion corresponding to zero initial conditions for both displacement and velocity. If the function **q=f(t′)** cannot be expressed analytically, then the integral in equation 3.33 can be evaluated approximately by suitable numerical integration methods. Therefore, for a given single degree-of-freedom (SDOF) system, the total solution can be obtained by adding equation 3.33 to the effects due to the initial conditions. Thus, the total solution is given as

$$u = e^{-nt} \left[u_o \cos \omega_d t + \left(\frac{\dot{u}_o + nu_o}{\omega_d} \right) \sin \omega_d t + \frac{1}{\omega_d} \int_0^t e^{nt'} q \sin \omega_d (t - \tau) d\tau \right]$$

$$(3.34)$$

If the damping effect is neglected due to the short duration of the applied force, then we have a condition in which **n = 0**, $\omega_d = \omega$, and therefore equation 3.33 reduces to

$$u = \frac{1}{\omega} \int_0^t q \sin \omega (t - \tau) d\tau \qquad (3.35)$$

The corresponding total solution including the initial conditions for both displacement **u_o** and velocity **u_o** evaluated at time **t = 0**, without damping is given as

$$u = \left[u_o \cos \omega t + \left(\frac{\dot{u}_o}{\omega} \right) \sin \omega_d t + \frac{1}{\omega} \int_0^t q \sin \omega_d (t - \tau) d\tau \right] \qquad (3.36)$$

Finally, equations 3.35 and 3.36 may be use to evaluate special vibration load cases, for instance, when a building office floor system supporting an electronic component is excited due to a person walking across the floor. This type of vibration will produce a sequence of approximately rectangular impulses [38] shown in figure 3.8. The time difference between the successive step functions, that is $t_{n-1} - t_n$ can be specified as $\tau/2$ so that the impulsive action is always in phase with the velocity to do a positive work on the system for each cycle of vibration.
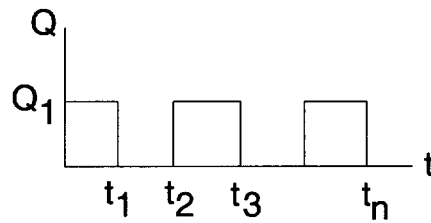
Figure 3.8   Rectangular Footstep Impulses due to a Person Walking Across an Office Building Floor.

The forcing function shown in figure 3.8 can be considered as a series of rectangular impulses with their origins shifted on the time scale except the first rectangle. Therefore, the general solution to rectangular impulse may be used for the forcing function shown in figure 3.8 with some modification [57]. From the principle of superposition, we can conclude that the amplitude of the function after n rectangular pulses is given by

$$A_n = \frac{2nQ_1}{k}$$

(3.37)

That is, in every cycle of vibration, the amplitude increases by $2Q_1/k$, and for undamped system we can say, the response will build up indefinitely. Therefore, from a practical point of view, only the first few cycles are normally used for analysis. The corresponding displacement response of the system is also given by

$$u = \frac{2nQ_1}{k}\left[\cos\omega(t - t_n) - \cos\omega t\right] \qquad (3.38)$$

For convenience, we will let the ratio of displacement at time t to the static displacement Q_1/k be defined as the dynamic load factor (DLF). Then, equation 3.38 can be written in dimensionless form if we use the relationship between the natural period of the system T and the natural frequency ω, that is $\omega = 2\pi/T$, hence:

$$DLF = 2n\cos 2\pi\left(\frac{t}{T} - \frac{t_n}{T}\right) - \cos 2\pi\frac{t}{T} \qquad (3.39)$$

We conclude this subsection by saying that, any periodic forcing function in resonance with the system will give large amplitudes of forced vibrations if it does positive net work cycle based on equation 3.38. Secondly, the dimensionless parameter DLF, given by equation 3.39 emphasizes the quantity of importance. That is, the ratio of duration of time to the constant force is applied to the natural period rather than the actual value of the time quantity contained in equation 3.38.

3.5   Random Vibration: Many researchers believe that stochastic processes adequately represent the true loading environment a typical electronic component will experience.[55] Also, from a reliability standpoint, the method has proven to be a powerful analytical tool for improving electronic components against defects at both manufacturing and assemblying stages. Random vibration is a unique dynamic load in that, when acting on an electronic component, the instantaneous value of loading process cannot be predicted in a deterministic sense unlike other structural dynamics methods including those presented before in this chapter. For a given bandwidth and at any instant of time, all the frequencies of vibration may be present. That is, all the structural resonance(s) of the system within the bandwidth may be excited at the same time, which may cause the system to fail since at resonance, the amplitude of the system will increase rapidly. Therefore the objective of this section is to introduce the necessary random vibration theory equations essential for analyzing the computational modal as shown in figure 3.1, when excited by dynamic loads in stochastic processes.

Let us consider electronic components with **n** accelerometers mounted on it as shown in figure 3.9. The system is then subjected to base excitation. The recorded accelerometers signals x_i (t) (i =1, 2, . . . n) which are functions of one independent variable time **t**, in a waveform might look differently from each other, that is x_r (t) $\neq$ x_s (t) for **r** $\neq$ **s**. To characterize this process x(t) in a probabilistic sense, it is necessary to establish   a multivariate probability density function $p(x_1, x_2, ... x_m)$, as defined by

$$p(X_1, X_2, \ldots \ldots X_m) dx_1 dx_2 \ldots \ldots dx_m$$
$$\equiv \Pr(X_1 \prec x_1 \prec X_1 + dx_1, X_2 \prec x_2 \prec X_2 + dx_2, \ldots \ldots, X_m \prec x_m \prec X_m + dx_m)$$

$$(3.40)$$

Where **m = 1, 2,...,** x_i equals the random variable consisting of the sample **values** x_{i1}, x_{i2}, ... x_{im} across the ensemble at time t_i. It is normally assumed that the first two of the functions, **p** (x_1) and **p** (x_1, x_2) and time variable t_1 and t_2 are sufficient to describe many random processes, associated with engineering systems.
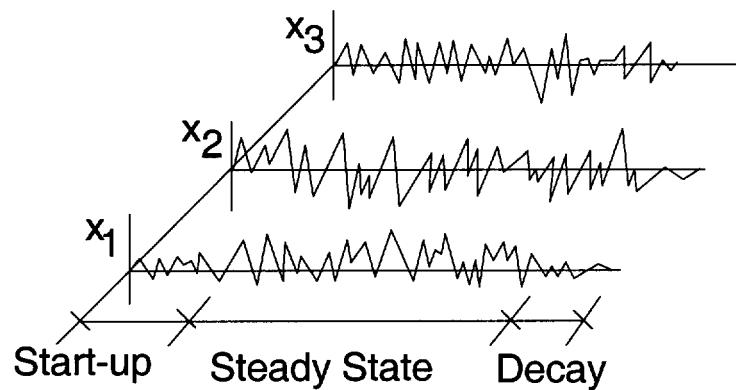
Figure 3.9   An Ensemble of Equally Probable Random Functions.

Stationary and Ergodic Processes: A random process is stationary if its standard deviation and spectral density for the time increment ΔT_1 are approximately the same as for the time increment ΔT_2, shown in figure 3.10. In addition, if the average value obtained with respect to time for any member of the ensemble is equal to the average across the assemble at an arbitrary time t_i, then the random process is called Ergodic. Thus in a stationary and ergodic processes, a single record may be used to obtain the statistical description of the random function.

Figure 3.10   Characteristics of Non-Stationary (left) and Stationary (right) Processes.

Statistical parameters[58-61] useful in describing a random process x_i (t) (i = 1, 2, ...n) are given below

$$\bar{x} = \frac{1}{T}\int_0^T x(t)dt \dots\dots(a)$$

$$\bar{x}^2 = \frac{1}{T}\int_0^T x^2(t)dt \dots\dots(b)$$

$$\sigma_x^2 = \frac{1}{T}\int_0^T [x(t) - \bar{x}]^2 dt = \bar{x}^2 - (\bar{x})^2 \dots\dots(c)$$

$$\sigma_x = \sqrt{\bar{x}^2 - (\bar{x})^2} \dots\dots(d)$$

$$RMS_x = \sqrt{\bar{x}^2} \dots\dots(e)$$

(3.41)

Where equation 3.41a-e represent the sample mean, mean-square value, sample variance, standard deviation, and root mean-square (see figure 3.11) of the process respectively.
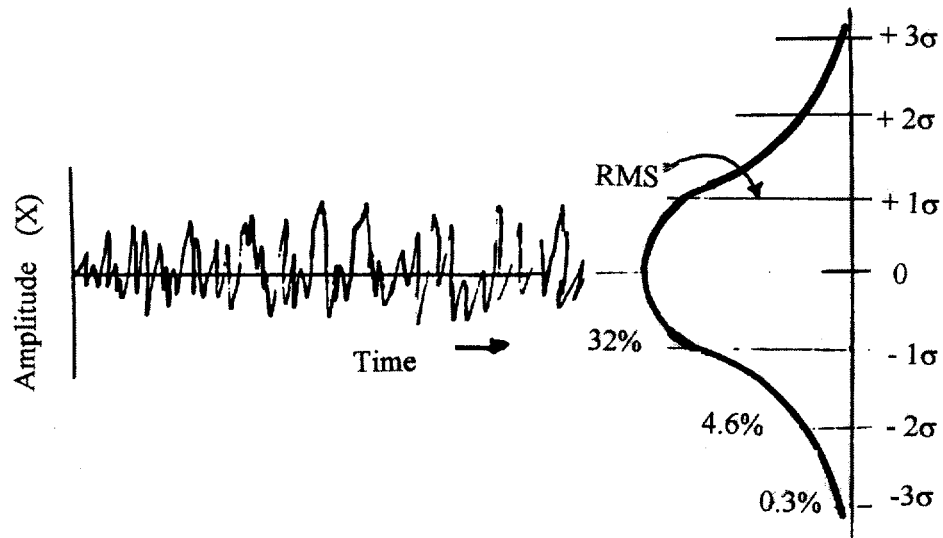
Figure 3.11   Random Process with Normal Amplitude Distribution.

Also for a given normal probability density function, the probability that a random variable x (t) has a value between x_n and x_n+1 is given by

$$p(x_n \leq x \leq x_{n+1}) = \int_{x_n}^{x_{n+1}} p(x)dx$$

(3.42)

Similarly the probability of x being greater than X_m, that is, $p(|x| > X_m)$ can be represented by the two shaded-tail area of the normal probability density function, since every real x will fall within the interval ($-\infty$ to ∞), whereby the area of the function may found as:

$$\int_{-\infty}^{\infty} p(x)dx = 1$$

(3.43)

Where p(x) is the function for normal distribution or Gaussian distribution expressed as

$$p(x) = \frac{1}{\sigma\sqrt{2\pi}} e^{-\frac{(x-\bar{x})^2}{2\sigma}} \dots\dots\dots\dots(-\infty \leq x \leq \infty)$$

(3.44)

Autocorrelation function for stationary Process: Correlation is defined as the measure of the dependence of two random processes. For a general random process in which $x_1(t)$ is identical to x(t) but shifted on the time scale by certain amount τ, that is $x_1(t) = x(t + \tau)$, the autocorrelation $R(\tau)$ may be given as

$$R(\tau) = \lim_{\to T=\infty} \frac{1}{T} \int_0^T x(t)x(t-\tau)dt$$

(3.45)

Where $\tau=0$, then equation 3.45 will reduce to the mean-square value expressed as

$$R(0) = \lim_{\to T = \infty} \frac{1}{T} \int_0^T [x(t)]^2 \, dt = \bar{x}^2$$

<div align="right">(3.46)</div>

The importance the autocorrelation function concept in random vibration can be highlighted as follows. Given a general stationary process with zero mean value $\bar{x} = 0$, and has Gaussian distribution, the autocorrelation function $R(\tau)$ can completely characterized the process since all the variance and covariance functions in equation 3.41 is directly related to the autocorrelation function (see figure 3.11) as follows

$$u_{ij} = \begin{cases} R(0) & i = j & (variance) \\ \\ R(\tau) & i \neq j & (covariance) \end{cases} \quad \ldots\ldots\ldots\tau = t_j - t_i$$

<div align="right">(3.47)</div>

Spectral Analysis: When the contributions of the frequency components of **x(t)** results in the value $\bar{x}^2$, the function x(t) is referred to as the spectral function. In order for this to happen, the coefficients of the Fourier series or its equivalent for the case of non-periodic functions, should be transformed into integral expression given by

$$\bar{x}^2 = \frac{1}{T} \int_0^T x^2(t) dt$$

$$= a_0^2 + \sum_{n=1}^{\infty} \left[\frac{a_n^2}{2} + \frac{b_n^2}{2} \right]$$

<div align="right">(3.48)</div>

Where for the case of periodic functions x(t) with period T, and $\omega = 2\pi/T$, is expressed in Fourier series form as

$$x(t) = a_0 + \sum_{n=1}^{\infty}(a_n \cos n\varpi t + b_n \sin n\varpi t)\ldots\ldots\ldots(a)$$

$$a_0 = \frac{1}{T}\int_0^T x(t)dt\ldots\ldots\ldots(b)$$

$$a_n = \frac{2}{T}\int_0^T x(t)\cos n\varpi t\, dt\ldots\ldots\ldots(c)$$

$$b_n = \frac{2}{T}\int_0^T x(t)\sin n\varpi t\, dt\ldots\ldots\ldots(d)$$

$$(3.49)$$

Similarly the mean-square value for the non-periodic functions case, having discrete time function $F(t_j)$ (j = 0, 1, 2, .. N-1) may also expressed in discrete Fourier transform as:

$$\overline{F}^2 = \frac{1}{T}\sum_{j=0}^{N-1}F^2(t_i)\Delta t = \sum_{n=0}^{N-1}C_n C_n^*$$

$$= \sum|C_n|^2 = |C_0|^2 + |C_1|^2 + \ldots\ldots|C_{N-1}|^2$$

where

$$F(t_j) = \sum_{n=0}^{N-1}C_n e^{2\pi i \frac{nj}{N}}$$

$$C_n^* = \frac{1}{N}\sum_{j=0}^{N-1}F(t_j)e^{2\pi i \frac{nj}{N}}$$

$$C_n = \sum_{j=0}^{N-1}F(t_j)e^{-2\pi i \frac{nj}{N}}$$

$$(3.50)$$

Equations 3.48 and 3.51 are the spectrum of the function x(t) for both periodic and non-periodic functions respectively. Each of the terms in the series in equation 3.48 reflects the corresponding contribution of frequency to the mean-square value for the periodic case. For the non-periodic case, the contribution to the mean-square is due to the square of the modulus of the corresponding complex coefficients C_n given by equation 3.51.

Spectral Density Function: Using spectral analysis concepts presented above, the autocorrelation function given by equation 3.45 of a random process can be related to spectral density function obtained experimentally. Given a normalized random process such that the mean value is zero, and the function itself has no periodic components, the autocorrelation in terms of spectral density function is given by

$$R_x(\tau) = \int_{-\infty}^{\infty} S_x(\omega) e^{i\omega\tau} d\omega = \bar{x}^2$$

$$(3.51)$$

Where the spectral density function $S_x(\omega)$ of x(t) is expressed as

$$S_x(\omega) = \frac{1}{2\pi} \int_{-\infty}^{\infty} R(\tau) e^{-i\omega\tau} d\tau$$

$$(3.52)$$

Using Euler's relationship, i.e. $e^{i\omega\tau}$ = cos ωτ + i sin ωτ, equations. 3.51 and 3.52 may simplified as

$$R_x(\tau) = 2\int_{0}^{\infty} S_x(\omega) \cos \omega\tau \cdot d\omega \qquad (3.53)$$

$$S_x(\omega) = \frac{1}{\pi} \int_{0}^{\infty} R_x(\tau) \cos \omega\tau \cdot d\tau \qquad (3.54)$$

Equations 3.53 and 3.54 are known as the Wiener-Kinchin equations. They describe how the autocorrelation function can be determined from spectral density function and vice

versa. Also, for a given spectral density function, the area under the curve is equal to the mean-square value of the random process given by equation 3.51. In closing this section, it is noteworthy that, when a random process spectral density has nonzero values in a narrow frequency range, the process is referred to as a narrow-band process. Likewise if the nonzero values are spread over broader range, the process is called wide-band.

Given a random excitation process, its impact on a structural system may be dependent on the frequency content of the excitation function. Therefore the ability to estimate the spectral function or spectral density function of the process is desirable. Consider a Single DOF system subjected to a random force **F(t)** and if we assumed that the function is known at **N** discrete equally spaced times, i.e. **tⱼ = Δtⱼ (j = 0, 1, 2, ...N-1)**, using superposition principles, the response of the system to the harmonic frequency components obtained by Fourier analysis of F(t) using equation 3.50 is given by

$$y(t_j) = \sum_{n=0}^{N-1} \frac{C_n e^{\frac{2\pi i n j}{N}}}{k(1 - r_n^2 + 2ir_n\xi_n)}$$

(3.55)

Where $\omega_n = n\varpi$ for $n \leq N/n$

$\omega_n = -(N-n)\varpi$ for $n \geq N/n$

$r_n = \omega/\omega$

$\varpi = 2\pi/T$

$\omega = (k/m)^{0.5}$

ξ_n = Damping ratio based on ω_n

k = system stiffness

T and N represent the time duration of excitation and the number of equal interval of excitation respectively.

Equation 3.55 gives the response of the single DOF system subjected to stochastic processes. The mean-square value based on equation. 3.55 is

$$\bar{y}^2 = \frac{1}{k^2} \sum_{n=0}^{N-1} |H_n|^2 |C_n|^2$$

(3.56)

where

$$H_n = \frac{1}{1 + r_n^2 + 2ir_n\xi_n}$$

Similarly, when the stochastic process is random, acceleration applied to the support of the structure, the mean-square value of the response at point **p** of the structure is given by

$$\bar{a}_p^2 = \frac{1}{k^2} \sum_{n=0}^{N-1} S(\omega_n)|H_n|^2 \Delta\omega$$

(3.57)

When the spectral density function $S_F(f_n)$ of the stochastic excitation is know, the modified form of equation 3.56 may be written in terms of cycles per seconds (cps) units as

$$\bar{y}^2 = \sum_{n=0}^{N-1} S_y(f_n)\Delta f$$

where

$$S_y(f_n) = \frac{1}{k^2}|H_n|^2 S_F(f_n)$$

(3.58)

Equation 3.58 will be used to estimate the response of the research model (see figure 3.1 and 3.12) when subjected to base excitation. Application to Electronic Packaging Unit: Consider electronic package unit in figure 3.12, acted upon by base excitation. The system response in terms of displacement, accelerations, and stresses may be computed statistically in the following manner.
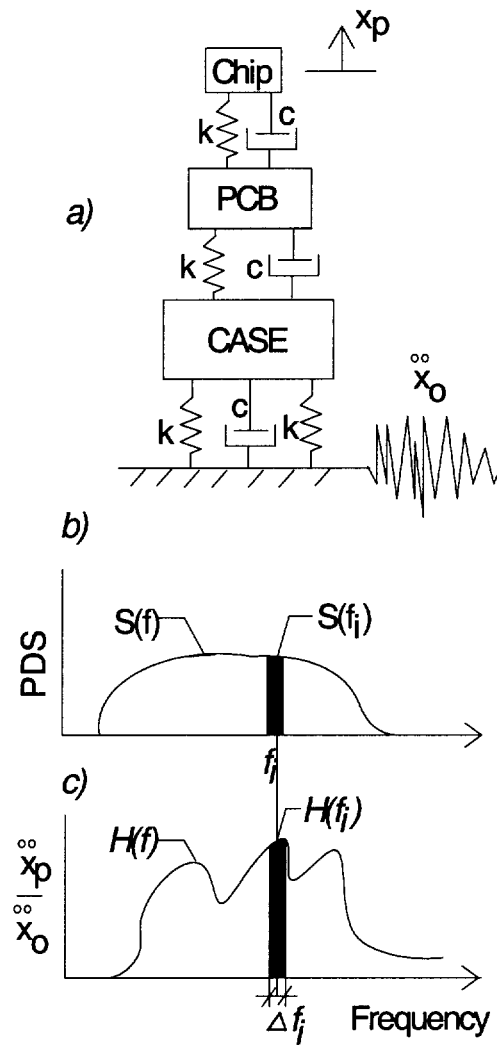
Figure 3.12   Representation of the Chassis, PCBs, and the Chip of a Electronic Unit as a
3-DOF System. (a) Dynamic under base excitation, (b) Base Acceleration
Spectral Density and (c) Frequency Response Function at the Chip level
(Transmissibility).

The mean square response acceleration at the chip level x_p, in figure 3.12, where the PSD

notations $S_x(\omega)$ and H(f) used in equations 3.50 and 3.54 have been changed to S(f) and

H_n, respectively, and can be calculated numerically using equation 3.57. Also the PSD

curve for the response at the chip level may be calculated by using equation 3.58, which

will give the area under the PSD curve. Therefore for processes that follows Gaussian

distribution, the probability of exceeding certain acceleration levels at any given point in time may be given as

$$PROB.[\ddot{x}_p > 1\sigma] = 31.7\%$$
$$PROB.[\ddot{x}_p > 2\sigma] = 4.6\%$$
$$PROB.[\ddot{x}_p > 3\sigma] = 0.3\%$$

(3.59)

It is assumed that the equations of motion for the structural system have been established and decoupled into generalized coordinates by modal analysis. Once this is done, the calculation of a covariance matrix σ, which takes into account the cross modal coupling between the eigenvector displacement components ϕ_N and ϕ_M can be made. The σ matrix coefficients are expressed in terms of displacement, velocity and or acceleration. The variance or the mean square displacements, velocities, accelerations and stresses in terms of σ^2 can then be calculated by

$$\sigma^2_{DISP}(x_i) = \sum_N \sum_M \phi_N(x_i)\phi_M(x_i)\sigma_{DISP}$$

$$\sigma^2_{ACCEL}(\ddot{x}_i) = \sum_N \sum_M \phi_N(x_i)\phi_M(x_i)\sigma_{ACCEL}$$

(3.60)

$$\sigma^2_{STRESS}(e_i) = \sum_N \sum_M \psi_N(e_i)\psi_M(e_i)\sigma_{STRESS}$$

Where x_i, x_i are displacement and accelerations of point i on the structure, ϕ_N, ϕ_M =are the eigenvector displacement components for all points on the structure for modes N and M, e_i is the ith element in the structure, and ψ_N, ψ_M = are the modal stress vectors in all the elements of the structure associated with the eigenvector displacements ϕ_N and ϕ_M. These concepts presented in this chapter are use in chapter 6 in formulating the global finite element model.

CHAPTER FOUR

THERMAL LOAD EQUATIONS FORMULATIONS

4.1   HEAT TRANSFER OVERVIEW: The trend in microelectronic packaging continues to be towards greater packaging density, speed and higher heat dissipation in both chip package and printed circuit boards (PCB) and has made the task of device cooling and thermal management in general, very important and challenging. [62-65] Device power levels are rapidly increasing making thermal management the central underpinning subject of electronic package reliability. Heat transfer analysis and thermal stress including stress-strain predictions at the solder joints have been studied by many researchers.[66-74] In view of this fact, this section of the dissertation will be limited to thermal resistance network method as a tool, as applied to the research model shown in figure 3.1.

When an electric current flows through a resistor, it produces heat that mathematically can be expressed as I^2R, where I is the current and R is the resistance. As a result, the heat generated in the resistive element will remain as long as the current continues to flow through it. This action generates heat build- up in the unit and a subsequent temperature rise at and around the packaging system which can be computed and converted to equivalent mechanical loads for use in design and operating criteria of components. Heat sinks, mechanical devices with extended surface designed to provide increased surface area to dissipate heat generated by electronic components to the cooling air, are commonly used to enhance the cooling of electronic components. While the heat sink provides an effective means of removing heat from electronic components, it also creates an additional solid mass on the components, which may affect the overall reliability of the electronic packaging especially when subjected to vibration or shock loading.

4.2 **Thermal Resistance Networks**: To determine the lead frame-to-solder joint temperature difference for given package component, the thermal resistance network method is introduced. This method greatly simplifies the first-order thermal analysis of electronic packaging system, mathematically, [75-77] and also enables the smooth transition from the thermal analysis problem setup to problem optimization formulation discussed later in chapter 6. Beginning from an electrical engineering analogy where the current passing through resistor is given by:

$$I = \frac{V_1 - V_2}{R_e} \tag{4.1}$$

Where

I = electric current flow

$V_1 - V_2$ = voltage difference across the resistance

Equation 4.1 is analogous to that of heat flow in an electronic component, which in general can be represented by

$$R_T = \frac{T_j - T_f}{q_c} \tag{4.2}$$

Where

$T_j - T_f$ = the junction and fluid (coolant) temperatures, respectively.

q_c = the component heat dissipation.

R_T = the thermal resistance, and is a function of the component geometry and the thermal properties.

4.3   Thermal Network and Heat Transfer Modes: In general, heat transfer consists of three different modes, namely conduction, convection, and radiation [62, 78]. Each mode of heat transfer requires the existence of a temperature difference, that is, heat travels from a high temperature region to a low temperature region for a given medium. Therefore, in electronic packaging, a one-dimensional thermal analysis method (thermal resistance) can be used based on conduction and convection heat transfer modes theories to predict both the hot and low temperature regions as discussed in detail next.

4.3.1   Conduction Cooling: Is the transfer of heat in which energy exchange takes place from the region of high temperature to that of low temperature by kinetic motion or direct impact of molecules, or by drift of electrons in the case of metals. The rate of heat conduction through a medium depends on the following factors:

- Medium Geometry
- Medium Thickness
- Medium Material
- Temperature difference across the medium

In rectangular coordinates, the general governing differential equation for three-dimensional conduction heat transfer analysis is given by:

$$\frac{\partial}{\partial x}\left(k\frac{\partial T}{\partial x}\right)+\frac{\partial}{\partial y}\left(k\frac{\partial T}{\partial y}\right)+\frac{\partial}{\partial z}\left(k\frac{\partial T}{\partial yz}\right)+g=c_p\rho\frac{\partial T}{\partial t} \qquad (4.3)$$

Where:

k = The thermal conductivity of a material

T = Medium temperature

g = Heat generated per unit volume

c_p = Heat capacity

ρ = Material density

t = Time

If we consider an electronic package element connecting node-**A** and node-**B**, with the distance between the nodes denoted by $L = x_B - x_A$, and having cross-sectional area A_e, the one-dimensional, steady state approximation equation 4.3 (Fouriers Law) can be written as

$$Q_e = -kA_e \frac{T_A - T_B}{L} \tag{4.4}$$

Where it is assumed that the temperature variation between the two nodes is linear. Solving for temperature difference over the element length **L** in equation 4.4 will yield

$$T_A - T_B = Q_e \left(\int_A^B \frac{dx}{kA_e} \right) = Q_e R_e \tag{4.5}$$

Where R_e and Q_e are the element thermal resistance and heat input respectively. For the special case where the bonding interface between the solder joint contains microscopic voids which may caused the temperature to drop at the interface ΔT_{int} between the two materials, the resistance, also called the contact thermal resistance, is given as

$$R_c = \frac{1}{h_c} = \frac{\Delta T_{int}}{Q} \tag{4.6}$$

Where the value of R_c is determined experimentally,[62] and is dependent on bonding surface roughness, material properties, temperature and pressure at the interface, and type of fluid trapped at the interface.[70]

4.3.2 Convection: When a fluid flows over a solid body or inside a channel while the temperature of the fluid and the solid surface are different, heat transfer between the fluid and the solid surface takes place as a consequence of the motion of fluid relative to the surface. This mechanism of heat transfer is known as convection. If the fluid motion is artificially induced, say with a pump or a fan that forces the fluid flow over the surface, the heat transfer is said to be forced convection. On the other hand, if buoyancy effects resulting from density difference caused by temperature gradient in the fluid set the fluid in motion, the heat transfer is said to be by natural (or free) convection. From an electronic packaging thermal management perspective, forced air cooling offers the ability to achieve higher heat transfer coefficients than natural convection, and is relatively insensitive to packaging orientation[3] and therefore is used widely. Given an incompressible Newtonian Fluid in rectangular coordinates system, the continuity equation based on the principle of conservation of mass in a two-dimensional domain, and under steady state and constant properties is given by:

$$\frac{\partial u}{\partial x} + \frac{\partial v}{\partial y} = 0 \tag{4.7}$$

Where $u = u(x, y)$ and $v = v(x, y)$ are velocity components of the flow in **x** and **y** directions respectively. Also, the equations of momentum for a differential volume based on Newton's second law of motion may be given as:

$$\rho\left(u\frac{\partial u}{\partial x} + v\frac{\partial v}{\partial y} \right) = F_x - \frac{\partial P}{\partial x} + \mu\left(\frac{\partial^2 u}{\partial x^2} + v\frac{\partial^2 v}{\partial y^2} \right) \qquad (4.8) \quad (\text{x Momentum})$$

$$\rho\left(u\frac{\partial u}{\partial x} + v\frac{\partial v}{\partial y} \right) = F_y - \frac{\partial P}{\partial y} + \mu\left(\frac{\partial^2 u}{\partial x^2} + v\frac{\partial^2 v}{\partial y^2} \right) \qquad (4.9) \quad (\text{y Momentum})$$

Where

    ρ = Fluid density

    μ = Fluid viscosity in the flow field

    P = Fluid pressure

    F_x and F_y = Body forces per unit volume acting in **x** and **y** direction respectively

In equations 4.8 and 4.9, the left-hand side term represents the inertia forces while the first term on the right-hand side is the body force, and the last term in the parenthesis represents the viscous forces acting on the fluid element. Finally, applying energy balance according to the first law of thermodynamics for a differential volume element in the flow field, the equation of energy is given by:

$$\rho c_p \left(u \frac{\partial T}{\partial x} + \upsilon \frac{\partial T}{\partial y} \right) = k \left(\frac{\partial^2 T}{\partial x^2} + \upsilon \frac{\partial^2 T}{\partial y^2} \right) + \mu \Phi \qquad (4.10)$$

Where the viscous-energy-dissipation function Φ is defined as:

$$\Phi = 2 \left[\left(\frac{\partial u}{\partial x} \right)^2 + \left(\frac{\partial \upsilon}{\partial y} \right)^2 \right] + \left(\frac{\partial \upsilon}{\partial x} + \frac{\partial u}{\partial y} \right)^2 \qquad (4.11)$$

All the terms in equation 4.10 and 4.11 have been previously defined. Therefore, for a given element in electronic package, surrounded by ambient temperature **T**, the one-dimensional thermal network approximation based on Newton's law of cooling may be given as

$$Q_e = h_e A_e (T_s - T_\infty) \qquad (4.12)$$

Solving for the temperature change, equation 4.12can be written as

$$T_s - T_\infty = Q_e \left(\frac{1}{h_e A_e} \right) = Q_e R_e \qquad (4.13)$$

These equations will be modified by appropriate boundary conditions for this work.

4.3.3 Thermal Network Nodal Energy Balance: Since the thermal network represents an assembly of nodes that are interconnected by thermal elements, the thermal resistance may be used to determine the rate of transfer of thermal energy between two connecting nodes. [79-83] Lets consider thermal circuit shown in figure 4.1. Under steady state conditions, the principle of conservation of energy can be applied to **node$_i$** as follows:

$$Q_i(input) = Q_i(output) = \sum \left(\frac{T_i - T_j}{R_{ij}} \right)$$
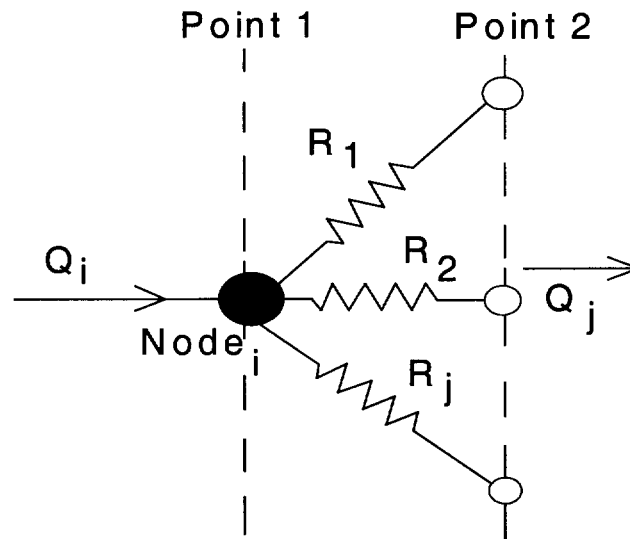
(4.14)

Figure 4.1   Steady State Energy Balance of Thermal Circuit between points 1 and 2.

4.4 **Application to Research Model**: In order to apply the concepts presented in this chapter to analyze the model shown in figure 3.1, some necessary assumptions will be made. It is assumed that, the heat generated in the chip module, which is also referred to as the junction heat, diffuses heat through the chip body in a three directional manner. The three dimensional effects of heat transfer can be approximated by thermal resistance network shown in figure 4.2, which represent all the primary heat flow paths. An additional term known as constriction thermal resistance[62] is introduced to the network to capture the three-dimensional effects and is given by

$$R_{constriction} = \frac{2}{2\sqrt{\pi d k}} \qquad (4.15)$$

Where **d** and **k** denote the diameter of the heat generation element (rod) and thermal conductivity of the larger of the bodies, respectively. The symbol **R_comb**, represents the combined thermal resistance effects due to the chip, the bond wires, and leadframe which may be use in thermal analysis for the model.
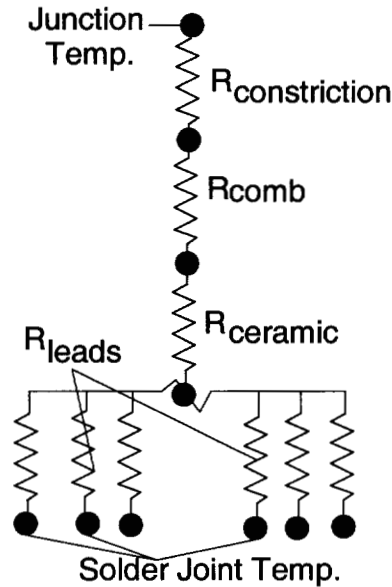

Figure 4.2   Complete Thermal Resistance Network for Research Model.

CHAPTER FIVE

Structural Optimization Methods

5.1   Classical Optimization Theory: An optimization problem in electronic packaging can be expressed as a general nonlinear programming (NLP) problem of the following form[84, 85]

$$
\begin{aligned}
&\textit{Minimize} \qquad\qquad f(x) \\
&\textit{Subjected \quad to} \\
&\qquad\qquad g_i(x) = 0, \qquad i = 1,\ldots p \\
&\qquad\qquad g_i(x) = 0, \qquad i = p+1,\ldots m \\
&\qquad\qquad x_{iL} \le xi \le x_{iU}, \quad i = 1,\ldots n
\end{aligned}
\tag{5.1}
$$

Where $f(x)$ and $g_i(x)$ are objective and constraint functions respectively, x_{iL} and x_{iU} are lower and upper bounds for the variable x_i, and **p**, **m** and **n** are the numbers of equality constraints, total constraints and design variables, respectively. The functions $f(x)$ and $g_i(x)$ are usually assumed to be twice continuously differentiable. Classical optimization theory uses differential calculus to determine points of maxima and minima for both unconstrained and constrained functions.[86-88] In a situation where some of the variables are discrete and others are continuous, we get the so-called mixed-discrete nonlinear programming problem (MDNLP) or mixed continuous-discrete variable problem. This class of optimization problem is not discussed in this section.

5.1.1   Concepts and methods of Optimization: In this section, definitions of various terms and concepts used in classical optimization analysis are presented. Given an objective (cost) function $f(X)$, an extreme point of the function defines either a maximum or a minimum of the function. Mathematically, a point $X_0 = (X_1, \ldots, X_j, \ldots, \ldots, X_n)$ is a maximum if

$$
f(X_o + h) \le f(X_o)
\tag{5.2}
$$

For all $h_0 = (h_1, ..., h_j, ..., ..., h_n)$ such that $|h_j|$ is sufficiently small for all j. This implies that X_0 is a maximum if the value of f at every point in the neighborhood of X_0 does not exceed $f(X_0)$. In a similar manner, X_0 is considered minimum for h if the following condition is satisfy

$$f(X_O + h) \geq f(X_O)$$ (5.3)

It is possible to have multiple extrema for any given range $[0, X_b]$ of a objective function $f(X)$ as shown in figure 5.1. **Points X_1, X_2, X_3, X_4, and X_5, are all extrema of $f(X)$.** Points X_1, X_3, and X_5 are the maxima and X_2 and X_4 are the minima.
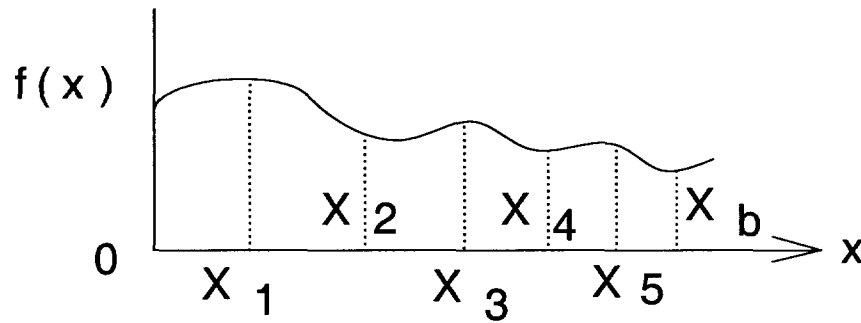
Figure 5.1   Multiple Maxima and Minima for a Objective (Cost) Function.

Local Minimum: The objective function $f(X)$ has a local or relative minimum at a point X_0 in the feasible interval set S if the function value is smallest at X_0 compared to all the other points X within the feasible neighborhood X_0 in equation 5.1. If strict inequality holds, then X_0 is called the strict or isolated local minimum. In reference to figure 5.1, point X_4 is the local minimum.

Global Minimum: The cost function $f(X)$ has a global or absolute minimum at a point X_0 if equation 5.1 holds for all X in the feasible interval set S. Point X_0 is referred to as strict or unique global minimum if strict inequality holds. In reference to figure 5.1, point X_b is

the global or absolute minimum for the objective function for the given interval. These definitions show that for the local minimum, we only test the inequality in equation 5.4 for a small feasible region around the point X_0, whereas we test it over the entire feasible interval set S for the global minimum point. In situations where there are no constraints imposed on the system, the feasible set for the problem is the entire design space.

5.1.2 Optimality Criterion: In general, we do not know before attempting to solve a problem if a minimum point exists for a given objective function. In certain cases we can ensure existence of a minimum point for an objective function if the Weirstrass Theorem of the existence of global minimum is satisfied [88]. The theorem states that, if $f(X)$ is continuous on a non-empty feasible set S, which is closed and bounded, then $f(X)$ has a global minimum in S. A set S is closed if it includes all its boundary points and every sequence of points, subsequently converges to a point in a set. A set is said to be bounded if for any point $X \in S$, $X^T X < C$, where C is a finite number. When conditions of the Weierstrass theorem are satisfied, the existence of global optimum is guaranteed. Even when the conditions of theorem are not satisfied, a global solution may still exist, but its existence cannot be guaranteed.

Unconstrained Problem Necessary Conditions: To minimize an objective function $f(X)$ without any constraints, the following conditions must be satisfied at the minimum point X_0:

Condition 1 ~ _Necessary Condition (First Order)_: If X_0 is a local minimum for the objective function f (X), then its first derivatives at X_0 must vanish, i.e.:

$$\frac{\partial f}{\partial X_i} = 0 \qquad i = 1, 2, \ldots n \tag{5.4}$$

Condition 2 ~ _Necessary Condition (Second Order)_: If X_0 is a local minimum for the function $f(X)$, then its Hessian

$$H = \frac{\partial^2 f}{\partial X_i \partial X_j}$$
(5.5)

at X_0 must be at least positive semi-definite. That is, all its eigenvalues must be non-negative.

Condition 3: ~ _Sufficient Condition (Second Order)_: If the Hessian matrix $H(X_0)$ is positive definite at the stationary point X_0, then X_0 is an isolated local minimum point. The associated matrix is called positive definite if all its eigenvalues are positive.

Since the above three conditions have to do with derivatives of $f(X)$ at point X_0, the minimum point is not changed if a constant is added to the cost function, or if it is scaled by a positive scalar, though the optimum value of the objective function is changed. A stationary point is the one that satisfies all the necessary conditions stated above. If a stationary point is neither a minimum nor a maximum, then it is called an inflection point.

5.1.3 The Theory of Constrained Optimization: The conditions for constrained optimization problem presented in this section are known as Karush-Kuhn-Tucker (KKT) conditions.[89] Consider the constrained optimization problem of minimizing $f(X)$ subject to the constraints $g_i(X) = 0$, $i = 1$ to p. A point X_0 satisfying the constraints $g(X_0) = 0$ is said to be a regular point of the design space if gradient vectors of all constraints at the point X_0 are linearly independent. That is, no two gradients can be expressed as a linear combination of the others. The KKT conditions assume that the minimum point is a regular point of the feasible set S.

Karush–Kuhn–Tucker Necessary Conditions: Let the Lagrangian for the constrained optimization problem of minimizing **f(X)** subjected to the constraints **g$_i$(X)** be defined as

$$L(X,u) = f(X) + \sum_{j=1}^{m} u_j g_j \qquad (5.6)$$

Where **u$_j$** is the Lagrange multiplier for the constraint **g$_j$** that needs to be determined. If we let **X$_0$** be a regular point in the feasible set *S* for **f(X)**, then there exist unique Lagrange multipliers **(u$_j$)$_0$** such that

$$\frac{\partial L(X_0)}{\partial X_i} = \frac{\partial f(X_0)}{\partial X_i} + \sum_{j=1}^{m} \left(u_j\right)_0 \frac{\partial g_i(X_0)}{\partial X_i} \qquad i = 1,2,\cdots n \qquad (5.7)$$

$$g_j(X_0) = 0 \qquad\qquad j = 1,2, \quad to \quad p \qquad\qquad (a)$$

$$\left(u_j\right)_0 g_j(X_0) = 0 \qquad\qquad j = (p+1) \quad to \quad m \qquad\qquad (b)$$

$$g_j(X_0) \le 0 \qquad\qquad j = (p+1) \quad to \quad m \qquad\qquad (c)$$

$$\left(u_j\right)_0 \ge 0 \qquad\qquad j = (p+1) \quad to \quad m \qquad\qquad (d)$$

$$(5.8)$$

Where there are **(n + m)** unknowns. The **n**, and **m** are the design variables and Lagrange multipliers respectively. The necessary conditions give enough equations **(n + m)** for the solution of all the unknowns, though they are usually nonlinear.

The sufficiency of KKT necessary conditions are also sufficient if the objective function and solution space satisfy additional conditions regarding convexity and concavity. These are summarized in table 5.1. If a given constrained optimization problem is subjected to constraints is convex, then any local minimum is also a global minimum and the KKT First-Order conditions are necessary as well as sufficient.

Table 5.1 Convexity and Concavity Conditions

TYPE OF OPTIMIZATION	REQUIRED CONDITIONS	REQUIRED CONDITIONS
	OBJECTIVE FUNCTION	SOLUTION SPACE
Maximization	Concave	Convex Set
Minimization	Convex	Convex Set

A function of n variables is convex if its Hessian is at least positive semi-definite everywhere. That is, when we differentiate each component of the gradient vector equation 5.4, with respect to X_1, X_2, X_3, ... X_n, to form matrix equation 5.5, and then evaluating each element of the matrix at the optimum point Xo, so that at least one element of the Hessian matrix is positive semi-definite.

5.2   Stochastic Optimization Methods: These algorithms employ a concept in stochastic computational techniques, derived from statistical mechanics for finding near globally minimum-cost solutions to large optimization problems.[9] These methods use algorithms known as "Stochastic Search" that generate random numbers as they search for the optimum solution. They do not require the evaluation of gradients of both objective and constraint functions as required for gradient-based classical optimization methods. Stochastic optimization methods are used to find global minima or maxima to problems involving discrete variables, difficult problems that are large, noisy, fraught with local minima, or discontinuous. Two random search algorithms namely, Genetic Algorithms (GA) and Simulated Annealing (SA) [9, 90, 91] are presented in this section. The section also concludes with a Neural Network overview and its application to electronic packaging.

5.2.1   Genetic Algorithm: This method imitates the process of evolution of biological species wherein fitness is maximized. The method works by maintaining a pool termed *population of several designs which are randomly combined to find improved solutions to any given problem*.[90]   A string of binary coding that encodes the design variables, represent each population member. In a genetic algorithm, one starts with a set of designs from which new and better designs are generated using the fittest members of the population pool or set.   The three operators required to implement the algorithm are described below:

Reproduction: Is an operator where an old string is copied into the new population according to the string's fitness which is defined according to the cost function value. The higher the value of the cost function, the lesser the number of offsprings of the fit strings it receives.

Crossover: This operator permits the selected population members to exchange the characteristics of the design among themselves. It involves the selection of starting

and ending positions on a pair of mating strings at random, by simply exchanging the strings of **0**'s and **1**'s (for a binary string) between these positions on one string, with that of the mating string.

Mutation: This is the final operator that safeguards the process from a complete pre-mature loss of valuable genetic material during reproduction and crossover. In terms of binary strings, this step corresponds to selecting a few members of the population, determined at random, a location on the string, and switching the **0** or **1** at that location.

The format of genetic algorithm involves eight procedural steps highlighted below, based on Huang's [92] work:

Step 1 ~ Define a scheme which represents a design point by a genetic string

Step 2 ~ Randomly generates **Np** genetic strings (member of the population) according to the schema, where **Np** is the population size. For constrained problems, only the feasible strings are accepted. Set $K = 0$.

Step 3 ~ Define the fitness function. A design with lower objective will have larger fitness value.

Step 4 ~ Assign fitness values to all members.

Step 5 ~ Reproduction: According to fitness values, select members from the current population and create a new population.

Step 6 ~ Crossover: Select two members from the new population, randomly choose two sites on their genetic strings and swap strings between two chosen sites among them.

Step 7 ~ Mutation: Choose a few members from the new population and modify each of them at a randomly selected site.

Step 8 ~ If any of the convergence is satisfied, stop, otherwise return to step 4.

For the purpose of GA, convergence in step 8 is satisfied if the following conditions are met. 1) The number of the generation K reaches a pre-set number. 2) The number of the strings having the highest fitness become large and 3) the best value of the fitness is not updated for many generations.

5.2.2 Simulated Annealing: This optimization method is based on thermodynamical analogy of the annealing of metals. When a molten metal is allowed to solidify by cooling slowly (annealing), it eventually arrives at a low energy state. Quenching on the other hand, is a sudden process of cooling metals, and it somehow assumes a higher energy state. The Simulated Annealing method attempts to minimize some analogue of the energy (temperature, T) in a manner similar to the metal annealing process, in order to achieve the global minimal of the cost, objective, or energy function. [90, 91] Applying the terminology of stochastic processes, each configuration of particles is referred to as a state. At each temperature, the solid is allowed to reach thermal equilibrium where the probability of being in a state **i** with the energy E_i is given by either Gibbs or Boltzmann probability density function (pdf) as

$$P(E_i) = \frac{e^{\left(-\frac{E_i}{KT}\right)}}{\sum\limits_{j \in S} e^{\left(-\frac{E_j}{KT}\right)}} = \frac{1}{Z(T)} e^{\left(-\frac{E_i}{KT}\right)}$$

(5.9)

where the set **S** consist of all possible configurations, **K** is Boltzmann's constant, and **T** is the temperature that controls the annealing process. The function Z(T), represents the partition function and is given by:

$$Z(T) = \sum_{j \in S} e^{\left(-\frac{E_j}{KT}\right)} \tag{5.10}$$

The significance of the control parameter **T**, in Simulated Annealing Optimization Processes, lies in the fact that it is used indirectly to determine how much of an increase in the objective (cost) function should be accepted when the process moves from one state to another. If we let m_i denote the current (the starting) state of the process, with its energy being $E(m_i)$, a small perturbation to m_i is made to obtain a new model state m_j given as

$$m_j = m_i + y_i(m_i) \tag{5.11}$$

where y_i is a random variable that falls between **–1** and **1**. To illustrate the importance of temperature T, in simulated annealing algorithm, the following probability density function given as

$$M = g_i(y_i, T_i) = \frac{1}{2(|y_i| + T_i)\ln\left(1 + \frac{1}{T_i}\right)} \tag{5.12}$$

will be used to generate a contour plot of the function M against y and T, as shown in figure 5.2. From this figure, it can be seen that, as the parameter temperature is reduced, the likelihood of simulated annealing finding a new state in the neighborhood closer to the current state increases significantly. Two noteworthy behavior of the Gibbs distribution can be seen in; a) at low energy state, the probability of occurance is higher than the higher energy state, and b) the low energy ordered states are strongly favored at low temperature.
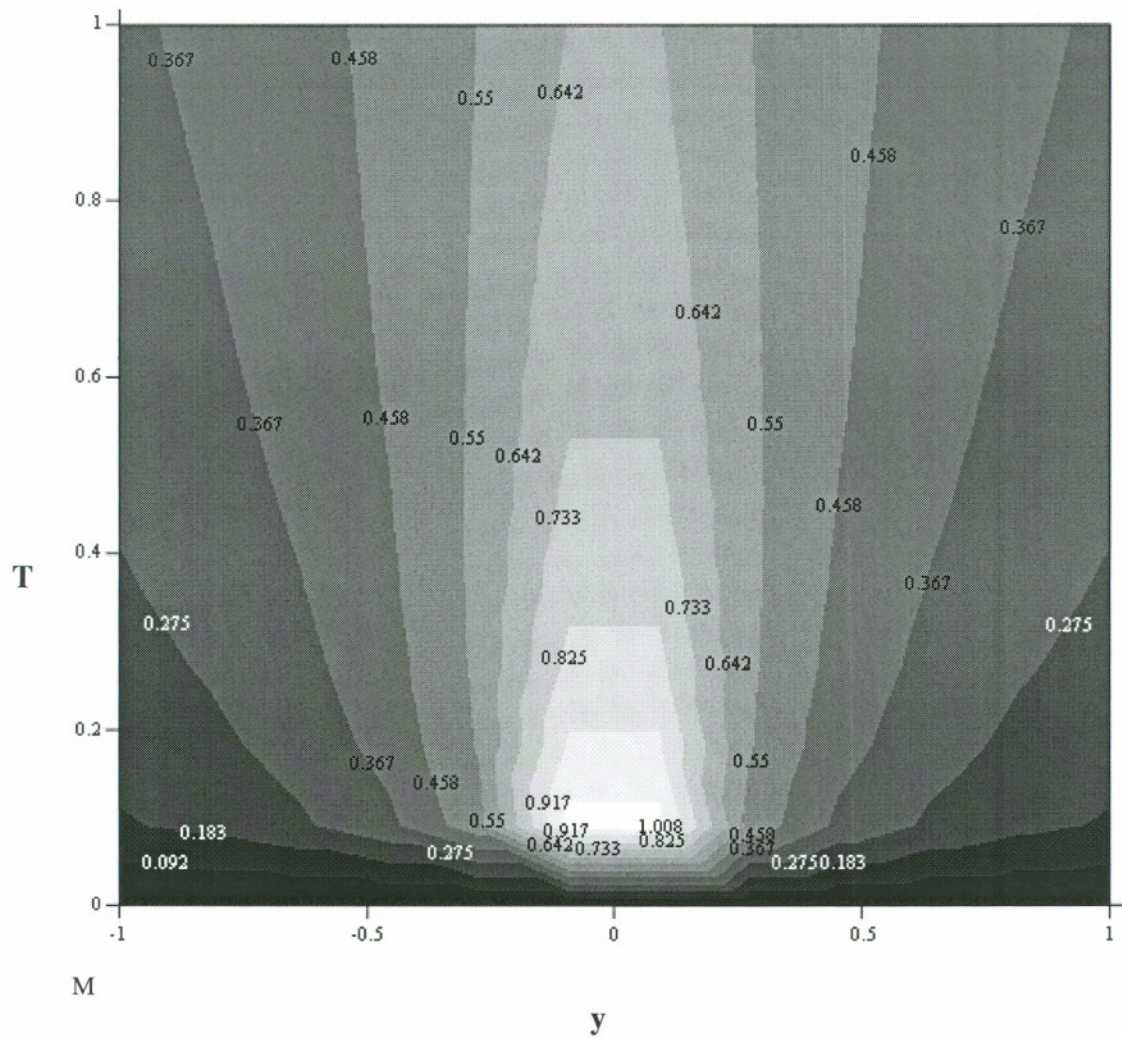
Figure 5.2 Contour Plot of the function **M** showing the Likelihood of Simulated Annealing Method finding the New State (maximum point) in the limit as $T \rightarrow 0$.

For this work, the energy function is identified with the error function **E(m)**. The error is due to possible imperfection in the computational models, and it takes on different values for different model configurations. Given an optimization problem, the objective therefore, is to find the state or model **m** for which the error is minimum. For instance, if

ΔE_{ij} is the difference (error) in the energy between the starting state m_i and the new state m_j, which is expressed mathematically as

$$\Delta E_{ij} = E(m_j) - E(m_i) \tag{5.13}$$

The decision whether or not the new state is accepted is based on the following rule:

if $\Delta E_{ij} \leq 0$, then the new state is unconditionally accepted. However, if $\Delta E_{ij} \geq 0$, then the new state is accepted if it meets the probability condition

$$P = e^{\left(-\frac{E_{ij}}{T}\right)} > r \tag{5.14}$$

where r is a randomly generated number that lies between 0 and 1. Equation 5.14 is referred to as the Metropolis Acceptance Criterion. Metropolis et al,[93] introduced simulated annealing optimization algorithm that uses this criterion. Kirkpatrick et al[94] extended the application of the algorithm to solve other types of optimization problems. The primary steps involved in running the algorithm are as follows

Step 1 ~ Obtain a starting temperature T, and state m_0, and evaluate $E(m_0)$

Step 2 ~ Randomly generate a new state close to m_0 and calculate $E(m_1)$

Step 3 ~ Analyze the new candidate state for $\Delta E = E(m_1) - E(m_0)$. If the candidate is feasible, that is $\Delta E \leq 0$, then $m_0 = m_1$ and $E(m_0) = E(m_1)$

Step 4 ~ If the candidate is $\Delta E \geq 0$, then generate a random number r such that, $0 < r < 1$. If $r < P$, let $m_0 = m_1$ and $E(m_0) = E(m_1)$.

Where $$P = e^{\left(-\frac{\Delta E}{T}\right)}$$

Step 5 ~ Stop the process if m_0 has not changed for several iterations; otherwise update $T = \alpha T$, where α is a number less than one, and return to step 2.

This algorithm is programmed in the computational program Mathcad developed by Mathsoft[95] and was used for this project depending upon the nature of the objective and constraint functions developed in chapter 6.

5.2.3   Neural Networks: A neural network is a massively parallel distribution processor (interconnections) made up of simple processing units, which has a natural propensity for storing experimental knowledge and making it available for use.[96] It resembles the brain in two respects:

1. The network acquires the knowledge of its environment through a learning process, and the procedure used to perform the learning process is called a learning algorithm.

2. The knowledge gained in the process of learning is stored in the network inter-neuron connections, known as the modifying synaptic weights of the network.

The network is able to attain the desired objective by modifying the synaptic weights of the network in an systematic fashion. Figure 5.3 illustrates a typical neural network structure showing the input layer, the hidden layer, and an output layer.
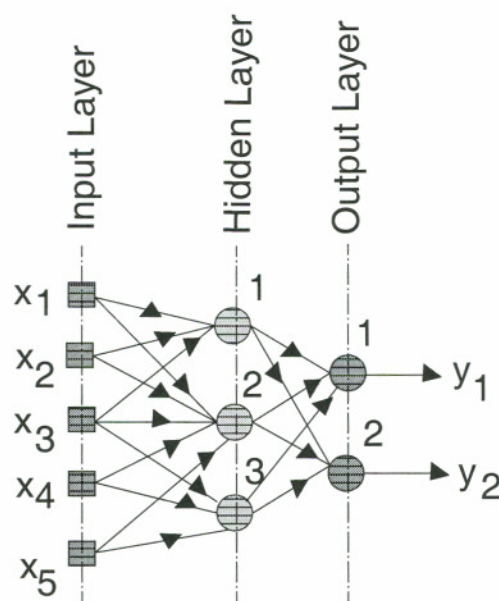

Figure 5.3   Partially Connected Feed-forward Back Propagation Neural Network.

The top three source nodes constitute the receptive field for hidden neuron **1**. Similar connections exist for the other hidden neurons in the network. To satisfy the weight-sharing constraints for each of the neurons in the hidden layer of the network, the same set of synaptic weights are used. This weight-sharing constraint concept may be applied to figure 5.3, where three local connections are connected to one neuron to make a total of three neurons. We may express the induced local field of hidden neuron **j** as follows

$$u_j = \sum_{j=1}^{3} w_i X_k \qquad j = 1, \quad 2, \quad 3 \tag{5.13}$$

where $\{w_i\}_{i=1}^{6}$ constitute the same set of weights shared by all four hidden neurons, and X_k is the signal picked up from the source node **k = i + j − 1**.

Neuron Models: The basic element (neurons) of neural was reported in the early 1940's. Neural network applications have attracted the attention of researchers from a number of disciplines over the last three decades.[97] The rapid recognition of the method is based on the fact that the method can potentially enable one to find solutions to objective functions, after sucessful training. In this study, we will introduce one of the main models. Consider the basic neuron model shown in fig 5.4, consisting of a processing element with synaptic input connections and a single output.
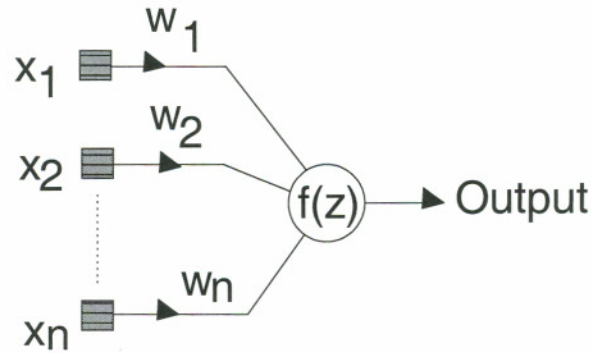
Figure 5.4   Simple Neuron Model.

In this simple model, inputs are multiplied by their respective connection weights w_i, which will yield the effective input to the processing element as

$$Z = \sum_{i=1}^{n} w_i X_i \qquad (5.16)$$

This weight input is then passed to an activation function called the sigmoid function which is expressed as

$$f(Z) = \frac{1}{1 + e^{-(Z+T)}} \qquad (5.17)$$

where Z is the weighted input processing element and T is the bias parameter used to modulate the output element. The proper weight coefficients, w_i and the bias parameter, T are determined in the network training process.

Feed-forward Neural Networks: There are two classes of neural networks, namely, feed-forward and feed-back networks. If the neurons' outputs are not connected to their inputs, the network is referred to as feed-forward networks. On the other hand, when the neurons' output are connected back to input, the resulting network is called feedback or recurrent network. Only feed-forward approach is present in this section. A single layer feed forward network with **n** input space **x** to output space **0** shown in figure 5.4 can be expressed as follows

$$
0 = \Gamma[w_x] \equiv
\begin{bmatrix}
f(.) & 0 & . & . & 0 \\
0 & f(.) & . & . & 0 \\
. & . & f(.) & . & . \\
. & . & . & . & . \\
0 & 0 & . & . & f(.)
\end{bmatrix}
\begin{bmatrix}
w_{11} & w_{12} & . & . & w_{1n} \\
w_{21} & w_{22} & . & . & w_{2n} \\
. & . & . & . & . \\
. & . & . & . & . \\
w_{m1} & w_{m2} & . & . & w_{mn}
\end{bmatrix}
\tag{5.18}
$$

Where w_x is the weight or connection matrix. The elements in the matrix operator Γ are given by the activation functions defined by equations 5.17 and 5.18. This type of network is called a linear network, although the operator function $f(Z)$, used to process the elements at every computing node is nonlinear. A linear network with two or more hidden layers is referred to as multilayer network. These types of networks are sometimes called layered or hidden-layer networks. The first layer, consisting of **n** input nodes, is called input layer while the last is referred to as the output layer. The layers bounded by the input and output layers are called hidden layers since they do not interact with the external environment. They simply accept and output information. The number of hidden layers and their nodes are problem dependent and should be minimized for computational efficiency since additional internal mapping is required. Multilayer network is capable of learning the mapping of complex functions through the proper choice of the number of hidden layers and their nodes.

Network Training: Neural network requires training before it can be used to optimize a objective function. The supervised learning algorithm adopted for this work is called the error back propagation training algorithm. Weights are systematically modified so that the response of the network increasingly approximates the desired response. Such process may be interpreted as optimization of the objective function. The design variables of the optimization are the synaptic strengths (weights) and biases within each node, as well as the objective function. The output error function is defined by

$$F = \sum_n \left[\sum_k \|d_{kn} - Output_{kn}\|^2 \right] \qquad n = 1, N; \qquad k = 1, K \qquad (5.19)$$

Where **N** is the number of training trials, and **K** is the number of output nodes. The learning algorithm modifies the weights so that the error decreases during the learning process. Once the network is trained so that **error_trained** ≤ **error_max**, it can be used as a function approximator for both continuous and discrete optimization problems.

Inter-neuron connection strengths, also known as synaptic weights are used to store the acquired knowledge. The procedure used to perform the learning process is called a learning algorithm, and the synaptic weights of the network are modified in an orderly fashion to attain a desired objective. Figure 5.3 illustrates a typical neural network structure with both the input and the output layers and a single hidden layer.

The concepts presented above are applied to solder joint constitutive data contained in table 5.2, in order to find the design values that will produce the optimum solder joint given the inherent uncertainties that may be present in the data.[16] To minimize the level of uncertainty in the data (sections 2.1.2 and 2.1.3), neural network method was used to learn the mapping of the input variables (stresses) to the continuous output variable (strain).

Table 5.2   Digitized Eutectic 63Sn-37Pb Solder Data at 25°C Ref. Temperature.[16]

STRAIN	STRESS-A	STRESS-B	STRESS-C	STRESS-D	STRESS-E	STRESS-F	STRESS-G	STRESS-H
0.000	0.00	0.00	0.00	0.00	0.00	0.00	0.00	0.00
0.005	10.00	10.00	10.00	10.00	10.00	10.00	10.00	10.00
0.010	20.00	20.00	20.00	20.00	20.00	16.80	16.80	16.80
0.015	30.00	30.00	30.00	30.00	30.00	24.00	24.00	24.00
0.020	36.00	36.00	36.00	36.00	36.00	27.30	27.30	27.30
0.040	41.20	40.00	41.20	40.00	40.00	31.00	31.00	31.80
0.060	43.80	41.20	43.80	42.20	41.20	32.20	32.20	33.50
0.080	44.60	42.20	45.00	43.00	42.50	32.80	33.20	34.20
0.100	46.60	43.00	46.00	44.00	43.00	33.00	33.80	34.60
0.200	49.50	45.80	49.00	47.00	45.80	33.00	34.20	33.60
0.300	49.80	46.80	49.80	48.00	46.80	32.40	32.40	30.40
0.400	48.80	46.70	48.80	48.80	46.70	30.80	30.00	26.00
0.500	47.60	45.00	46.20	47.60	46.20	27.80	26.40	21.80
0.600	46.20	42.80	43.00	45.20	43.00	24.00	22.80	17.80
0.700	45.00	41.80	40.00	42.80	40.00	20.40	19.20	14.00

Note: Solder joint sample thickness = 0.25 mm[16]

Values for Stress-A to Stress-E were obtained from high strain rate (0.09 to 0.21 s^{-1})

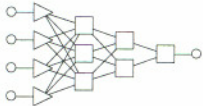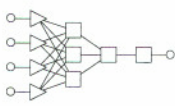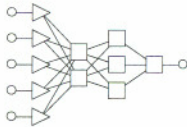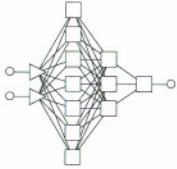Values for Stress-F to Stress-H were obtained from low strain rate (0.002 to 0.003 s^{-1})
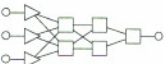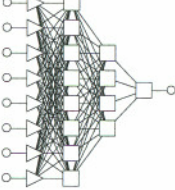
In standard linear regression analysis, the coefficient of the analysis which is referred to as R^2 which is based on the method of least squares proximity to unity is use to judge how well the proposed model correlates with a test data. In neural network, a network is judge successful if it makes predictions more accurate than a simple or standard regression methods estimate. To achieve this, the data set is divided into three data subsets. One of the subsets, termed the training set is used to produce an estimate that has a *lower prediction error standard deviation* than the training data standard deviation itself. The other two subsets are used for training and verification computation respectively.
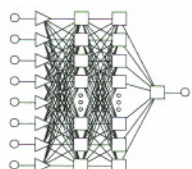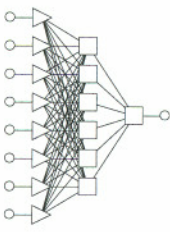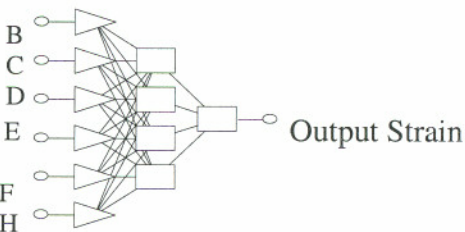
The networks automatically calculate the mean and standard deviation of the training and the verification subsets during its computation. It also calculates the mean and the standard deviations of the prediction errors. If the ratio of the prediction to data standard deviations is unity, then the network does no better than a simple average. This implies that, a good network should always have a ratio lower than one. For performance comparison with the standard regression analysis methods, neural network also computed standard least square fitting parameters, i.e. Pearson-R correlation coefficient between the actual and predicted outputs. A perfect prediction will have a correlation coefficient of unity.[98] The generalized regression neural network (GRNN) and probabilistic neural network (PNN) were used for this study with the results given in tables 5.3 and 5.4.

Table 5.3   Eutectic (63Sn-37Pb) Solder Alloy Network Regression Statistics.

	TRAINING STRAIN	VERIFICATION STRAIN	TESTING STRAIN
Data Mean	0.219375	0.0425	0.3683333
Data Standard Deviation	0.2279166	0.04646	0.3485805
Error Mean (E)	0.0003258	-0.0007377	-0.01799
Error Standard Deviation	0.0161	0.00589	0.038
Absolute E	0.01271	0.004747	0.0306
Standard Deviation Ratio	0.07066	0.1267801	0.109005
Correlation	0.9976339	0.9922279	0.9949118

Table 5.4   Array of Ten Good Networks for Eutectic Solder Alloy.

1st Network	2nd Network	3rd Network
4th Network	5th Network	6th Network
7th Network	8th Network	9th Network

Notes
The tenth network performed much better than the first nine shown above.

(see table 5.1 and 5.2 input and   output data respectively)

10th Network

Input Stresses

B
C
D
E
F
H

Output Strain

CHAPTER SIX

APPLICATION TO 20-PIN CERAMIC QUARD FLATPACK SOLDER JOINT

6.1   Problem Description: A 9mm x 9mm x 1.5 mm thick 20-pin surface mount Ceramic Quard FlatPack (CQFP) electronic component shown in figure 3.4, consist of ceramic chip body which is supported by copper leadframe and is joined to the PCB with near-eutectic 63Sn-37PB solder alloy via the copper pad and firmly bonded to PCB. Each side of the chip has five pins of cross-sectional area of 0.254mm^2, and a stem height of 1.4mm.   Torsional eccentricity due to the chip center of mass and center of rigidity not coinciding may induce significant torsional forces at the solder joint [99] when the system is excited by random vibration, but will not be considered in this study.

The objective of the study, as stated earlier, is to investigate the relationship between solder joint formation during manufacturing stages (molten state) and the integrity of the solder joint geometry (solidified state), and under the action of thermomechanical loads. In carring out this study, careful attention was paid to the three molten solder properties when subjected to thermomechanical loads. These properties are as follows:

1. Surface tension at the solder-atmosphere interface
2. Gravitational force on the solder, and
3. Wetting angles

The thermomechanical forces acting on the copper gullwing leadframe solder joints were computed from the global finite element model shown in figure 3.4. A structural optimization method was employed to predict the optimum solder fillet based on the proposed bond force equation. A second finite element analysis was performed on the predicted optimum solder joint using material nonlinearity. This option was done to verify that the actual stresses in the optimum joint are within solder alloy allowable limits.

In summary, the elements for the work in this chapter follows the flowchart shown in figure 6.0.
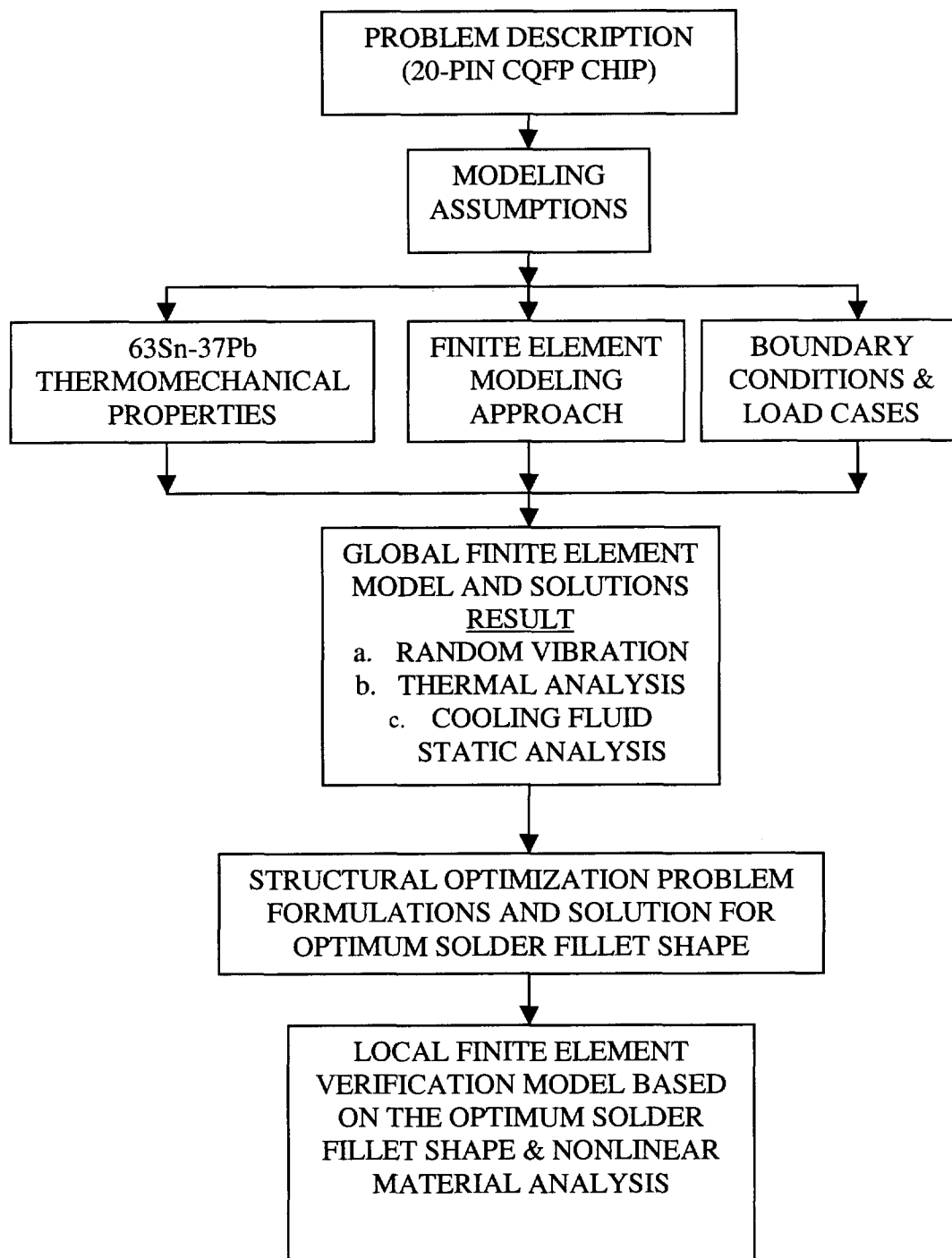
```
┌─────────────────────────────────┐
│     PROBLEM DESCRIPTION          │
│      (20-PIN CQFP CHIP)          │
└─────────────────────────────────┘
                │
                ▼
┌─────────────────────────────────┐
│          MODELING                │
│         ASSUMPTIONS              │
└─────────────────────────────────┘
```

| 63Sn-37Pb THERMOMECHANICAL PROPERTIES | FINITE ELEMENT MODELING APPROACH | BOUNDARY CONDITIONS & LOAD CASES |

```
┌─────────────────────────────────┐
│   GLOBAL FINITE ELEMENT          │
│   MODEL AND SOLUTIONS            │
│          RESULT                  │
│   a.  RANDOM VIBRATION           │
│   b.  THERMAL ANALYSIS           │
│      c.  COOLING FLUID           │
│          STATIC ANALYSIS         │
└─────────────────────────────────┘
                │
                ▼
┌─────────────────────────────────┐
│  STRUCTURAL OPTIMIZATION PROBLEM │
│  FORMULATIONS AND SOLUTION FOR   │
│  OPTIMUM SOLDER FILLET SHAPE     │
└─────────────────────────────────┘
                │
                ▼
┌─────────────────────────────────┐
│     LOCAL FINITE ELEMENT         │
│  VERIFICATION MODEL BASED        │
│  ON THE OPTIMUM SOLDER           │
│  FILLET SHAPE & NONLINEAR        │
│     MATERIAL ANALYSIS            │
└─────────────────────────────────┘
```

Figure 6.0   Flowchart of Computation Details.

6.2 **Modeling Assumptions**: In order to create a computational model that will represent a true CQFP chip module, the following assumptions, outlined below, were deemed necessary in order to obtain accurate system response and minimal FEA computational, data processing and interpretation time. The assumptions were:

1. It was assumed that, a 3-dimensional finite element global model would be adequate to predict the system vibration modes, frequencies, and dynamic responses in terms of maximum displacements and stresses, at the leadframe-solder pad interface. This model was referred to as the global finite element model and it was used to compute the stresses caused by the process of thermal cycle and cooling air loads on the solder joint. This phase of the analysis (global finite element problem) was conducted in the linear elastic regime.

2. The results obtained from the global problem were valid and applicable for structural optimization analysis as well as the detail (local) finite element model of the single solder joint under the action of thermomechanical loads. The 63Sn-37Pb solder alloy was considered as time-dependent material with nonlinear characteristics.

3. A damping ratio of 5 percent of the critical damping was applied to the system, to reflect the discontinuity that may be present in the joint, PCB, and the case.

6.3.1 Thermomechanical Material Properties: Solder joint under thermomechanical loads can deform both elastically and inelastically. Therefore, for any given displacement response, the stress in the solder joint will be a function of the joint assembly compliance, and the inelastic deformation properties of the solder alloy, used for the joint. The creep related material deformation was presented in chapter 2, sections 2.12 to 2.1.3 and therefore only the elastic material properties are covered in this section. The linear elastic material properties used for the global finite element problem are given in Table 6.1. It was assumed that, due to relatively small temperature change of 30 °C, the elastic properties of 67Sn-37Pb eutectic solder alloy will sufficiently predict the stress distribution in the chip caused by the thermomechanical loads without any significant error.

Table 6.1   Thermomechanical Elastic Properties for the Global Finite Element Modal.

Material	Temperature (°C)	Young's Modulus (GPa)	Poisson Ratio	Coefficient of Thermal (mm/mm- °C)	Thermal Conductivity (W/m- °K)
CQFP Chip		303.37	0.21	5.83E-6	120
FR-4 PCB		13.79	0.12	17.6E-6	0.2
Solder (63Sn-37Pb)	24	48.2	0.4	24.7E-6	296
Solder Pad	24	48.2	0.4	24.7E-6	296
Copper Leadframe		130	0.35	16.7E-6	386

6.3.2 General Finite Element Modeling Approach: In order to accurately predict the global response of the problem shown in figure 3.4, the individual components consisting of PCB, solder pad, and leadframe are modeled separately for stiffness and mass properties verification and then assembled together to form the global finite element model.[100-104] The global model comprised of 3810 (3-nodes triangular thin plate elements), 285 (4-nodes quadrilateral thin plate elements), and 643 (8-nodes solid or cubic elements), making a total of 4767 elements and 3815 connecting nodes. All the other electronic components

attached to the PCB mass were lumped onto the board at their respective locations as shown on figure 3.4

The vibration frequencies and modes required for random vibration analysis were computed on the basis of this model. The system mass participating in each mode was evaluated before proceeding to the computation of dynamic stresses. In a similar fashion, the stresses resulting from steady state, linear thermal analysis and cooling fluid drag forces were computed, and combined with the vibration forces using the square root of the sum of squares (SRSS) method. This was done to simulate the combined forces that may be acting on the leadframe-solder joint interface, and therefore was used to augment the local finite element model.

6.3.3 Boundary Conditions and Load Cases: PCB's in electronic packages are normally supported or attached firmly to the chassis of the unit at one end of the board, see figure 1.1. This type of support condition was adopted for the global model, which implies, the connection is capable of resisting rotation (moment) and translation. Pinned support conditions were used between the PCB and solder pad for the local model. The ratio of out-of-plane stiffness of the PCB to the stiffness of one leadframe pin is very large, and therefore will not transmit rotational forces (moments) from the pin to the PCB, hence the pinned support. Similar boundary conditions were used for the cooling fluid model. For the thermal analysis, convection boundary condition in a form of prescribed temperatures was specified for both the chip body and the leadframes, which support the chip. A 3-dimensional conduction steady state thermal analysis was performed using Topaz commercial finite element heat transfer analysis program.

In summary the three load cases imposed on the global model are given below:

1. The dynamic load acting on the model was due to a random vibration with PSD input of 0.20 G^2/Hz as given in a paper by Steinberg,[55] which induced an excitation of the form shown in figures 3.12 and 6.1 on the electronic packaged support. The random

vibration input and response curve is plotted on log-log axises, with the power spectral density expressed in squared acceleration units per hertz (G^2/Hz).

2. Conduction and convection thermal analyses were performed on 3-dimensional CQFP model with 0.6W heat generation rate. The initial temperature used for the analysis was assumed to be 27 °C. The maximum temperature of 57 °C was imposed on the outside surface of the chip which served as the convection boundary condition. Therefore the net temperature change for the analysis was 30 °C.

3. The drag forces acting on the chip body resulting from cooling air with 1.3 m/s air speed as reported in reference [39] was used. Due to the low fluid speed of the cooling air, an equivalent static force to model was used to approximate the fluid dynamics model response.
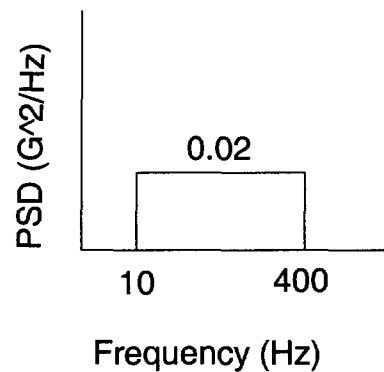
Figure 6.1   Random Vibration PSD Input Response.

6.4   Results – Global FEA Problem: Twenty natural frequencies were computed from the frequency analysis. Only the first ten modes are actually needed for the random vibration analysis since they sufficiently described all the important modes contained in PSD frequency range of 0 to 400Hz. The frequency analysis results are summarized in table 6.2. As expected, the mode shapes (values) confirmed the up and down movement of the chip along the z-axis relative to the PCB. Such response is justified if we compared the in-plane stiffness of the PCB, which is several order of magnitude larger than its out-of-plane component. Secondly, the 20-pin CQFP chip attached to the PCB does not have

enough stiffness by itself, compared to the PCB, to alter the system response and hence moved along with the PCB. Values given in table 6.2 provide an insight into the dynamic behavior of the global model. By examination of the response, possible errors in the FEA model can be detected and corrected before proceeding to the random vibration modal analysis. The effective modal mass along the chip z-axis used for the random vibration analysis equals about 95 percent of the system mass, which exceed the 90 percent industry requirement, see figure 6.2 for mode shape 6 the plot.

Table 6.2   Summary of Frequency Analysis Results.

Mode Number	Frequency (cycles/sec)	Eigenvalues ($\omega 2$)	Periods (sec)	x	Modal Weights y	z
1	11.205	4956.56	0.0892	0.0	0.0	1.4143
2	39.9.	62944.2	.025	0.0	0.00001	0.0369
3	71.467	201640	.014	0.00002	0.0	0.385
4	116.28	533791	.0086	0.0	0.00001	0.0001
5	186.18	1368E6	.0054	0.0	0.00002	0.0007
6	209.55	1.733E6	.0048	0.00002	0.0	0.1435
7	245.21	2.373E6	.0041	0.0	0.0	0.0141
8	322.73	4.11E6	.0031	0.0	0.00002	0.0112
9	383.77	6.36E6	.0025	0.0	0.0	0.0008
10	392.58	6.66E6	.0025	0.0	0.0	0.1088

Stresses were computed directly from the PSD response using the first ten modes of vibration. The displacement and stress contour plots are also given in figures 6.3 to 6.5. These stresses represent one standard deviation (1σ) stresses at the heel of the leadframe hill. It implies that, these stresses will be seen 68.3 % of the time the electronic package is in service. For the case of the cooling fluid load, the stresses resulting from static analysis are given in figures 6.6 and 6.7. Lastly, figures 6.8 to 6.10 shows the heat flux and stresses computed 3-dimensional finite element thermal analysis with the aid of the code Topaz.

The heat flux and stress distribution within the CQFP chip, particularly the copper leadframe, shows a trend that is noteworthy. The leadframe, besides supporting the chip body, can also be seen to provide the pathway for the heat generated by the chip to dissipate to the PCB. In this sense, the PCB can be considered as a heat sink reservoir.

To replicate the true forces the CQFP chip will see during actual service operation, the results of the three separate load cases were superimposed to form one load case for the local problem. This was done by the *square root of the sum of the squares* (SRSS) method. The results given in table 6.3 represent the highest forces present in both xy-plane and xz-plane at the heel of the leadframe-to-solder pad interface. The product of the stress and the area for each respective plane produce the shear and the normal (peeling) forces shown in the table. These forces are considered to be absolute worst-case forces, that the joint will see, since we have assumed previously that all the residual stresses present in the material are negligible. These forces are responsible for undermining the integrity of the joint. The shear force acting at the interface is attempting to break the bond between the leadframe and the solder fillet, while the peeling force at the interface is attempting to break the bond force by pulling the leadframe from the solder pad.

Table 6.3   Summary of Leadframe-Solder Pad Forces due to Global FEA.

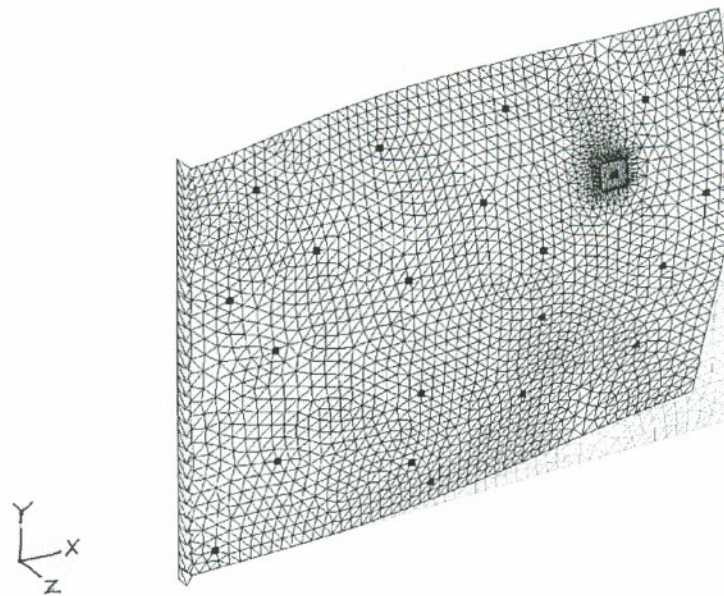| Force Component on the solder joint	Random Vibration Analysis	Cooling Fluid Static Analysis	Thermal Analysis	Combined Force using SRSS Method
Shear Force $_{xy}$	0.737 N	2.25E-6 N	4.56 N	4.62 N
Peeling Forces $_{xz}$	5.78 N	7.756E-7 N	0.35 N	5.79 N

Figure 6.2   Frequency Analysis: Plot of Mode Shape 6.
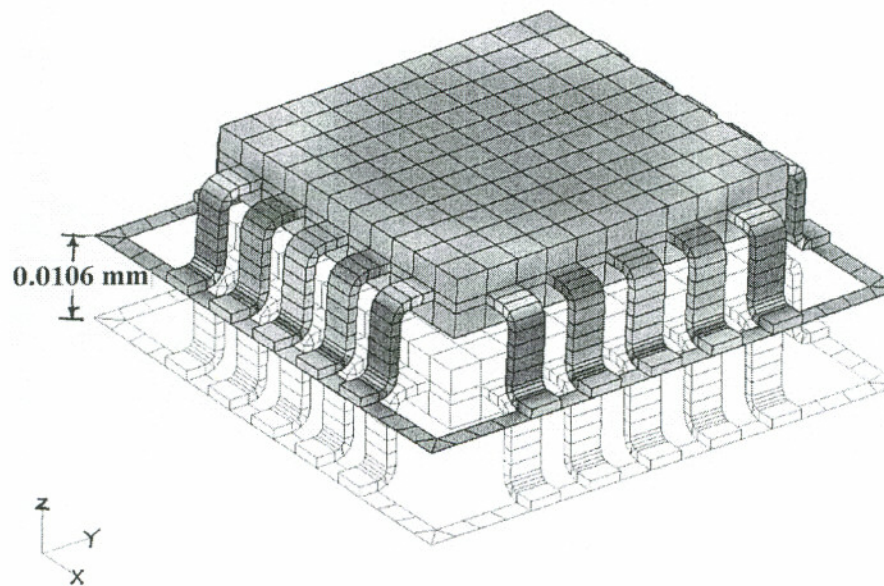
Figure 6.3   PCB-CQFP Chip Out-of-plane Displacement due Random Vibration.

$\sigma_{xy} = 3.52 \text{ N/mm}^2$
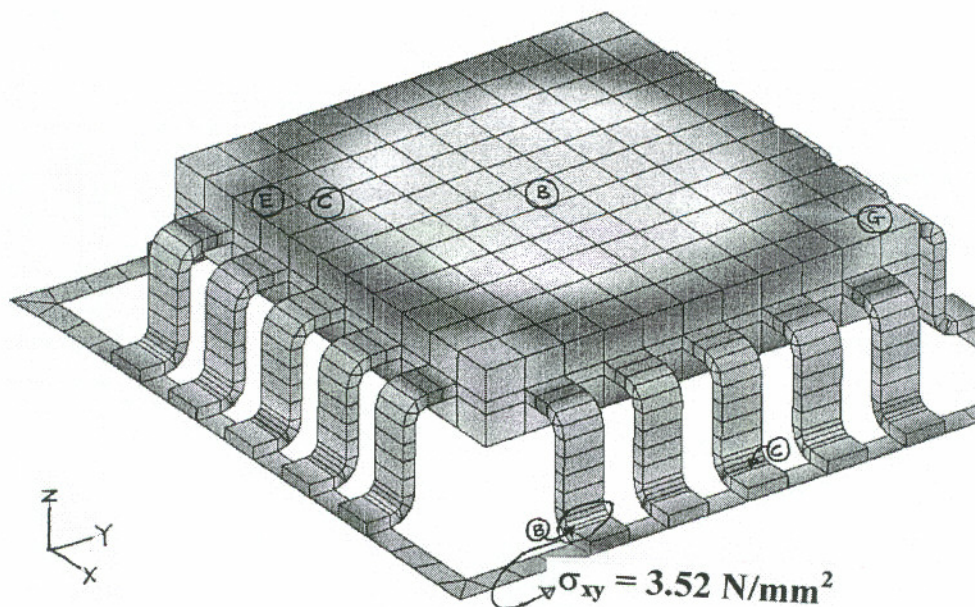
Figure 6.4   Random Vibration: XY-Shear Stress Distribution in CQFP.

$\sigma_{yz} = 27.6 \text{ N/mm}^2$
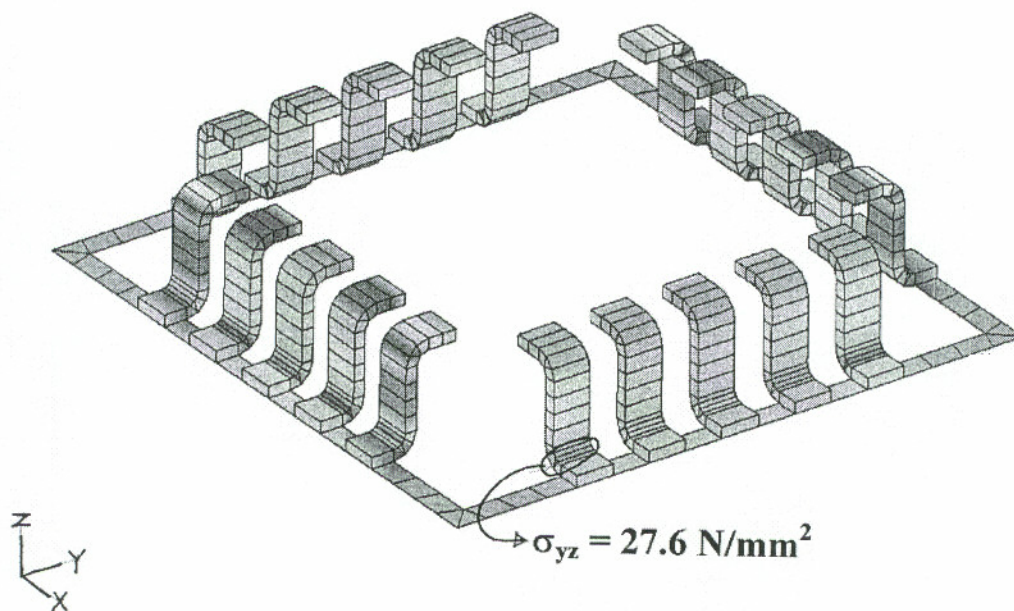
Figure 6.5   Random Vibration: YZ-Shear Stress Distribution in Leadframe.

$$\sigma_{xy} = 2.48\text{E-5 N/mm}^2$$
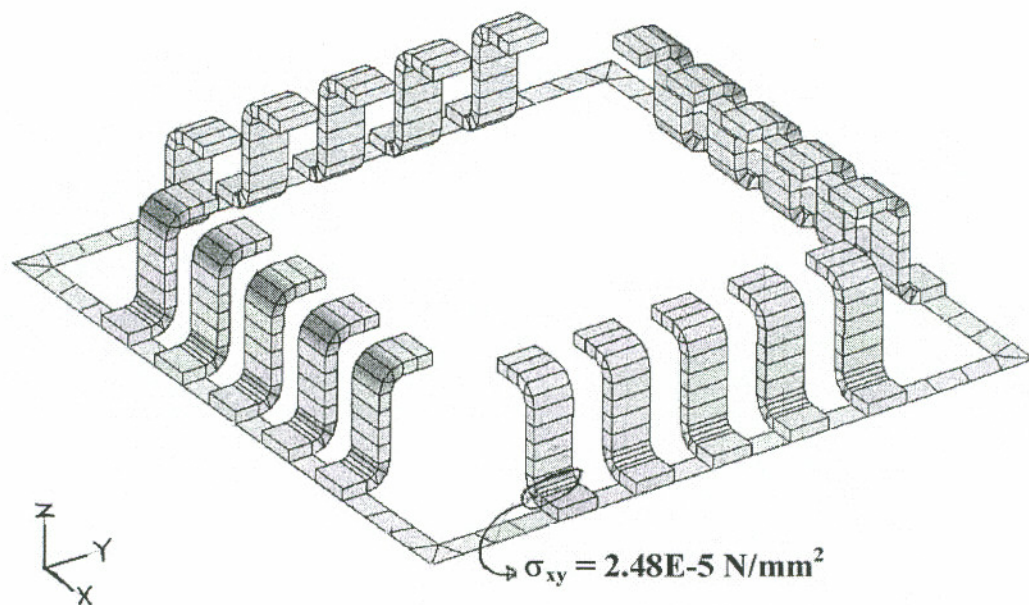
Figure 6.6   Cooling Fluid: YZ-Shear Stress Distribution in Leadframe.

$$\sigma_{yz} = 10.47\text{E-4 N/mm}^2$$

Figure 6.7   Cooling Fluid: XY-Shear Stress Distribution in Leadframe.
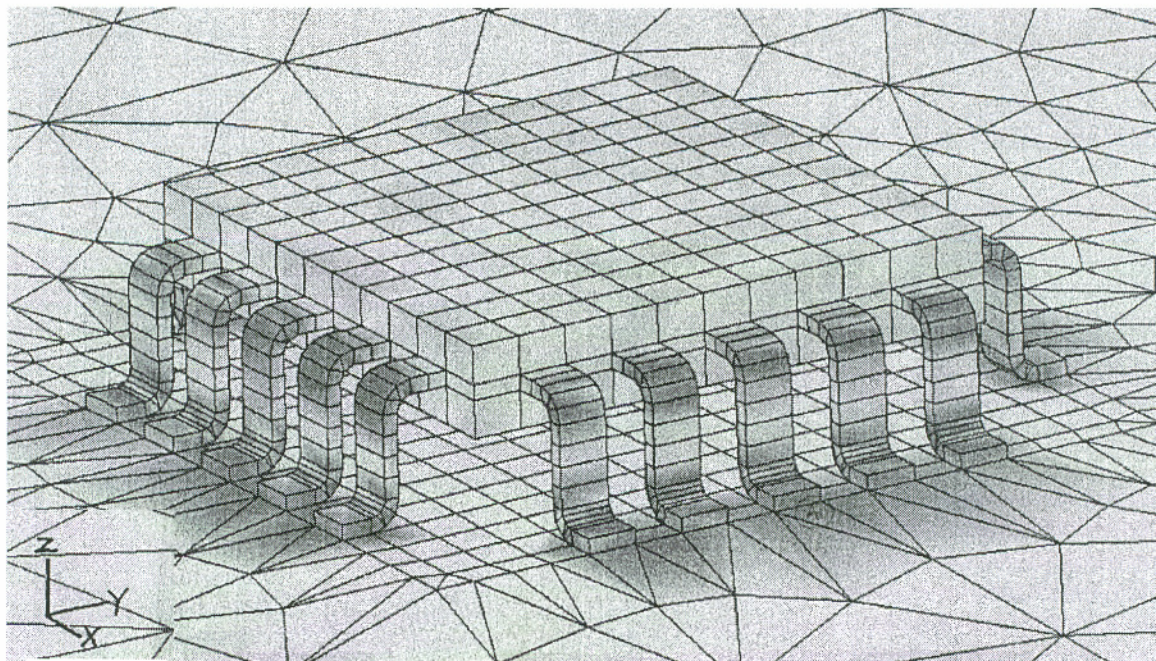
Figure 6.8   Thermal Analysis: Heat Flux Distribution.

$\sigma_{xy} = 41.8 \text{ N/mm}^2$

Figure 6.9   Thermal Analysis: XY-Shear Stress Distribution in Leadframe.

$\sigma_{yz} = 37 \text{ N/mm}^2$

Figure 6.10   Thermal Analysis: YZ-Shear Stress Distribution in Leadframe.

6.5   Optimization Problem Formulation: The objective function for this problem was derived based on the materials presented in chapter two,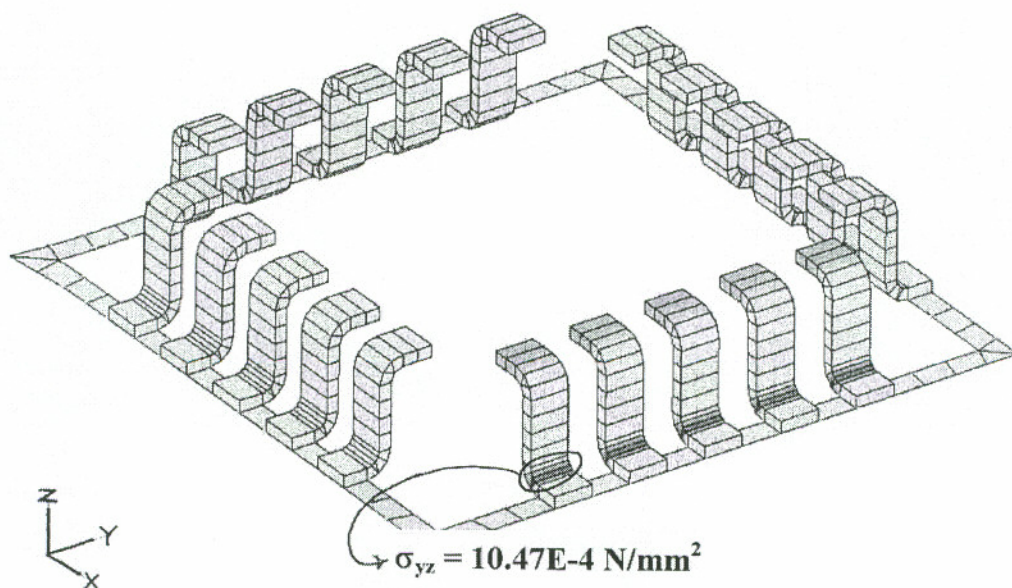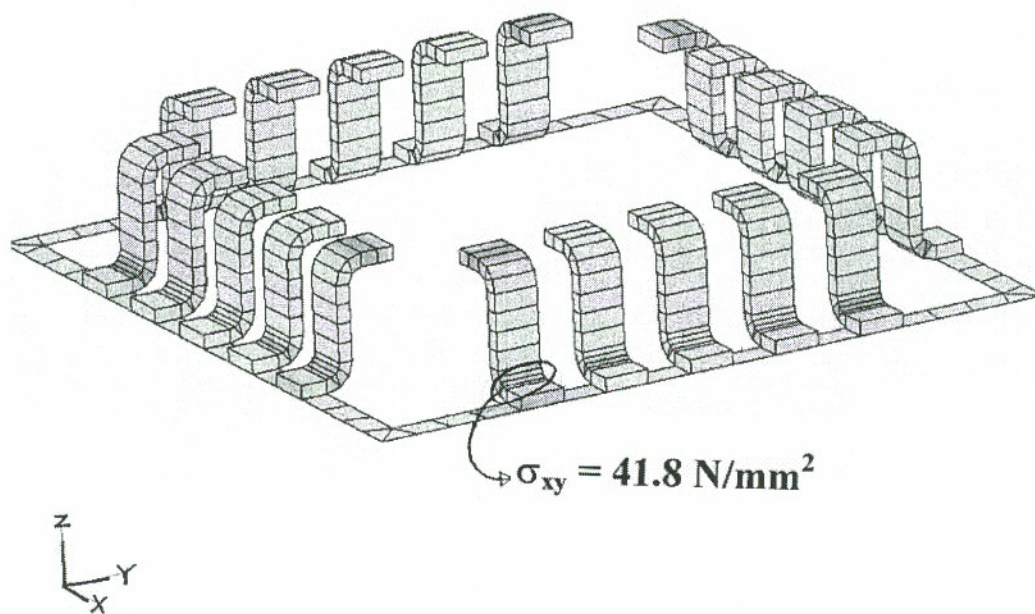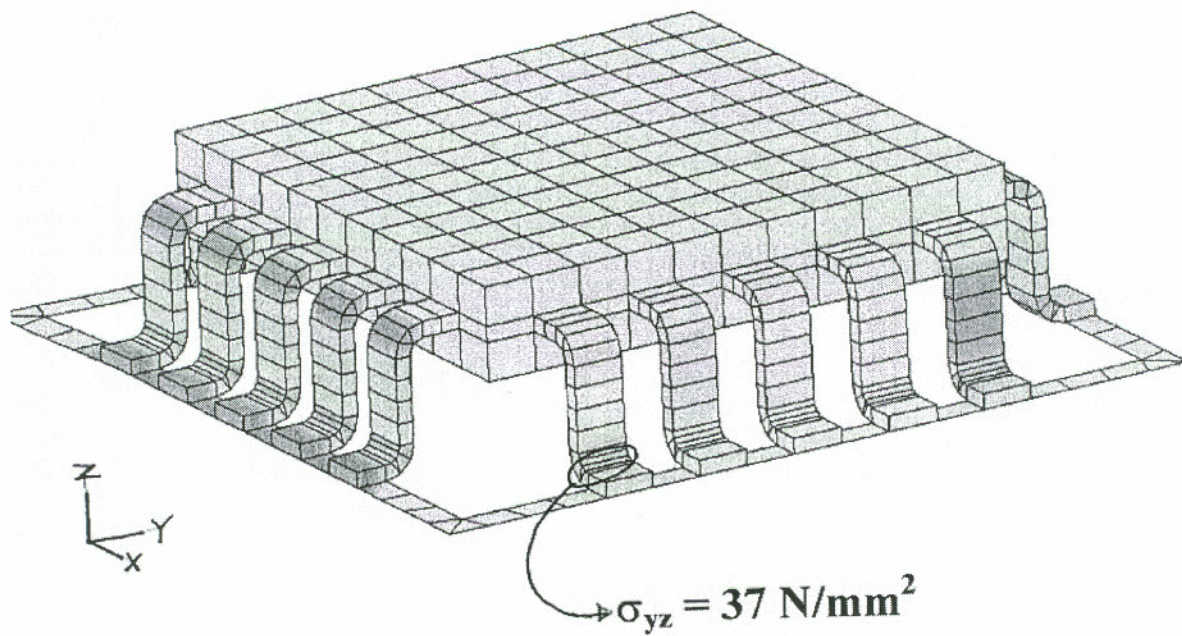 section 2.14 and 2.2.1, particularly, equations 2.28, 2.30, and 2.34. Heinrich and others,[32] provided numerical solutions to equation 2.34 for a large number of solder fillet shape as a function of the wetting angles, gravitational force, and surface tension. Partial summary of their results essential to this study and bounded by the wetting angles 0° to 90° was digitized with their values given in table 6.4. For practical limitations, a solder joint fillet having a wetting angle within this range was judged to be acceptable. The values in this table were adopted for this study.

Table 6.4   Possible Array of Solder Joint Fillet Shape Parameters.

Case Number	Solder Fillet Limits Height and Length (mm)		$\theta_1 = \theta_2 = 0^{\circ}$			$\theta_1 = \theta_2 = 90^{\circ}$		
	H	L	L/H	A/H^2	A_b	L/H	A/H^2	A_b
					(mm^2)			(mm^2)
$\sqrt{\dfrac{\rho \cdot g}{\gamma}} \rightarrow 0$	0.211	0.2058	0.975	0.2047	0.0091	0.2110	0.772	0.0344
$\sqrt{\dfrac{\rho \cdot g}{\gamma}} = 0.5$	0.189	0.2058	1.0886	0.2302	0.0082	0.189	0.841	0.0301
$\sqrt{\dfrac{\rho \cdot g}{\gamma}} = 1.0$	0.147	0.2058	1.4026	0.296	0.0064	0.147	7.088	0.0234

The main objective for this section of the study is to formulate a structural optimization problem that is based on the materials given in chapter two and tables 6.3 and 6.4. The problem is then solved for the minimum solder fillet area as a function of wetting angles, surface tension and gravitation forces. The resulting optimum fillet area must satisfy the shear and yield strength of 63Sn-37Pb eutectic solder alloy when subjected to thermomechanical forces given in table 6.3. To achieve our goal, we planned to compute the effective areas for the joint in xy-shear plane and xz-bond plane. For the shear plane, the area of joint footprint which was identical to the area of a rectangle was used while for the bond or peeling force fillet area was approximated by one-forth the area of an ellipse. Combining these areas and equations 2.28 and 2.31, and then making further simplification, the objective function for this study was obtained as:

$$f_p\left(A_p\right) = \frac{Q_p}{\left(2A_b + d.H\right)} \tag{6.1}$$

Subject to inequality constraint given by equation 6.2, which was derived, using figures 2.1 and 2.2.

$$\left[\frac{f_p\left(A_p\right)}{F_p}\right]^N + \left[\frac{f_{v\_total}}{F_{v\_allowable}}\right]^N = \leq 1.0 \tag{6.2}$$

In equations 6.2, the subscripts p and v represent bond and shear stress respectively. The equation reflect the contribution of shear stress present in the solder joint divided by the allowable shear strength of the alloy, and the bonding stress normalized by the allowable bonding stress of the alloy, all raised to power N. The significance of the equation 6.2 can be seen in two ways. First, it allows either the shear or bond stress ratios to approach unity depending upon the imposed load and solder geometry in order to abide by the unity limit. Secondly the equation is meant to proportion or balance the shear stress and bond stress under the given unity constraints and thereby satisfying the combined nature of the forces acting simultaneously on the joint. The objective function (equation 6.2) contains two types of design variables, the implicit and explicit variables. The wetting

angles, the surface tension, and the gravitational force are the implicit variables while the solder fillet area is the explicit variable, which is being optimized. All the other parameters used for the optimization analysis are given in table 6.5

Table 6.5   Solder Joint Fillet Optimization Parameters.

Parameters Definition	Symbol	Value	Units
Leadframe coefficient of thermal expansion	CTE_L	0.0000167	mm/mm °C
Solder coefficient of thermal expansion	CTE_S	0.0000247	mm/mm °C
Leadframe leg thickness	t_L	0.254	mm
Leadframe leg width	d	0.4115	mm
Temperature change difference	$Temp_{chg}$	30	°C
Leadframe leg curvature radius	R	0.381	mm
Cross sectional area leadframe leg	A	0.1045	mm^2
Thickness of solder material directly under leadframe leg	t_S	0.0254	mm
Maximum height of solder fillet as function of wetting angles	H	0.211	mm
Maximum length the solder fillet may spread as a function of wetting angles	L	0.2428	mm
Effective contact length of the solder joint	L_{eff}	1.6287	mm

Table 6.5 Solder Joint Fillet Optimization Parameters Continued.

Geometric constant associated with the curvature of the leadframe leg	A_m	0.166848892	mm
Solder-Leadframe contact that area assumed to be effective	A_{eff}	0.670198395	mm^2
Solder-Leadframe interface bonding effective factor, lies between 0 to 1.0	pis	0.5	
Total shear force acting at the shear plane due to thermomechanical effects	Tau_total	4.626	N
Poisson's ratio of solder material	v	0.4	
Allowable Joint bonding stress as reported in reference [73]	F_p	27579.04	N/mm^2
Solder material modulus of elasticity	E_s	44800	N/mm^2
Soder material shear modulus	G_s	16000	N/mm^2
Total axial stress on the leadframe resulting from thermomechanical effects	P	5.79	N/mm^2
Exponted used to normilzed the combined effect of shear and axial forces	N	2	
Allowable Joint shear force at solder shear plane as reported in reference [73]	Fv_allowed	87.6	N/mm^2
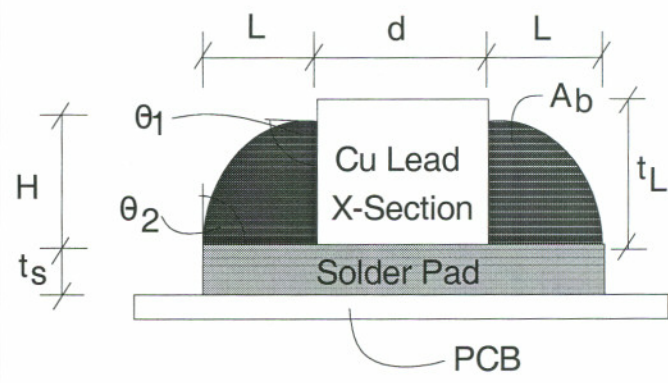
Close examination of both equation 6.1 and 6.2 indicates that, they are nonlinear functions with one explicit design variable and therefore can be solved by a classical optimization method, called the nonlinear programming algorithm. Though stochastic optimization methods may be used for this problem, the classical method is preferred due to the small number of design variable(s) involved in the problem. Also, both minimum and maximum solder fillet areas bound the solution space. The results of the structural optimization analysis are given in table 6.6.

Table 6.6   Summary of Computation of Optimization Analysis.

Constant used for equation 2.30	C1	1.17244	
Constant used for equation 2.30	C2	76.8	
Maximum Solder bonding Stress caused by thermomechanical loads	Qp	94.6924	N/mm^2
Total shear stress at shear plane (Thermomechanical + Solder-Cu Expansion)	f_{v_total}	87.5818	N
Solder Area Practical Limits $(0.0064 < Ab < 0.03436)$ mm^2	0.0064	0.0344	mm^2
Results			
Objective function (minimized)	$fp(A_b)$	562.8249	N/mm^2
Constrain function	$g(A_b) < 1.0$	0.999999889	
Optimum Solder Joint Fillet Area Computed	A_b	0.03416	mm^2

Table 6.7 contains the optimum shape predicted by the optimization analysis based on the the combined thermomechanical load. It corresponds to the following solder joint fillet physical and geometric parameters shown in the table. Figure 6.11 shows the full solder joint of a single joint based on the optimum joint in table 6.7

Table 6.7   Optimum Solder Fillet Shape.

Wetting Angles	Gravity to Surface Tension Ratio	Optimum Shape Parameters		
$\theta_1 = 90°$ $\theta_2 = 90°$	$\sqrt{\dfrac{\rho \cdot g}{\gamma}} \to 0$	Cross Section through Gullwing Solder Joint		
		$L = 0.2428$ mm $H = 0.211$ mm Optimum Area $(A_b) = 0.03415$ mm^2 $t_S = 0.0254$ mm $t_L = 0.254$ mm		

6.6   **Local Finite Element Model (Single Solder Joint)**: For this phase of the study, the solder joint alloy was assumed to follow isotropic elastic-plastic material behavior. Therefore, the strain hardening modulus, the bulk modulus, and the elastic properties used for the analysis were taken from table 2.1 of chapters 2. In sum, the thermomechanical properties used to augment the local model are shown in table 6.8. To simulate the time related solder deformation response that is necessary for material nonlinear analysis, the load coefficients shown in table 6.3 were applied incrementally with time and summarized in table 6.8 for period of 0.0201 seconds.

Table 6.8   Local Finite Element Model Data.

LOAD HISTORY		ELASTIC- PLASTIC 67SN-37PB SOLDER ALLOY
Load Coefficient	Time (sec)	E = 48.2 MPa
0.0	0.0	G = 17.2 MPa
0.25	0.002	$\upsilon = 0.4$
0.50	0.004	
0.70	0.006	Yield Stress = 10.0 MPa
0.88	0.008	Hardening Modulus = 234 MPa
1.0	0.07	Bulk (volume) Modulus = 88.33 MPa
1.0	0.0201	

The model was made up of 10,552 8-node solid elements and 12,330 connecting nodes. The finite element model was built based on the optimum fillet area shown in figure 6.11. The results of the analysis in a form of both stress contours and stress verses element identity are given below in figures 6.12 to 6.19. The stresses includes, the Von Mises, maximum shear stress and the bond or peeling stress. The large deformation analysis was performed using the commercial finite element analysis code Stardyne.[105]
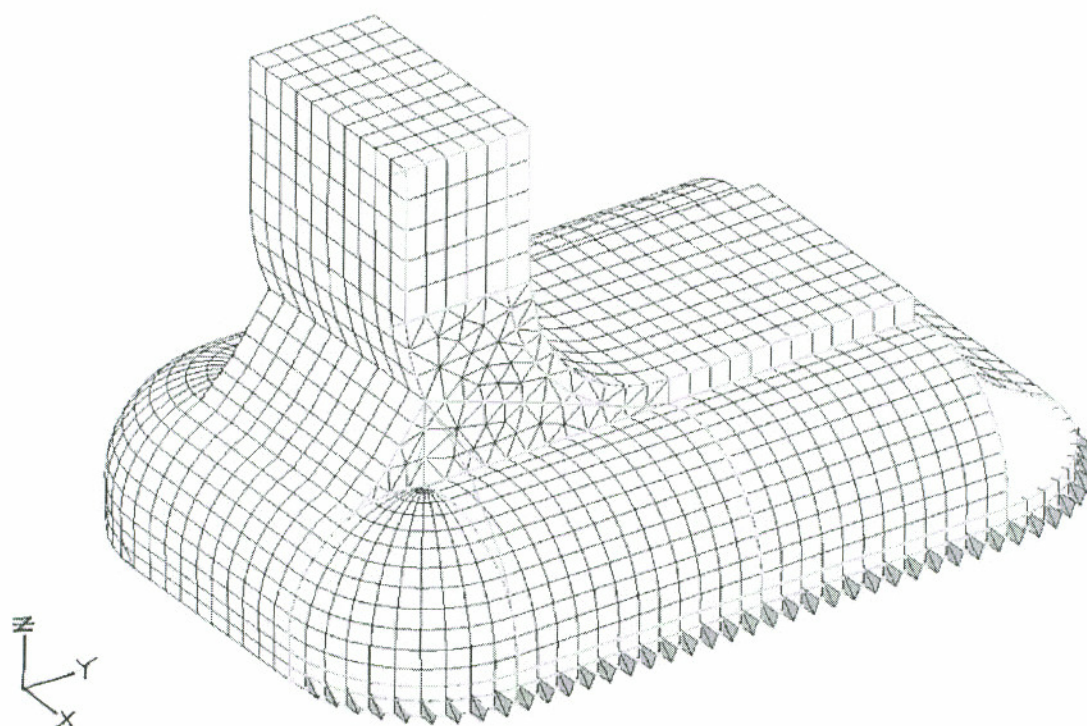
Figure 6.11   The Local Finite Model of the Optimum Solder Joint Geometry.

a)
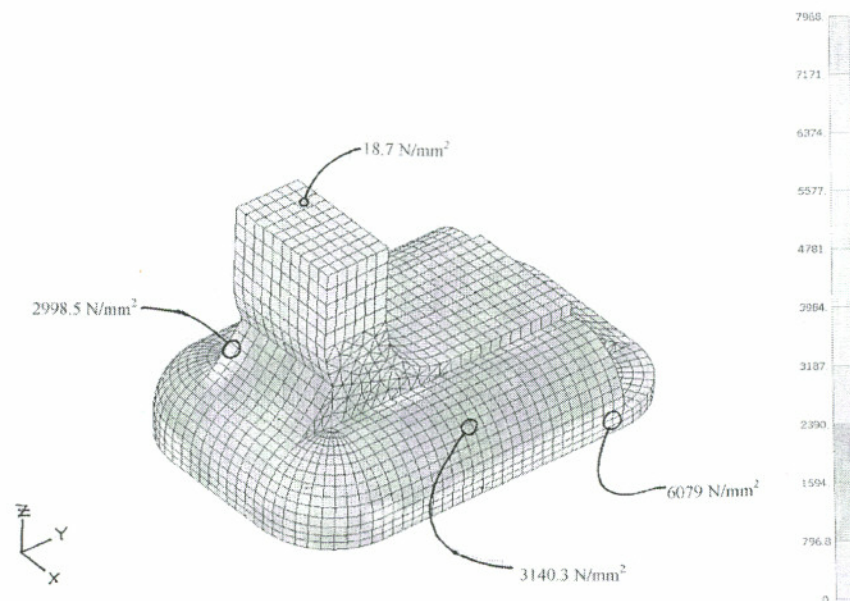
b)
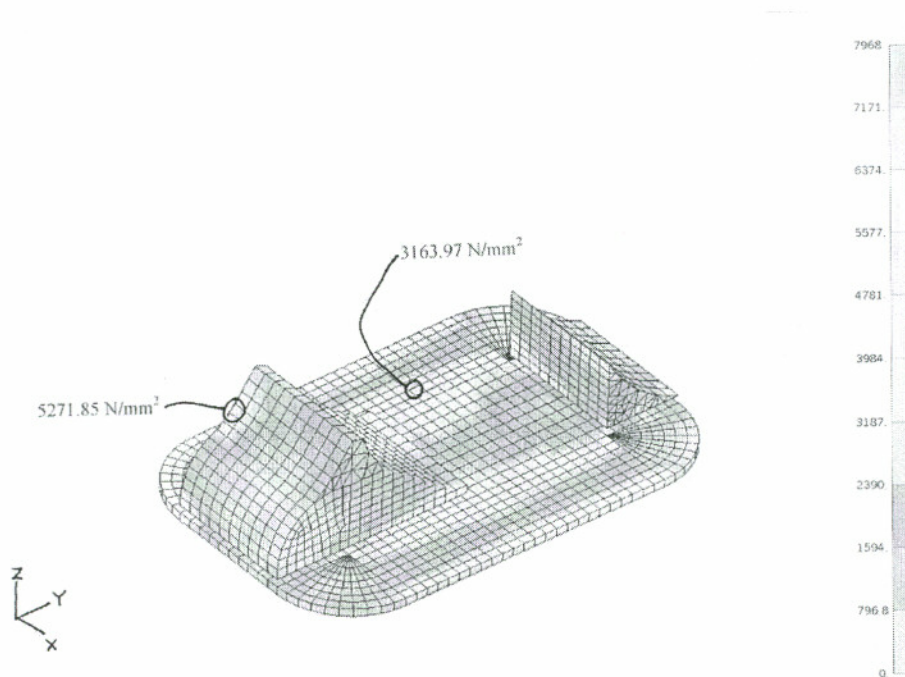
Figure 6.12   Von Mises Stress Contours a) Full Model b) Partial Model.
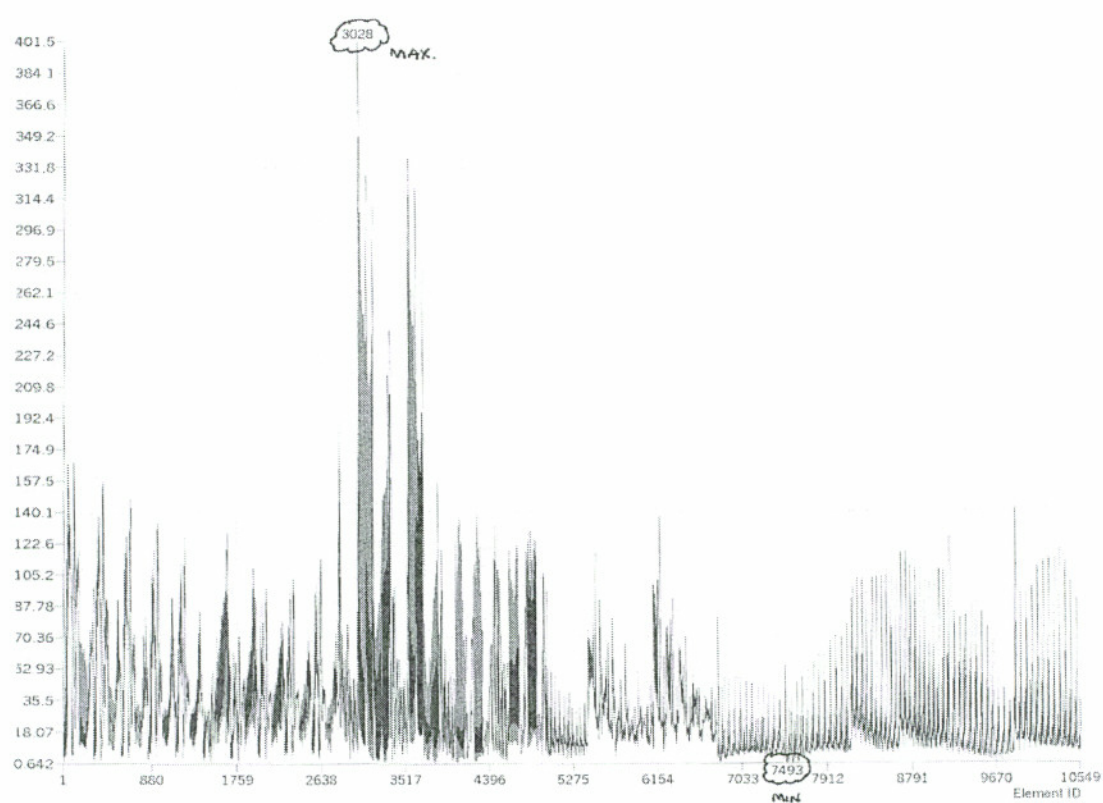
Figure 6.13   Stress Plot Von Mises Stress versus Element Numbers.
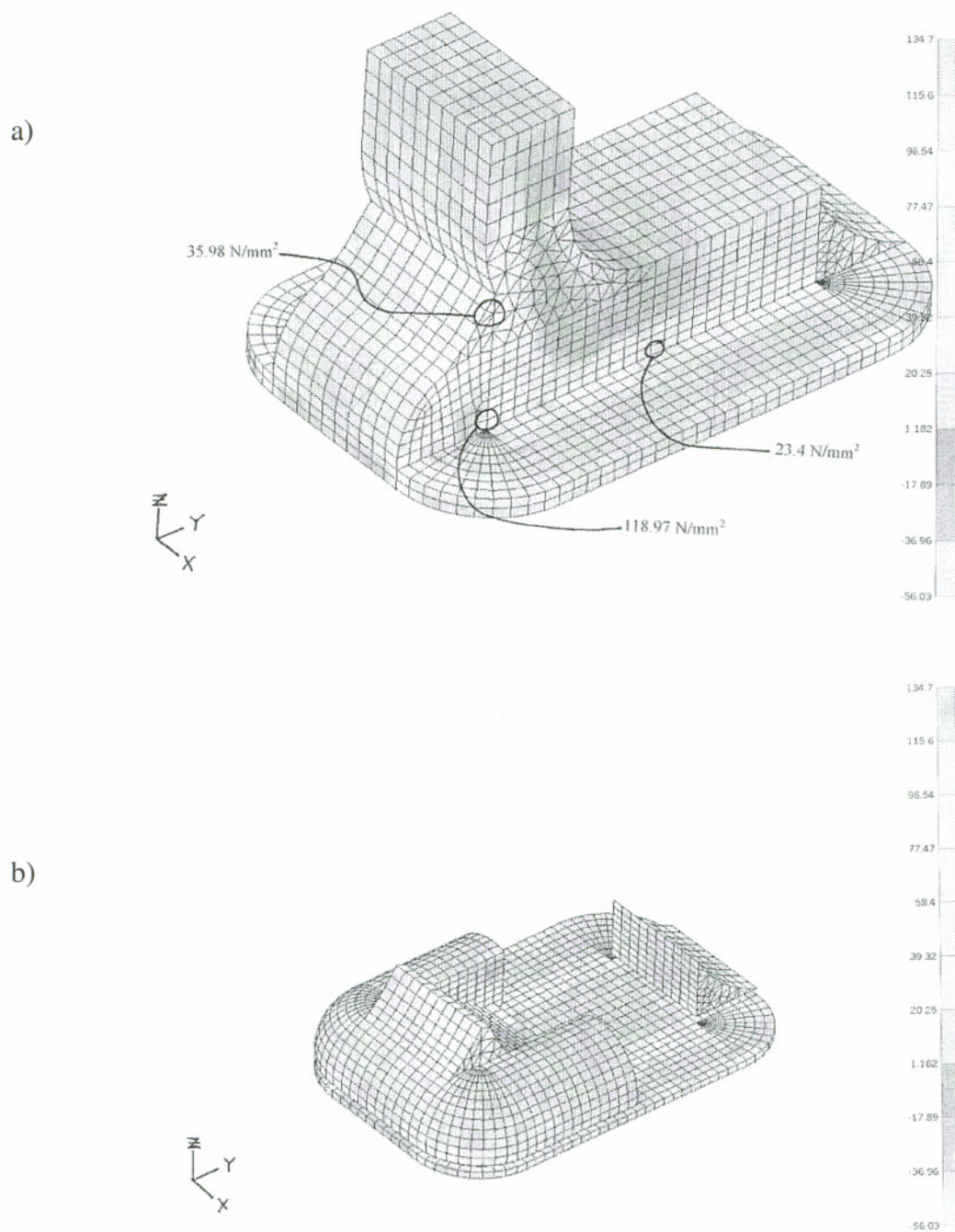
Figure 6.14   Peeling (Bond) Shear Stress Contours: a) Full Model b) Partial Model.
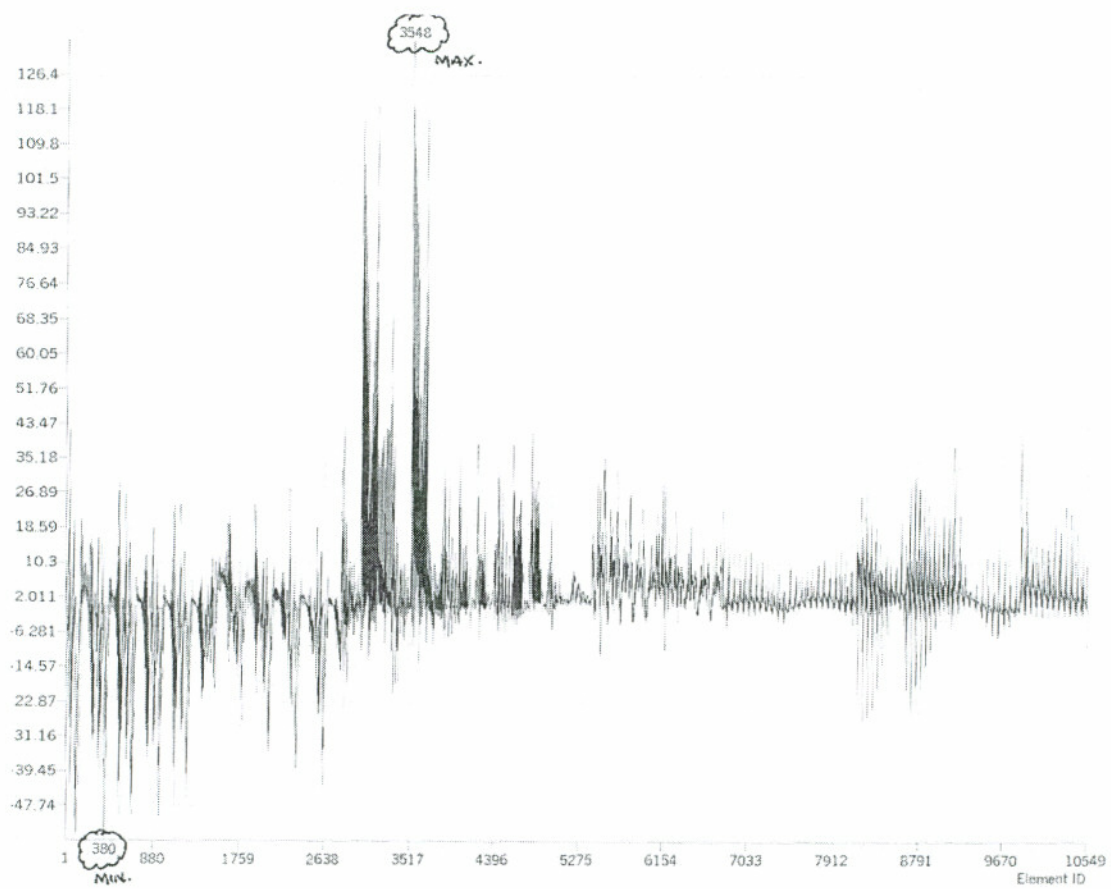
Figure 6.15   Peeling (Bond) Shear Stress versus Element Numbers.
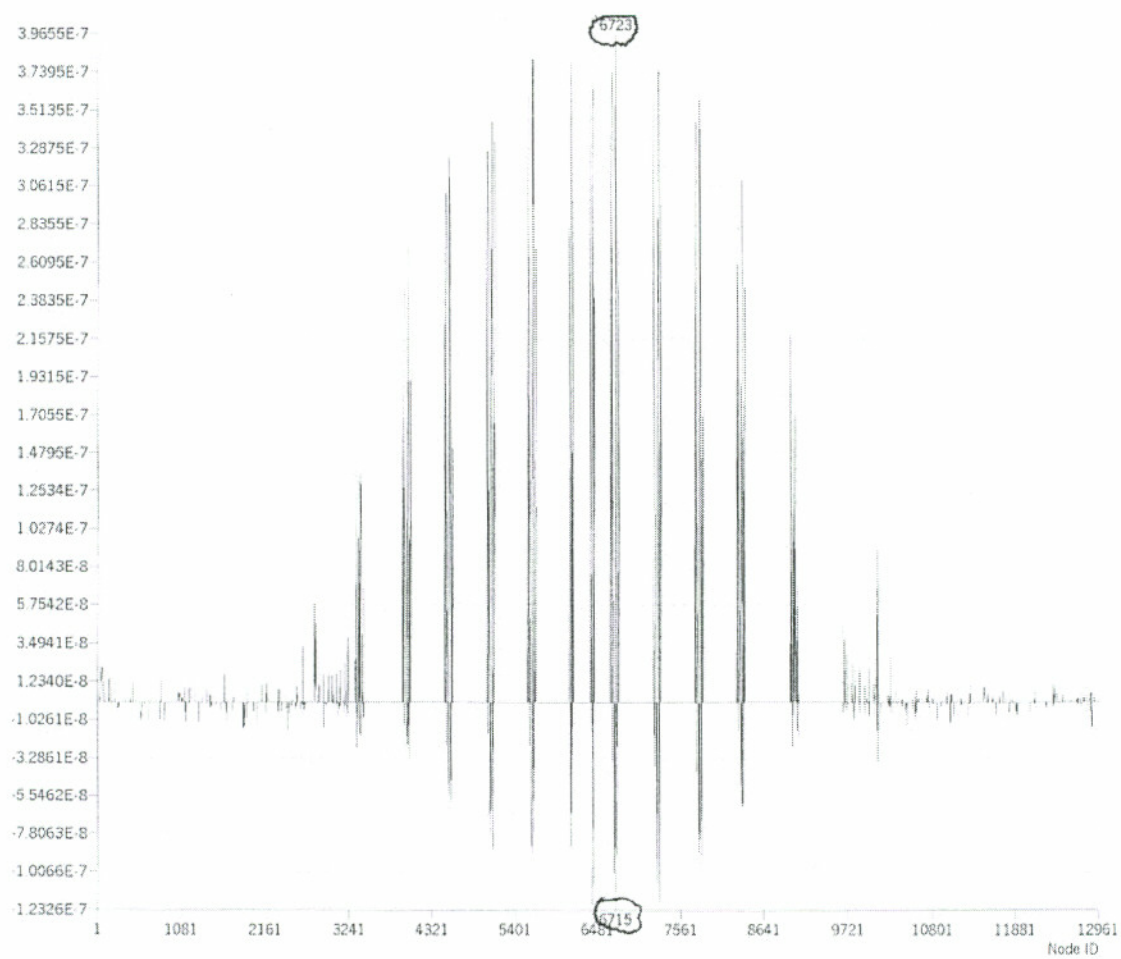
Figure 6.16   Peeling (Bond) Shear Force Displacement versus Nodal Numbers.
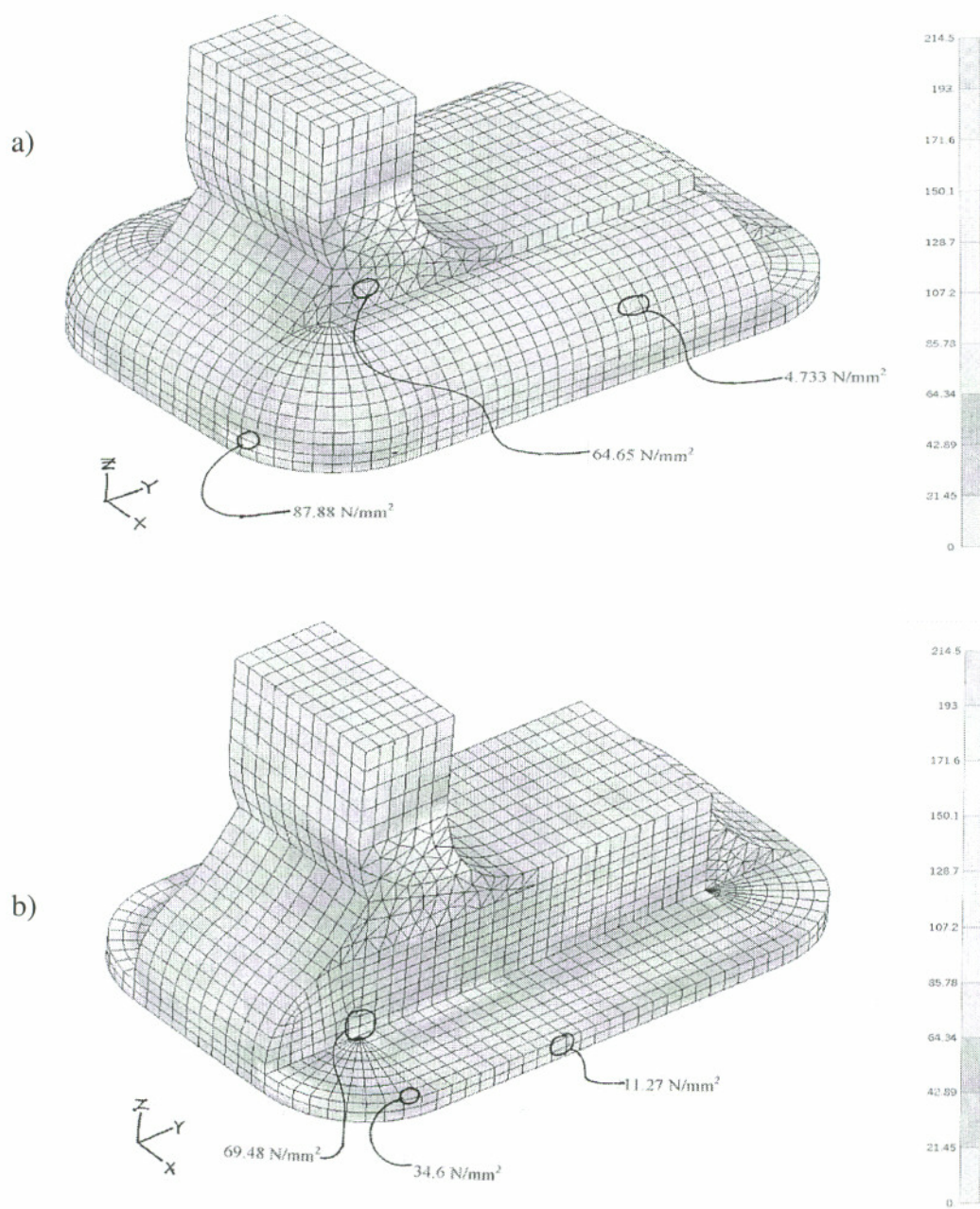
Figure 6.17   Maximum Shear Stress Contours: a) Full Model b) Partial Model.
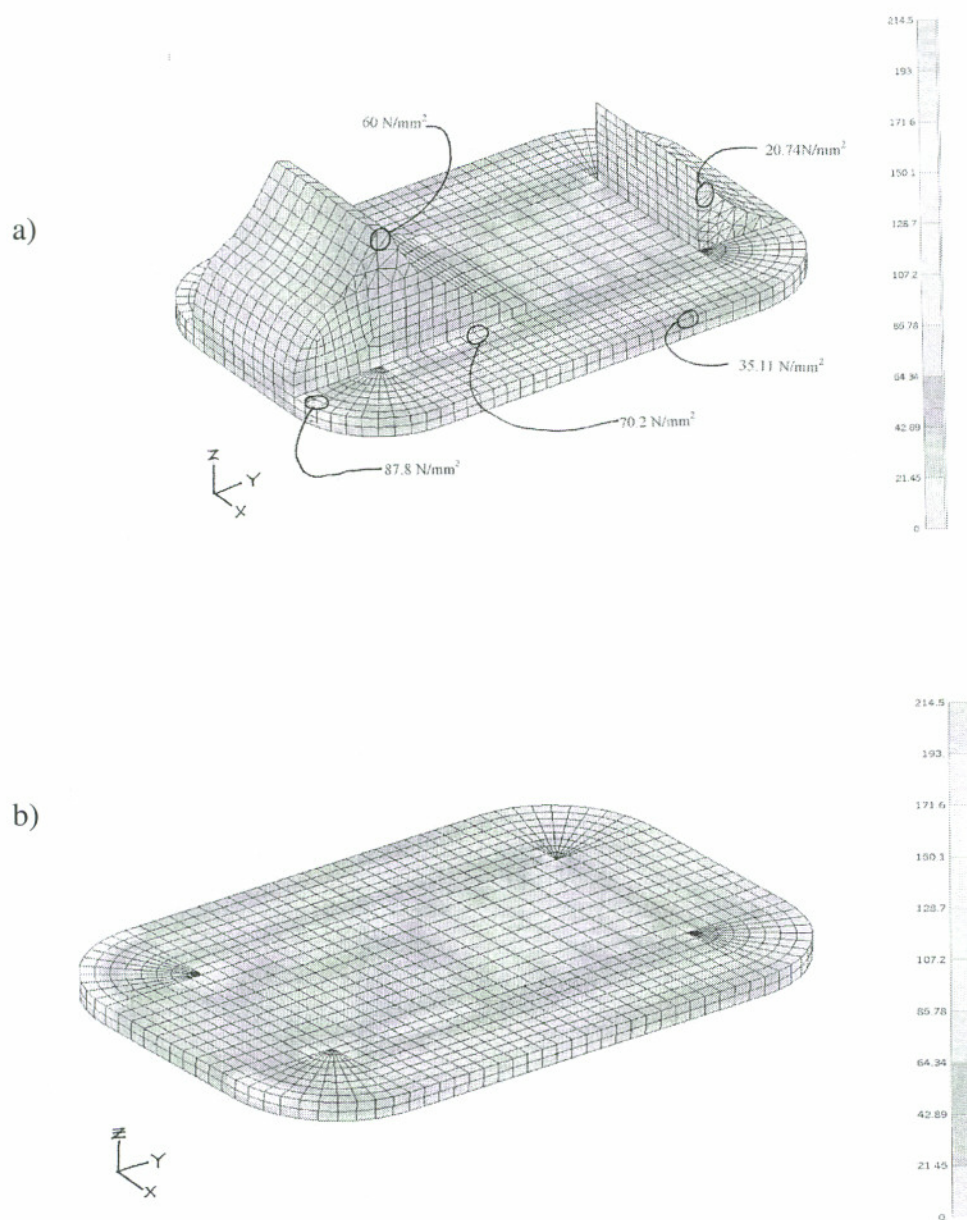
Figure 6.18   Open Solder Joint Component showing Maximum Shear Stress Contours.

$Q_{P\,(max)} = 118.97\ \text{N/mm}^2$
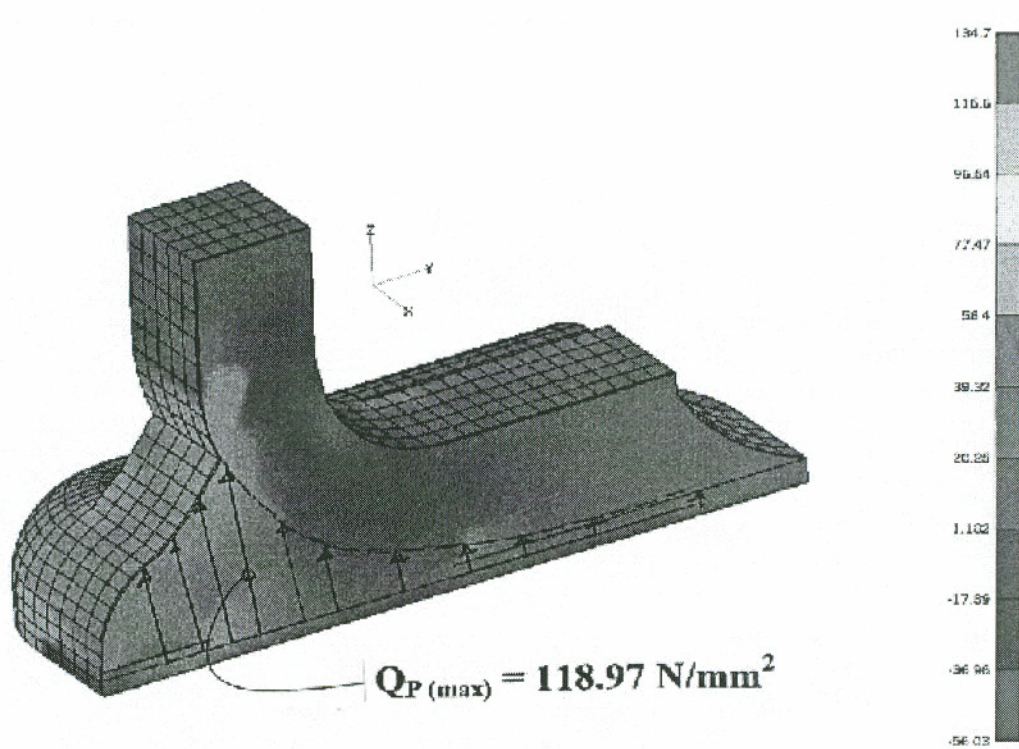
Figure 6.19   Peeling (Bond) Stress Profile along solder joint.

CHAPTER SEVEN

DISCUSSIONS AND CONCLUSIONS

7.1 **General Summary**: The multidisciplinary approach to reliability studies in electronic packaging for the past decade has received much greater attention both in academia and industry. The area of solder joint integrity in electronic packaging has seen particularly noticeable activity because of the current trend of component miniaturization leaving much smaller surfaces for the high power generating components to dissipate increasing level of thermal energy. This trend led to the motivation for the development and the presentation of multidisciplinary materials in chapters 2 to 5. These chapters represent the foundation blocks for this dissertation, and subsequently, the successful application to 20-pin CQFP chip module solder joint discussed in chapter 6.

Chapter 1 of the dissertation provided the introductory materials and the motivation for studying the topic: *thermal-structural optimization and reliability of solder joint geometry in electronic packaging*. It also, laid out the blueprint for the elements of this dissertation work. The materials presented in chapter 2 deals with the mechanics of materials as it relates to 67Sn-37Pb, near eutectic solder joint alloy. A damage continuum mechanics concept was introduced and used to model the thermomechanical behavior of the alloy for the first time in solder joint reliability studies. Also, a new bond force model was proposed and used to predict the permissible forces that a given gullwing leadframe solder joint may experience but retain linear elastic response. Further discussion on these two key contributions, made by this dissertation to solder joint reliability studies will be discussed in detail in sections 7.1.1 and 7.1.2.

A comprehensive treatment of thermomechanical loads formulation for electronic packaging was given in chapters 3 and 4. They cover classical composite theory used to study the epoxy fiber reinforced PCB, structural dynamics principles, particularly in the area of random vibration. Heat transfer concepts and analysis strategies as they relate to electronic packaging application were also discussed those chapters. Chapter 5 covered structural optimization techniques, which serves as the central component of the studies by bringing all the multidisciplinary elements, presented in the other chapters of the study, together so that the optimum solder joint fillet area can be sought out.

Chapter 6 examined the validity of the materials in chapters 2 to 5 by direct application to a 20-pin CQFP chip, surface mount module solder joint. It showed systematically, how the two proposed modeling methods can greatly enhance the modeling of solder joint by reducing most of the complexities in joint reliability studies. From the results derived from the study, the relationship that exists between the physical solder alloy molten properties to thermomechanical loads and how they ultimately affect solder joint integrity are highlighted.

7.1.1 Proposed Solder Bond Stress Model: Many different bond (peeling) interface stress models for solder alloy-to-leadframe in solder joint studies have been proposed in literature.[23-25] The derivation of some of these models are based on first principles and therefore are limited in their application to some solder joints, particularly gullwing and J-type connections. The few existing models, which are semi-analytical, do not fit the boundary conditions posed by these two types of solder joint.

Solder joints in electronic packaging are made of assemblies of different components whose geometric dimensions may not be symmetric along the length of the joint and therefore limits the use of these methods in real life applications, as evidenced in

both textbooks on this subject and other published literature. To circumvent the problem, a new bond force model that considers the whole solder geometry was proposed and presented. The expressions used to predict the interfacial bond force between leadframe and solder fillet was based on the global joint parameters and the prying deformation of a fictitious equivalent bolted leadframe joint.

In order to determine the interfacial bond force (stress) between leadframe and the solder fillet for a given solder joint, the actual joint was transformed into an equivalent fictitious bolted joint shown in figure 2.1. The axial force or cramping force, in the bolt was assumed to be equal to the sum of all the infinitesimal bond forces that are present at the bi-material interface due to the soldering action. At this point, the objective was to find the unknown bond forces based on the bonding material's permissible strength values, which normally is obtained from test.

Knowing the distribution of the interfacial bond stress along the length of the joint, the bond force, Q_p, expression was derived using the geometry parameters of the joint and Castigliano's curved beam energy theory. For gullwing leadframe solder joint used for this study, the bond force expression was given by the following equation 2.31, which was developed in chapter 2.

$$Q_p\left(x = L_{eff}\right) = 4PL_{eff}\left(C_1 + C_2\right)\varphi$$

The key to using this new method for other types of solder joints lies in the ability of the analyst to predict the bond stress distribution along the length of the joint. This presents a significant analysis challenge as demonstrated by the details of predicting bond stress profile for a given joint in this study.

For this type of joint, through a series of finite element solder joint simulations, the bond stress intensity profile in the joint was found to follow parabolic function having the peak values at the heel of the joint, see figure 2.2 and 6.14a. The maximum value of Q_p for this study was limited to the alloy's peeling strength. This assumption was considered reasonable, since in many joining processes, the strength of the joint material is normally stronger than the base materials.[30]   The bond force equation 2.31 include a factor φ, ranging from 0 to 1, that accounts for different degrees of bonds that may arise due to poor bonding interface conditions. For a perfect bond the factor of φ is unity. This factor is meant to recognize some of the poor bonding conditions seen in reflow soldering processes. In addition, the equation also makes provision for the internal thermally induced force within the solder joint due to mismatch of the joint materials coefficient of thermal expansion.

The significance of the proposed model can be seen in many areas of solder joint reliability studies. For example, given a solder joint configuration, the model can be used to predict the allowable thermomechanical loads that a chip component can transmit through the leadframe to the joint and still maintain its integrity. It can also be used for preliminary solder joint reliability studies to gain insight to the problem as a prelude to the more involved and expensive finite element analysis as demonstrated in this study. The results of the local verification model are shown in figures 6.12 to 6.19. These indicate that these new approaches proposed in this study are valid, since all the stress are within the value of Q_p used to predict the optimum solder joint fillet shape.

7.1.2. Thermomechanical Properties of 63Sn-37Pb Solder Alloy Modeling: The success of the study was contingent upon the selection of the right constitutive relationship among the many other models found in the literature. The variability of eutectic or near-eutectic Sn-Pb alloys is so large that no two identical thermomechanical property sets could be found in published research papers on the same subject, among the hundreds of papers examined.

The need to explore a statistical method that could provide a reasonable level of confidence beyond the standard data fitting method was considered. Neural network statistical method was found to be appropriate for this study. A neural network is a network associated with mathematical algorithm, and was used to simulate the behavior of eutectic alloy to thermomechanical loads. The network has the ability to learn the test data of the alloy by adaptation of the weights it assigns to each data set or point.

It is generally postulated, as an experimental fact, that yielding of a material can occur if the stress σ, in the material satisfy general criterion $F(\sigma, \kappa) = 0$, where κ is a hardening parameter. The yield condition may be visualized as a surface in n-dimensional space of stress with the position of the surface dependent on the instantaneous value of the state parameter κ. For eutectic solder, at high temperature, the rate at which creep strain develops depends not only on the current state of the stress and the strain but, on the full history of the development. Thus, to determine the increment of strain at a particular time interval, it is necessary to know the history or the state of stress and strains at all preceding time intervals.

Neural network algorithms are well known for learning systems with nonlinear histories and making predictions with good results. For this study, the mapping and learning capability of neural networks was recognized as a material constitutive modeling tool for synthesis and optimization of the test data, particularly, for strain rate dependent eutectic Sn-Pb solder material properties. The network was trained to identify all the

limiting constraints that exist between the low and high strain rate data shown in table 5.2 by diagnosis of the data sets, interpreting the data sets, debugging or removing extreme data points, making prediction and validating the prediction during its operation. The data set in table 5.2 consists of five high strain rate data, columns **A** to **E**, and three low strain rate data sets columns **F** to **H**.

To predict the strain hardening modulus κ, needed for continuum damage mechanics model, the network evaluated the performance of 480 different network types and retained the potential ten good ones, given in table 5.4. The tenth network was considered to be the best. To optimize the strain hardening modulus κ, while satisfying the strain rate dependence constraints, the network eliminated data groups **A** and **G**, high and low strain rates data, respectively. Through this process, a unified elastic-plastic, isotropic model was obtained for the analysis of the local finite element verification model. During the neural network analysis, the strain was made the dependent variable.

The statistical results of the analysis are given in table 5.3. The computed standard deviation ratio between the data mean and the predicted mean were found to be 0.0126, with a corresponding correlation coefficient of 0.99223. These are good modeling indicators and confirmed that neural networks were successfully used to predict eutectic solder material constitutive parameters. A standard deviation ratio of 1.0 implies that, the network is modeling the data set in the same manner as any other regression method that uses simple averages. For this study, all the indicators mentioned above, are given in table 5.3 are much lower than unity with correlation coefficients close to unity, hence the results are acceptable. The Von Mises yield criteria was used for these studies as shown in figures 6.12 and 6.13.

7.1.3 The Optimum Solder Joint Fillet Shape: The optimum solder fillet shape shown in table 6.7 was obtained using equations 6.1 and 6.2. These equations were formulated for gullwing leadframe solder joint based on structural optimization techniques. Surface mount technology permits reflow soldering process to be used to attach electronic components to PCB and other system level elements. The shape of the final, solidify shape as the result of reflow process is dependent upon the solder alloy's physical properties, including surface tension, density, gravity, and the wetting angles. In the past, researchers have focused mainly on the stress analysis of the joint and the prediction of fatigue life under a variety of cyclic loading (thermal and mechanical) conditions. A comprehensive treatment of the problem has not received the attention as evidenced by published research papers.

In light of this, and recognizing that, the final geometry of the solid solder joint subjected to thermomechanical load will influence the joint performance, a new approach that considers the problem at all phases of the joint, starting from the joint formation to the joint service environment was proposed and implemented for this dissertation. The relationship between surface tension, gravity, and wetting angles associated with molten solder shape formation when subjected to thermomechanical loads was studied comprehensively for the first time in this dissertation. The global finite element results and structural optimization principles were used to obtain the optimal solder joint geometry. The bond force model and the neural network material model were used to formulate both the objective and the constraint functions, which were nonlinear and therefore required nonlinear programming algorithm to solve them.

The design space was established by the practical requirements mandated by the electronics industry. These include the solder area (volume) of the reflow solder, the leadframe leg cross-sectional dimensions, the copper pad length, and wetting angles ranges, between $0°$ to $90°$, as summarized in table 6.4 and figure 6.7. The upper limit on the wetting angles is aimed at preventing two adjacent solder joints from bridging. This approach yielded objective and constraint functions that are well posed for structural

optimization analysis, containing only one explicit variable. The indirect link between the explicit and the implicit variables were maintained so that once the optimum solder fillet area was found, the rest of the variables (surface tension, gravity, wetting angles) the rest could readily be determined.

The optimum fillet area corresponds to the case where the ratio of gravity-to-surface tension forces is almost zero, with both wetting angles, being $\theta_1 = \theta_2 = 90^\circ$. The constraint function $g(A_b)$, became active with its value equals to 0.99999889, almost approaching the unity limit. The results suggest that, in solder joint reliability studies, the influence of the gravitation force on the molten solder geometry formation is negligible and hence can be ignored mainly due to the small size of the joint. Solder joint reliability models, which are based mainly on surface tension theory, were thus deemed adequate to characterize the solder joint formation phenomenon. To resist the joint in-plane shear force induced by the thermomechanical loads, a large shear plane area was needed and hence the 90° wetting angles.

The local finite element model based on the predicted optimum fillet area is shown in figure 6.11. Finite element results for the local model are given in figures 6.12 to 6.19. It can be seen from these figures that, the entire shear and the bond or peeling stresses are all within the allowable values given in table 6.5, used for the optimization analysis. These results confirmed that, the optimum solder fillet predicted by the structural optimization analysis using the proposed bond force model was indeed optimum, since there are no stress violation. It can be concluded from this section of the study that, the relationship between molten solder shape formation parameters and thermomechanical load for solder joint performance are strong and hence should be investigated in order to address solder joint reliability problems comprehensively.

7.2   Main Conclusion: The problem of optimizing leadframe solder joint geometry for thermal-structural integrity in electronic packaging was examined using both theoretical and practical applications. It was found that, for a given gullwing leadframe solder joint formed from reflow soldering process, there exists a direct relationship between the physical properties of the solder and the thermomechanical loads that result in the final solder fillet shape. This relationship holds true with the assumption that the shape of molten fillet will remain unchanged after solidification. A methodology for presenting the optimum fillet shape for joint integrity given thermomechanical loads was proposed and demonstrated. The following conclusions may be drawn from work done for this dissertation:

1. The relationships between solder joint formation parameters (surface tension, gravity, wetting angles) and thermomechanical loads in terms of solder joint integrity is strong, and therefore must be integral component of solder joint reliability studies.

2. For relatively small solder joints, the optimum solder joint fillet for a given thermomechanical load is dependent on surface tension force and the wetting angles only. The impact of gravity force on the fillet shape is negligible and hence can be ignored in joint reliability studies.

3. Continuum Damage Mechanics and Neural Network principles can be use successfully to model the hot deformation behavior of 63Sn-37Pb constitutive parameters.

4. The proposed interfacial bond force model can be used to predict the resultant bond forces present between the leadframe and the solder alloy in gullwing leadframe joint. This model can be used as both an analysis and design tool in solder joint reliability studies.

5. The interfacial bond shear and shear stress along the length of the solder joint are not uniform and, therefore, models that are based on symmetry conditions are not appropriate to sufficiently characterize these stress profiles.

7.3   **Future Work**: This study was centered on gullwing leadframe solder joint in electronic packaging. There are other types of joints used in electronic packaging where the concepts derived in this dissertation can be used. Therefore, pertinent directions for one to pursue are to extend these concepts to those joints, including J-leadframe solder joint and ball grid array (BGA), in order to enhance the performance of these joints when subjected to thermomechanical loads. Also, the new proposed interfacial bond force model should be expanded to other joints in order to assemble potential bond stress distribution profile along the length of a given joint required for the full utilization of the proposed interfacial bond force model.

REFERENCES

1. Seraphim, D. P., ed. Principles of Electronic Packaging. New York: McGraw-Hill Company, 1989. pp. 1.

2. Hannemann, R. J., et al., Semiconductor Packaging – A Multidisciplinary Approach. New York: John Wiley & Sons, Inc., 1994. pp. 607, 650-653.

3. Bar-Cohen, A., and Kraus, A. D., ed. Advances in Thermal Modeling of Electronic Components and Systems. New York: ASME Press, 1993. Vol. 3, pp. 61, 262-263, 275.

4. Ohring, M., Reliability and Failure of Electronic Materials and Devices. San Diego: Academic Press, 1998. pp. 415, 527, 557, 435.

5. Barker, D., et al, "Combined Vibrational and Thermal Solder Joint Fatigue – A Generalized Strain verses Life Approach," Journal of Electronic Packaging, Vol. 112, 1990, pp.129-133.

6. Wong, T., et al, "Establishing the Shock Fragility Limit for Liquid Crystal Display: Some Recent Approaches and Results," Mechanics and Materials for Electronic Packaging, Chicage, 1994. New York, ASME 1994. pp.14, 161-165. (AMD, Vol.187)

7. Li, Y., et al., "The effect of Stencil Printing Optimization on Reliability of CBGA and PBGA Solder Joints," Atlanta, GA, 1996. New York: ASME Press, Vol. 120, March 1996. pp. 54-60.

8. Li., Y., and Mahajan, R. L. "CBGA Solder Fillet Shape Prediction and Design Optimization" New York: ASME Press, Journal of Electronic Packaging, Vol. 120, June 1998. pp. 118-122.

9. Davis, L., and Steenstrup, M., Genetic Algorithms and Simulated Annealing. Los Altos, CA., Morgan Kaufmann Publishers, Inc., 1987. pp. 2-8.

10. Brown, W.D., ed. Advanced Electronic Packaging: With Emphasis on Multichip Modules. IEEE Press, 1998,. pp. 40.

11. Lau, J. H., ed. Solder Joint Reliability: theory and Applications. Van Nostrand Reinhold, New York, 1991. pp. 266.

12. Akay, H. V., et al. "Fatigue Life Predications for Thermally Loaded Solder Joints Using a Volume-Weighted Averaging Technique," Journal of Electronic Packaging, Vol. 119, 1997. pp. 228-235.

13. Skrzypek, J.J., and Hetnarski, R.B., Plasticity and Creep-Theory, Examples, and Problems. Florida, CRC Press, Boca Raton, 1993. pp. 3, 4, 358-370.

14. Boresi, A.P., et al., Advance Mechanics of Materials. 5th ed. Canada: John Wiley & Sons, 1993. pp. 28-101, 385-392.

15. Lau, J.H., and Pao, Y., Solder Joint Reliability of BGA, CSP, and Flip Chip, and Fine Pitch SMT Assemblies. New York, McGraw-Hill, 1997. pp. 124,125,

16. Gilat, A., and Krisha, K., "The Effects of Strain Rate and Thickness on the Response of Thin Layers of Solder Loaded in Pure Shear", Journal of Electronic Packaging, Vol. 119, 1997, pp. 81.

17. Devletian, J. H., Private Communication, Oregon Graduate Institute, January 1999.

18. Lau, J. H. ed. Solder Joint Reliability - Theory and Application. New York, Van Nostrand Reinhold, 1991. pp. 279.

19. Frear, D.R., and Kinsman, K.R., Solder Mechanics - A State of the Art Assessment. Warrendale, PA, Minerals, Metals, and Material Society, 1991. pp. 140.

20. Bhattachaiya, B., and Ellingwood, B., "Continuum Damage Mechanics – Based Model of Stochastic Damage Growth," Journal of Engineering Mechanics, September 1998. Pp. 1000-1009.

21. Muju, S., et al., "Predicting Durability," Mechanical Engineering Magazine of ASME, March 1999. pp. 64-67.

22. Grunwald, J., and Schnack, E., "Models for Shape Optimization of Dynamically Loaded Machine Parts," WCSM01, Proceedings, Germany, Oxford: Pergamon 1995. pp. 307-310.

23. Timoshenko, S., "Analysis of Bi-Metal Thermostats," Journal of the Optical Society of America, Vol 11, 1925. pp. 233-255.

24. Chen, W.T., and Nelson, C.W. "Thermal Stresses in Bolted Joints," IBM Journal of Research and Development, Vol. 23, 1979. pp. 178-188.

25. Jiang Z.O., et. al. "Thermal Stresses in Layered Electronic Assemblies," Journal of Electronic Packaging, Vol. 119, 1997. pp. 127-132.

26. Suhir, E., "Stresses in Bi-Metal Thermostat," Journal of Applied Mechanics, Vol. 53, 1986. pp. 657-660.

27. Suhir, E., "An Approximate Analysis of Stresses in Multi-layered Elastic Thin Films," Journal of Applied Mechanics, 1988, Vol. 53, pp. 657-660.

28. Suhir, E., "Interfacial Stresses in BiMaterial Thermosts," Journal of Applied Mechanics, Vol. 56, 1989. pp. 596-600.

29. Pao, Y.H., and Eisele, E., "Interfacial Shear and Peeling Stresses in Multi-layered Thin Stacks - Subjected to Uniform Thermal Loadings," Journal of Electronic Packaging, Vol. 113, 1991. pp. 164-172.

30. Devletian, J. H., Private Communication, Oregon Graduate Institute, March 1999.

31. Hibbeler, R. C., Structural Analysis. 3rd ed. New Jersey, Prentice Hall, 1995. pp. 417.

32. Heinrich, S.M., et al., "Effects of Chip and Pad Geometry on Solder Joint Formation in SMT," Journal of Electronic Packaging, Vol. 115, 1993. pp. 433-439.

33. Lee, T.S., "Finite Element Modeling of 3-Dimensional Solder Joints Geometry in SMT," Journal of Electronic Packaging, Vol. 119, 1997. pp. 118-125.

34. Goldmann, L.S., "Geometric Optimization of Controlled Collapse Interconnections," Journal of IBM Research Development, Vol. 13, pp. 251-265.

35. Heinrich, S.M., et. al., "Solder Joint Formation in Surface Mount Technology – Part 1: Analysis," Journal of Electronic Packaging, Vol. 113, No. 3, 1990a, pp. 210-218.

36. Heinrich, S.M., et. al., "Solder Joint Formation in Surface Mount Technology – Part 2: Design," Journal of Electronic Packaging, Vol. 113, No. 3, 1990b. pp. 219-223.

37. Chiang, K.N.,and Chen, W.L., "Electronic Packaging Reflow Shape Prediction for the Solder Mask Defined Ball Grid Array," Journal of Electronic Packaging, Vol. 120, 1998. pp. 175-178.

38. Murray, T. M., et al. Floor Vibration Due to Human Activity. Chicago, AISC, 1997. pp.1-50. (Steel Design Series 11)

39. Wong H., and Lee T. T., "Thermal Evaluation of a Power PC 620 Multi-Processor Computer" Proc. 12th IEEE-THEM Symposium, 1996. pp. 72-80.

40. Vierck, R.K., Vibration Analysis. New York: Harper & Row Publisher, Inc., 1979. pp. 1-2.

41. Harper, C.A., ed., Electronic Packaging, Microelectronics and Interconnection Handbook. New York: McGraw –Hill Company, 1997. pp. 2.61, 5.62-5.66.

42. Suhir, E., "Dynamic Response of Microelectronics and Photonics Systems to Shock and Vibrations," Advances in Electronic Packaging, Hawaii, 1997. New York: ASME, 1997. pp.1685. (EEP-Vol. 19-2)

43. Suhir, E., "What can we gain using nonlinear shock photonics," Advances in Electronic Packaging, Hawaii, 1995. New York: ASME, 1995. pp.365-376. (EEP-Vol. 10-1)

44. Spyrakos, C.C., and Raftoyiannis, J., Linear and Nonlinear Finite Element Analysis. Pittsburgh, PA, Argor Publishing Division, 1997. pp. 406,180-197, 316-329.

45. Timoshenko, S. and Woinowsky-Krieger, S., Theory of Plates and Shells. New York: McGraw-Hill, Inc., 2nd ed., pp. 33-51, 79-98.

46. Gibson, R.F., Principles of Composite Material Mechanics. New York: McGraw-Hill, Inc., 1994. p. 251-258, 270-330.

47. Jones, R. M., "Mechanics of Composite Materials" 2nd ed., Philadelphia; Taylor & Francis, Inc., 1999, pp. 277-288.

48. Holung, J. A., and Wong, T., "A Probabilistic Approach to Analyzing the Shock Loadings on Portable Electronic Packages and Devices," Mechanics and Materials for Electronic Packaging, Chicago, New York, ASME, 1994. pp.145-149. (AMD Vol.187)

49. Darbha, K., et al., "Stress Analysis of Surface-Mount Interconnection Due to Vibrational Loading," Journal of Electronic Packaging, Vol. 110, 1997. pp. 187-188.

50. Chopra, A. K., Dynamics of Structures-Theory and Application to Earthquake Engineering. New Jersey: Prentice Hall, 1995. pp. 61-88.

51. Arndt, R. E. A., et al Advancement of Aerodynamics, Fluid Mechanics, and Hydraulics. New York: ASCE, 1986. pp. 949.

52. Krenk, S. and Nielsen, S. R., "Energy Balanced Double Oscillator Model for Vortex-Induced Vibrations," Journal of Engineering Mechanics, Vol. 125 no. 3, 1999, pp. 263-271.

53. Gerhart, P. M., et al., Fundamentals of Fluid Mechanics. 2nd ed., Addison-Wesley Publishing Company, 1993. pp. 639.

54. Mario, P., Structural Dynamics – Theory and Computation. 3rd ed., New York: Van Nostrand Reinhold, 1991. pp. 63-83.

55. Steinberg, D. S., Vibration Analysis for Electronic Equipment. 2nd ed., New York: John Wiley & Sons, Inc., 1988. pp. 275-326.

56. Clough, R. W., and Penzien, J., Dynamics of Structures. 2nd ed., New York: McGraw-Hill, Inc., 1993. pp. 73-82.

57. Weaver, W., Jr., et al., Vibration Problems in Engineering. 5th ed., New York: Wiley & Sons, Inc., 1990, pp. 84-98.

58. Johnson, R.A., Miller & Freund's Probability & Statistics for Engineer. 5th ed., New Jersey: Prentice-Hall, Inc., 1994. pp. 137-182.

59. Montgomery, D. C. and Ruger, G. C., Applied Statistics and Probability for Engineers. 2nd ed., New York: John Wiley and Sons, Inc., 1999. pp. 49-197.

60. Hogg, R. V. and Tanis, E. A., Probability and Statistical Inference. 5th ed., New Jersey: Prentice-Hall, Inc., 1997. pp. 62-277.

61. Alberink, I. B. and Pestman, W. R., Mathematical Statistics. New York: Walter de Gruyter, 1991. pp. 1-56.

62. Cengel, Y. A., Heat Transfer, A Practical Approach. New York: McGraw-Hill Company, 1998. pp. 862-899.

63. Moerlose, J., Temmerman, W., "Thermal Analysis of Chip on Board," Proc. 13th IEEE SEMI-THERMS: Symposium, 1997. pp. 112.

64. Simons, R.E., "Microelectronics Cooling and SEMI-THERM: A Look Back," Proc. 10th IEEE SEMI-THERM Symposium, 1994. pp. 1.

65. Guenin, B.M., et al, "Analysis of a Thermally Enhanced Ball Grid Array Package," Proc. 11th IEEE SEMI-THERM Symposium, 1995. pp. 146.

66. Yu, D., et al, "Conjugate Heat Transfer with Buoyancy Effects from Micro-Chip Sized Repeated Heaters," Journal of Electronic Packaging Vol. 119, 1998. pp. 275-280.

67. Stout, R. P., and Billings, D. T., "How to Extend a Thermal–RC-Network (Derived from Experimental Data) to Respond to an Arbitrarily Fast Input," Proc. 14th IEEE-SEMI Therm Symposium, 1998. pp. 8-15.

68. Neelakautan, S., and Addison, S., "The Effect of a Table on the Thermal Performance of an Electronic System," Proc. 14th IEEE-SEMI Therm Symposium, 1998. pp. 16-22.

69. Kabir, H. and Ortaga, A., "A New Model for Substrate Heat Spreading to Two Convective Heat Sinks; Application to the BGA Package," Proc. 14th IEEE-SEMI Therm Symposium, 1998. pp. 24-30.

70. Chung, K. "Ball-Grid Package Thermal Management," Proc. 14th IEEE-SEMI Therm Symposium, 1998. pp. 78-86.

71. Mok, L. S., "Thermal Management of Silicon-based Multichip Modulus," Proc. 10th IEEE-SEMI Therm Symposium, 1998. pp. 59-60.

72. Shaukatullah, H. and Gaynes, M.A., "Experimental Determination of the Effect of Printed Circuit Board Card Conductivity on the Thermal Performance of Surface Mount Electronic Package," Proc. 10th IEEE-SEMI Therm Symposium, 1994. pp. 44-52.

73. Lall, P., et al., Influence of Temperature on Microelectronics and System Reliability. New York: CRC Press, 1997. pp. 101-146.

74. Free, J. A., and Louie, R. R., "Recent Advances in Thermal Flow Simulation: Integrating Thermal Analysis into Mechanical Design Process," Proc. 11th IEEE-SEMI Therm Symposium, 1995. pp. 136-144.

75. Ellison, G. N., Thermal Computations for Electronic Equipment. New York: Van Nostrand Reinhold Company, Inc., 1984. pp.96-112.

76. Kirschman, R. ed. High-Temperature Electronics. New York: IEEE Press 1999 pp.5-6.

77. Bar-Cohen, A., and Knueger, W, B., "Thermal Characterization of Chip Packages-Evolutionary Development of Compact Models," Proc. 13th IEEE-SEMI Therm Symposium, 1997. pp. 180-196.

78. Incropera, F. P., and Dewitt, D. P, Fundamentals of Heat and Mass Transfer. New York: John Wiley & Sons, Inc., 1996. pp.110-112.

79. Guenin, B. M., "Transient Thermal Model for the MQUAD Microelectronic Package," Proc. 10th IEEE-THERM Symposium, 1994. pp. 86 –89.

80. Liv, D., et al., "Asymptotic Thermal Analysis of Electronic Packages and Printed-Circuit Board," Proc. 11th IEEE-THERM Symposium, 1995. pp. 131-134.

81. Zhou, T., et al., " Thermal Evaluation of Standard and power TQFP," Proc. 12th IEEE-THERM Symposium, 1996. pp. 19-24.

82. Parry, J. D. and Roston, H., "A Methodology for Thermal Characterization of IC Packages, Part I: Experimental Validation of Detailed Models," Journal of Electronic Packaging, Vol. I, 1997. pp. 989-992.

83. Guenin, B. M., et al., "Analysis of Thermally Enhanced SOIC Packages," Proc. 12th IEEE-THERM Symposium, 1996. pp. 1-70.

84. Kashiwamura, T., et al. "Structural Optimization of Electronic Components By Using Statistical Optimization Methods," Journal of Electronic Packaging, Vol. EEP-19-1, 1997. pp. 1071-1077.

85. Subbarayan, G., and Mahajan, R. L., "Strategies For Optimization of Electronic Package Design and Manufacturing Processes," Journal of Electronic Packaging, Vol. EEP-19-1, 1997. pp. 25-128.

86. Taha, H. A., Operations Research – An Introduction. Upper Saddle River, NJ, Prentice-Hall, Inc., 1997. pp. 745.

87. Pierre, D. A., Optimization Theory with Application. New York: Dover Publications, Inc., 1986. pp. 29.

88. Arora, J. S., Introduction to Optimum Design. New York: McGraw-Hill, Inc., 1989. pp. 83.

89. Nemhauser, G. L., et al., Handbook in Operations Research and Management Science. Amsterdam: Elseveir Science B.V., 1989. pp. 171-180.

90. Pant, R., "Application of Stochastic Techniques for Aircraft Conceptual Design Optimization," Oxford Pergamon, 1995. pp. 827-832.

91. Sen, M., and Stoffa, P. L., Global Optimization Methods in Geophysical Inversion. New York: Elsevier Science, 1995. pp. 83-102, 125-137.

92. Huang, M., Algorithms for Mixed Continuous-Discrete Variable Problems in Structural Optimization. Ph.D. Dissertation, University of Iowa, 1995.

93. Metropolis, N., et al. "Equation of State Calculation by fast Computing Machines," Journal of Chemical Physics. 1953. pp 21, 1087-1092.

94. Kirkpatrick, S., et al. "Optimization By Simulated Annealing," Science, Vol. 220, 1983. pp. 671-680.

95. Mathcad Version 8 Mathematical Computer Program, 1998. Cambridge, MA, Mathsoft Inc.

96. Haykin, S., Neural Networks – A Comprehensive Foundation. 2nd ed, Upper Saddle River, NJ, Prentice-Hall, 1997. pp. 2-10.

97. Dayhoff, J., Neural Network Architectures – An Introduction. New York: Van Nostrand Reinhold, 1990. pp. 217-243.

98. Statistica Neural Networks User Manual. Tulsa OK, Statsoft Inc., 1999.

99. Meekisho, L., and Nelson-Owusu, K., "Stress Analysis of Solder Joint with Torsional Eccentricity Subjected to Based Excitation," Conference Paper Present at the 12th International Conference on Mathematical and Computer Modeling and Scientific Computing, Chicago, USA, August 1999.

100. Zienkiewicz, O. C., and Taylor, R. L., The Finite Element Method. 4th ed., New York: McGraw-Hill, Inc., 1991. Vol. 2, pp. 312-429.

101. Zienkiewicz, O. C., and Taylor, R. L., The Finite Element Method. 4th ed., New York: McGraw-Hill, Inc., 1991. Vol. 1, pp. 3-59, 89-135.

102. Spyrakos, C. C., Finite Element Modeling in Engineering Practice. Pittsburgh, PA, Argor Publishing Division, 1996. pp. 75-166.

103. Bolton, A., Structural Dynamics in Practice: A Guide for Professional Engineers. UK: McGraw-Hill International, 1994. pp. 31-53; 107-137.

104. Tumn, J.J. and Cheng F. Y., Dynamic Structural Analysis. New York: McGraw-Hill, Inc., 1983. pp. 10-205.

105. Stardyne Finite Element Analysis Computer Program User Manual. Yorba Linda, CA, Research Engineers, 1985.

VITA

Kofi Nelson-Owusu was born on December 17, 1964 in Kumasi, Ghana. He started his engineering education at University of Science and Technology in Ghana, 1987. He transferred to Portland State University in Portland, Oregon in 1990 where he received both his BS and MS in civil engineering in 1992 and 1994 respectively. Working as a structural engineering for both private and public establishments, he enrolled in Oregon Graduate Institute of Science and Technology in Portland, Oregon in 1997. He finished the requirements for the degree of Doctor of Philosophy in Material Science and Engineering in January 2000.

Professional Affiliation(s):

Associate member of Structural Engineers Association of Oregon, SEAO.

Associate member of American Society of Civil Engineers, ASCE.

Publications

1. Meekisho, L., and Nelson-Owusu, K., "Stress Analysis of Solder Joint with Torsional Eccentricity Subjected to Based Excitation," Conference Paper Present at the 12th International Conference on Mathematical and Computer Modeling and Scientific Computing, Chicago, USA, August 1999.

2. Nelson-Owusu, K., "The Significant of the Missing-Link (Panel Zone Deformation) on the Total Steel Rigid Frame Lateral Displacement as Addressed by UBC-97, Section 1630.2, Item-2 Provision," Connections: A publication of Structural Engineers of Oregon, April 1998. pp. 6-9.

3. Nelson-Owusu, K., "Designing for Seismic-Induced In-lnplane Shear Forces in Unreinforced Masonry Wall Overlaid With Reinforced Concrete to Achieve Optimum Structural Response," Connections: A publication of Structural Engineers of Oregon, September 1996. pp. 7-10.